Large-Eddy Simulation of Molecular Mixing in a Recirculating Shear Flow

Thesis by

Georgios Matheou

In Partial Fulfillment of the Requirements

for the Degree of

Doctor of Philosophy

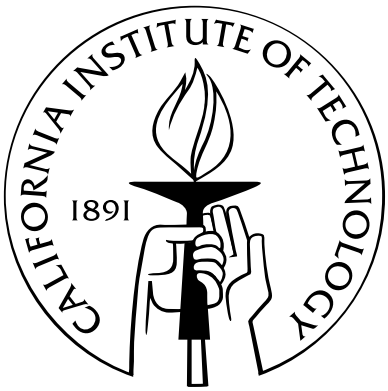

California Institute of Technology

Pasadena, California

2008

(Defended May 9, 2008)

To Andri

Acknowledgements

I would like to express my deepest appreciation towards my advisor, Professor Paul Dimotakis, for his mentorship, guidance, and support during my time at Caltech. This work would not have been made possible without his efforts to provide essential resources. My gratitude also extends to the other members of my committee, Professors Tim Colonius, Daniel Meiron, Dale Pullin, and Joseph Shepherd, for their suggestions and constructive criticism of the thesis.

I am also indebted to Professor Carlos Pantano, who has been a great (and patient) mentor. I would like to thank Carlos Pantano, David Hill, and Ralf Deiterding for their assistance with the VTF/AMROC computational framework, and for developing and maintaining this tool.

Aristides Bonanos, Jeff Bergthorson, and Michael Johnson provided the experimental measurements used in the simulations presented in this thesis. I would like to thank them for their assistance with the experimental data and the numerous discussions that improved the quality of this work.

I would also like to acknowledge discussions with the members of the GALCIT community and the Compressible Turbulence group that was part of the Caltech Advanced Simulation and Computing (ASC) program. I would especially like to thank Kazuo Sone, Antonino Ferrante, and Daniel Appelö for discussions on numerical analysis and computer science issues. Computer support by Dan Lang and administrative support by Christina Mojahedi at Professor Dimotakis' group are also appreciated. I would like to thank the Center for Advanced Computing Research at Caltech and the Livermore Computing Center at Lawrence Livermore National Laboratory for technical assistance.

This work was supported by AFOSR Grants FA9550-04-1-0020, FA9550-04-1-0389, and FA9550-07-1-0091, by the Caltech DOE Advanced Simulation and Computing (ASC) Alliance Center under subcontract No. B341492 of DOE contract W-7405-ENG-48, and NSF Grant EIA-0079871.

During my time at Caltech I have met many friends who have made this experience more enjoyable and rewarding. In particular, I would like to thank (in the order I met them) Fotini Liepouri, George Lykotrafitis, Melania Apostolidou, Aristides Bonanos, and Benjamin Sexson.

I would also like to thank my family for their support. This thesis is dedicated to Andri, for her unconditional love, encouragement and support throughout this journey.

Abstract

The flow field and mixing in an expansion-ramp geometry is studied using large-eddy simulation (LES) with subgrid scale (SGS) modeling based on the stretched-vortex model for momentum and scalar subgrid turbulent transport. The expansion-ramp geometry was developed to provide enhanced mixing and flameholding characteristics while maintaining low total-pressure losses, elements that are important in the design and performance of combustors for hypersonic air-breathing propulsion applications. In the expansion ramp configuration considered in this study, a subsonic top stream is expanded over a perforated ramp at an angle of 30° through which a secondary stream is injected. The separation of the top stream creates a shear layer that reattaches on the lower wall when the mass flux of the lower stream is insufficient to provide the entrainment requirements, in a similar manner to a backward-facing step configuration. Depending on the mass-flux ratio of the two streams the shear layer splits at reattachment, and part of the flow is deflected upstream forming a re-entrant jet within the recirculation zone, resulting in enhanced mixing and flameholding.

The approach followed in this work relies on verification and validation of the numerical methods and turbulence models, focusing on development of a truly predictive computational framework for turbulent-mixing applications. The mixing was studied by tracking a passive scalar without taking into account the effects of chemical reactions and heat release, an approximation expected to be adequate in experiments conducted in parallel. The numerical methodology employs non-dissipative approximations of the spatial derivatives and a turbulence model based on physical arguments. No turbulence-model parameters were adjusted in the simulations.

The computer code is first verified using an exact solution of the Euler equations. A vortical solution on a periodic domain is used to verify the order of accuracy of the interior stencil. In order to assess the solver and the boundary closure implementation, a method utilizing results from linear stability analysis (LSA) theory is developed. LSA can be used to compute unstable perturbations to a flow, subject to certain approximations. The perturbations computed from LSA are then used as an inflow condition to the flow computed by the solver been assessed. A projection-based metric is constructed that only assumes the shape of the solution and not the growth rate of the perturbations, thus also allowing the latter to be determined as part of the verification. The growth rate of the perturbations for an unbounded (effectively) incompressible shear layer and a confined compressible

shear layer is found to be in agreement with the prediction of the LSA.

The flow and mixing predictions of the LES are in good agreement with experimental measurements in the expansion-ramp geometry. Specifically, the recirculating flow between the ramp and the reattachment of the shear layer is reproduced by the LES. The magnitude of the velocity of upstream-moving flow near the lower wall is 10–15% of the top free stream for mass-injection ratios of about 1/10, but becomes negligible as the flow tends towards a free shear layer, for higher mass-injection ratios of about 1/5. The mean reattachment length of the primary shear layer is somewhat overpredicted by the simulations for all the cases studied. The agreement in the pressure coefficient profiles along the top and bottom walls and the total pressure profiles along the transverse direction is satisfactory.

Total (resolved and subgrid) probability density functions (PDFs) of the scalar are estimated using an assumed beta-distribution model for the subgrid scalar field. The improved mixing characteristics of the geometry compared to free shear layers at equivalent conditions are illustrated by the shapes of the PDFs. Moreover, the temperature rise and the probability of mixed fluid profiles are in good agreement with the experimental measurements, indicating that the mixing on a molecular scale is correctly predicted by the LES–SGS model.

Finally, the predictions of the LES are shown to be resolution-independent by computing the flow for three resolutions, differing by a factor of 2 in each direction between them. The mean fields and passive scalar PDFs have essentially converged at the two finer grid resolutions used.

Contents

List of Figures

List of Tables

Chapter 1

Introduction

Mixing on a molecular scale of two or more fluids of different composition is achieved by the action of diffusion. The rate of mixing of different species is of great importance because the speed of chemical reactions in many applications, such as fuel combustion, is limited by the availability of molecularly mixed reactants.

Diffusion is a relatively slow process because it relies on molecular collisions. Fortunately, (macroscopic) large-scale motions can significantly enhance the rate of mixing. Reynolds (1883) first introduced a dimensionless parameter, now called the Reynolds number, after observations of laminar-turbulent flow transition in a pipe. The Reynolds number, defined as

$$Re = \frac{U\ \delta}{\nu}, \tag{1.1}$$

relates the characteristics of the aforementioned "large-scale motions" through the velocity of the fluid, U, and an appropriate length scale of the motion, δ, to the diffusion coefficient of momentum, ν, also called the kinematic viscosity. Stability analysis of flows (e.g, Drazin & Reid, 2004) later corroborated the observation of Reynolds (1883) that when the Reynolds number is sufficiently large "...the flow rapidly becomes complicated and confused" as stated in (Landau & Lifshitz, 1959, p. 108), who continue to add that "Such flow is said to be turbulent," thereby giving a rudimentary definition of turbulence.

Turbulent transport is not only important for species mixing. An example is the increased drag observed for a flat-plate boundary layer when the boundary layer is turbulent compared to a laminar one (e.g., Schlichting, 1979). The turbulent flow enhances momentum transport normal to the wall resulting in increased drag. In the case of species mixing, stirring produced by the irregular motion of the fluid creates a large interfacial surface which increases the rate of mixing (Batchelor, 1959; Landau & Lifshitz, 1959; Tennekes & Lumley, 1972; Dimotakis, 1986, 2000).

1.1 Motivation—Enhanced mixing for air-breathing propulsion applications

Motivation for this work is the investigation of fundamental fluid dynamics important to the performance of combustors for hypersonic air-breathing propulsion applications, such as supersonic-combustor ramjets (scramjets) (Curran & Murthy, 2000; Curran, 2001). The foremost challenge in the design and operation of scramjet engines is addition of energy to a supersonic stream by mixing and combusting a fuel. Although this can be accomplished by a variety of passive and active mechanisms, practical considerations require high combustion efficiency with reduced-length combustors (Curran et al., 1996; Seiner et al., 2001).

The two canonical flows most widely used in the study of turbulent mixing are jets and shear or mixing layers. Typical configurations for enhanced mixing in supersonic flow combustors rely on combinations of jets and shear layers (Gutmark et al., 1995; Kutschenreuter, 2000). Enhanced mixing alone is not sufficient. Regions of strain rate lower than the extinction strain rate of hydrocarbon fuels are required for sustaining combustion (Egolfopoulos et al., 1996) together with low total pressure losses to achieve the necessary propulsion efficiency.

In a shear or mixing layer, two near-parallel streams of unequal velocities, initially separated by a thin spitter plate, are allowed to mix. Many studies have investigated the characteristics of this flow in the context of turbulent mixing. Brown & Roshko (1974) noted the presence of large spanwise organized structures in incompressible, high-Reynolds-number shear layers. Konrad (1976) observed that after the transition of the flow from laminar to unsteady, due to the formation of the large coherent structures, another type of transition occurred further downstream of the splitter plate, that is, at a higher Reynolds number. This type of transition was associated with the ability of the flow to sustain three dimensional fluctuations with the appearance of smaller scales and streamwise vortices on the surface of the large structures. In similar observations in a chemically reacting shear layer Breidenthal (1978) showed that the onset of three dimensionality was correlated with a rapid transition (increase) in the amount of product, which he refers to as the "mixing transition." The mixing transition in turbulent flows was later documented for other flows and introduced in a formal framework by Dimotakis (2000). Dimotakis (2000) notes that the mixing transition is a universal property of turbulence occurring when there is sufficient separation of scales to sustain fully developed turbulence.

Entrainment and growth rate processes in incompressible shear layers are well understood (Dimotakis, 1986, 1991), despite the fact that prediction of the growth rate appears to be sensitive to the inflow conditions (e.g., Slessor et al., 1998), with important implications for the simulation of such flows. For incompressible shear layers about half the fluid within the layer is mixed on a molecular scale (Dimotakis, 1991). Turbulent mixing can be viewed more generally as a three-stage

process (Eckart, 1948). Using the shear layer as an example: the fluid is initially entrained in the mixing layer through the action of the large scale structures, is then stirred by turbulence and at the smallest space-time scales is homogenized by diffusion.

Mixing in compressible shear layers has not been as well characterized. The growth rate of the mixing zone, which sets an upper bound on the mixing, decreases with increasing compressibility (Papamoschou & Roshko, 1988; Slessor et al., 2000), however, contradictory trends are reported for the fraction of the mixed fluid in the mixing layer with respect to compressibility (Hall et al., 1991; Island et al., 1996; Freund et al., 2000; Rossmann et al., 2004). The reduction in growth rate and the amount of mixed fluid are both important issues in the context of air-breathing high-speed propulsion.

Jets in crossflow are another canonical flow that has been studied extensively (Zukoski & Spaid, 1964; Spaid & Zukoski, 1968; Hollo et al., 1994; Smith & Mungal, 1998; Ben-Yakar et al., 2006; Shan & Dimotakis, 2006). The jet in crossflow has higher entrainment rate than a jet into a quiescent reservoir, however, in supersonic flow, a bow shock forms upstream of the injector resulting in high total-pressure loses. The bow shock causes the boundary layer to separate, creating a flameholding region where fuel and air can mix subsonically (Zukoski & Spaid, 1964; Spaid & Zukoski, 1968; VanLerberghe et al., 2000). As a way of improving the flameholding characteristics of the device, a cavity can be added downstream of the injection (Yu et al., 1998; Ben-Yakar & Hanson, 2001; Yu et al., 2001) but with a significant drag penalty generated by the forward-facing facet.

1.2 The expansion-ramp injection geometry

Jets and shear layers alone cannot satisfy the performance requirements of supersonic combustors. Shear layers have negligible total pressure losses but the mixing is limited by the shear layer growth. Transverse and inclined jets, on the other hand, produce bow shocks that reduce the efficiency of the device.

In this work, the flow and mixing in an expansion-ramp geometry is studied through numerical simulations. The expansion-ramp geometry (Fig. 1.1) combines the low strain-rate flameholding characteristics of backward facing steps with low-pressure losses of free shear layers (Johnson, 2005; Bonanos et al., 2007, 2008a; Bergthorson et al., 2008; Bonanos et al., 2008b). In the expansion-ramp configuration the top, high-speed ("air") stream is expanded over a ramp at 30° to the flow. The lower ("fuel") stream is injected through perforations in the expansion ramp. Similar to the case of flows over backward-facing steps (Eaton & Johnston, 1981), for subsonic and transonic top streams, the flow separates at the end of the splitter plate, where the expansion begins, and forms a shear layer. This is identified as the primary shear layer in the expansion-ramp configuration. When the lower stream flow cannot satisfy the entrainment requirements of the primary shear layer, the shear

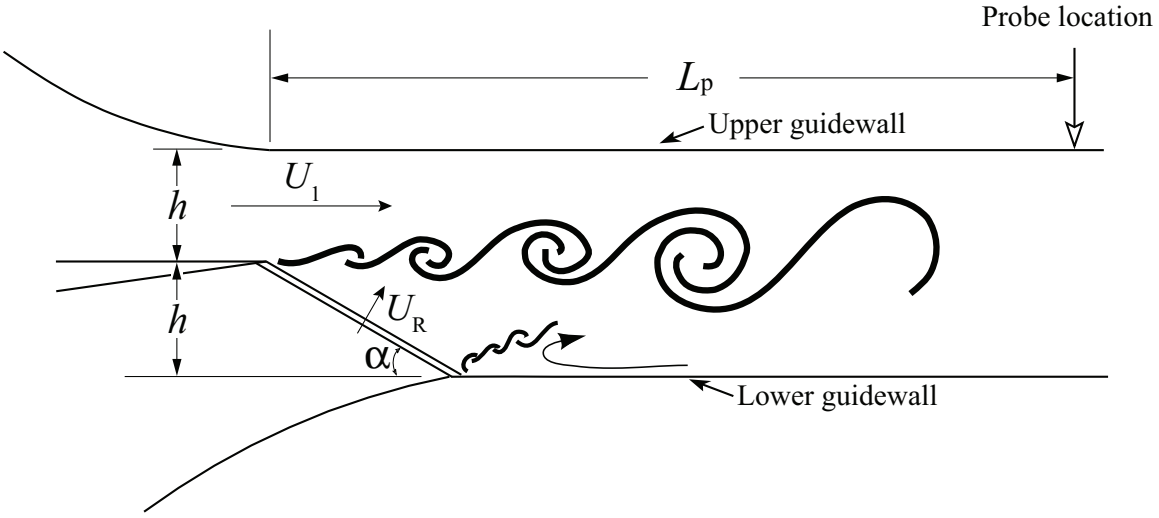

Figure 1.1: Schematic of the expansion-ramp geometry. The top stream, U_1, enters the test section in the horizontal direction while the lower stream, U_R, is injected through a perforated ramp at $\alpha = 30°$. The separating top stream forms the primary shear layer, which reattaches downstream (not pictured) with part of the flow being deflected upstream in the recirculation region. The upstream moving fluid forms a secondary shear layer where the ramp meets the lower guide wall.

layer curves toward the lower guide wall and reattaches.

Within the reattachment region on the lower wall, the shear layer splits with part of the flow deflected upstream into the recirculating flow region formed between the ramp and the reattachment (see Fig. 1.1). The deflection of the shear layer upstream is similar to the re-entrant jet formed at the end of a cavitation region (e.g., Callenaere et al., 2001). The re-entrant jet carries hot products and radicals upstream that mix with lower-stream fluid forming a secondary shear where the ramp meets the lower guide wall. This is a second mixing layer that allows products to further mix with the lower stream. The recirculating region, re-entrant jet, and the secondary shear layer allow for enhanced mixing compared to a free shear layer while providing a low strain-rate environment (Johnson, 2005; Bergthorson et al., 2008; Bonanos et al., 2008b).

The length of the recirculation zone can be controlled through variation of the mass-injection ratio of the two streams. Increasing the injection pushes reattachment downstream leading to a change in the pressure coefficient at a given streamwise location. Heat release via exothermic reaction in the shear layer has the same effect as increasing the mass flux of the lower stream because of the reduced volumetric entrainment of free-stream fluid (Hermanson & Dimotakis, 1989; Johnson, 2005; Bergthorson et al., 2008; Bonanos et al., 2008b).

1.2.1 Description of the experiments

The simulations performed correspond to the experiments documented by Johnson (2005) and Bergthorson et al. (2008). The results of the simulations are compared to the experimental measure-

ments. A brief description of the experiments is presented here in order to facilitate the discussion of the comparison between experiments and simulations. Further details can be found in Johnson (2005), Bonanos et al. (2007), Bergthorson et al. (2008), Bonanos et al. (2008a), and Bonanos et al. (2008b).

The experiments were performed in the Supersonic Shear Layer (S^3L) laboratory at Caltech (Hall et al., 1991). The top stream is delivered from a large pressure vessel using a control program to maintain constant pressure in the upstream plenum and can reach flow speeds up to $M_1 \approx 3.2$. The lower stream has a constant mass flux, metered using a calibrated sonic valve. The two streams are accelerated through converging nozzles designed to minimize the boundary-layer thickness on the splitter plate and turbulence generation at the design Mach number. The lower stream is injected through a perforated expansion ramp angled at $\alpha = 30^\circ$ with respect to the horizontal. The ramp is perforated with 3611 1.55-mm-diameter holes, corresponding to an open-area fraction of 0.60. The test section height is $2h = 10.16$ cm, with the individual stream height being h (Fig. 1.1). The nominal run time in the facility is 2–6 seconds.

The $H_2/NO/F_2$ system is used to study the mixing in the expansion ramp geometry. Specifically, the top stream is seeded with a mixture of hydrogen (H_2) and nitric oxide (NO), and the bottom stream with fluorine (F_2). The remainder of the gas in both streams is comprised of helium, argon, and nitrogen inert diluents, with compositions chosen to match the molar mass and specific-heat ratio of the two streams. Nitric oxide is added to the hydrogen stream to generate radicals on contact with fluorine to initiate the hydrogen-fluorine reaction (Mungal & Dimotakis, 1984). The reaction then proceeds without an ignition source (hypergolically) at room temperature.

Flow-field measurements are obtained by pressure taps along the lower and upper guide walls, and a measurement rake that can be placed at distances $L_\mathrm{p} = 7h - 9h$ downstream of the splitter plate. Temperature and total and static pressures are measured at the rake through an array of thermocouple and pressure probes. In addition to temperature and pressure data, Schlieren flow visualization is utilized as a concurrent non-intrusive diagnostic. Figures 1.2 and 1.3 show Schlieren images of the flow for two mass-injection ratios (Johnson, 2005). The primary and secondary shear layers are clearly visible in Fig. 1.2. In Fig. 1.3 the increased injection pushes the recirculation zone downstream. The upstream-moving mixed fluid does not reach the ramp to form the secondary mixing layer and the flow becomes similar to a free shear layer.

The amount of molecularly mixed fluid is estimated using the "flip" experimental technique (Mungal & Dimotakis, 1984; Koochesfahani & Dimotakis, 1986). Mixing is computed from a pair of chemically reacting experiments. In one of the experiments, the top stream is rich in its reactants whereas in the other the compositions are "flipped" so that the lower stream is rich in its reactants. Recording the temperature rise that accompanies the chemical-product formation allows the amount of molecularly mixed fluid to be inferred. This way, the measurements are not affected by

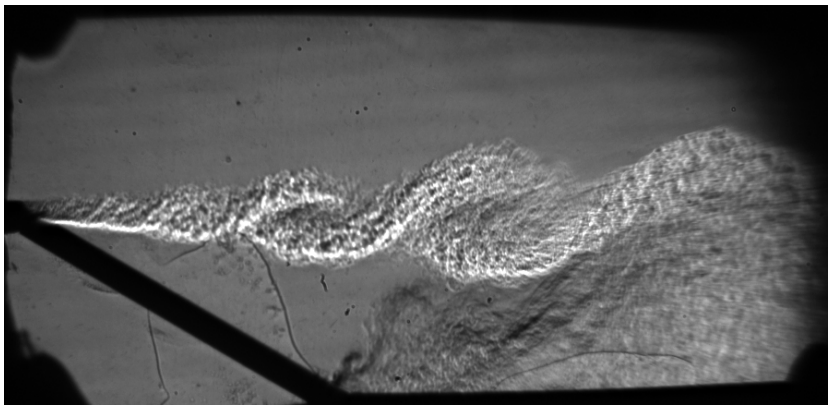

Figure 1.2: Schlieren visualization of the flow in the expansion ramp geometry from the experiments of Johnson (2005). The primary and secondary shear layers are clearly visible. Upper stream $U_1 \approx 120$ m/s, lower steam $U_\mathrm{R} \approx 5.5$ m/s. Upper stream composition is N_2 and lower stream is 66.66% Ar, 33.33% He (non-reacting flow).

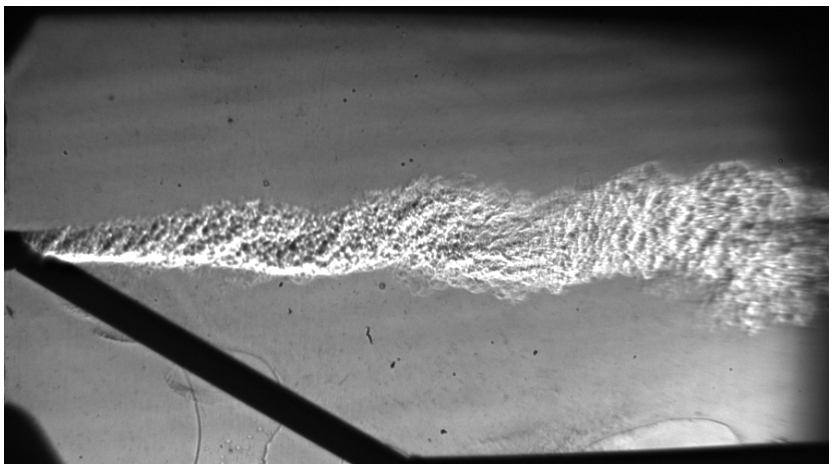

Figure 1.3: Schlieren visualization of the flow in the expansion ramp geometry from the experiments of Johnson (2005). Upper stream $U_1 \approx 120$ m/s, lower steam $U_\mathrm{R} \approx 12.5$ m/s. Upper stream composition is N_2 and lower stream is 66.66% Ar, 33.33% He (non-reacting flow). The increased injection pushes the recirculation zone downstream eliminating the secondary mixing layer (cf. Fig. 1.2).

limitations in spatial resolution since only fluid mixed on a molecular scale reacts and contributes to the temperature rise.

The "flip" experiment relies on two underlying assumptions: that the experiments are performed in the mixing-limited regime and that the flow in the pair of experiments remains unchanged with the changing location of the temperature rise. The first assumption is validated by computing the Damköhler number, $Da \equiv \tau_{\mathrm{m}}/\tau_{\chi}$, the ratio of the mixing time scale to the chemical time scale for experiments that have converged with respect to chemical reaction rates. The chemical time scale is estimated using the "balloon-reactor" model of Dimotakis & Hall (1987). The studies of Hall et al. (1991), Slessor et al. (1998), and Bond (1999) have shown that the flow is mixing-limited when $Da > 1.5$. In the experiments considered here, this condition is satisfied. The assumption that the flow must remain unchanged in the pair of experiments is assessed by examining the stagnation pressure profiles recorded along the measurement rake (Johnson, 2005; Bergthorson et al., 2008; Bonanos et al., 2008b). The flow is deemed matched if the stagnation pressure profiles are in agreement.

1.3 Modeling for turbulent mixing and nonpremixed combustion

The objective of this study is the numerical simulation of the flow in the expansion-ramp geometry corresponding to subsonic experimental conditions. The experiments documented in Johnson (2005) and Bergthorson et al. (2008) provide good information on the flow field and mixing characteristics for a range of conditions and a well-documented, suitable arena against which to validate numerical simulations.

The main goal of the current work is to address the prediction challenge in the computational simulation of complex flows. The experiments in the expansion-ramp geometry provide a framework for the assessment of such models for turbulent momentum and species mixing. Although the current work is concerned with a specific numerical model, the assessment methodology is generally applicable and the outcome provides guidance for further development.

The numerical model is now characterized in more detail. Numerical integration of the Navier–Stokes equations provides the evolution of the fluid mechanical fields. However, the broad range of spatial and temporal scales characterizing most turbulent flows of interest place direct numerical simulation (DNS) beyond practical reach. Several methods have been developed to obtain approximate solutions that capture the behavior of turbulent flows. Such methods are called turbulence models.

Large-eddy simulation (LES) is a category of turbulence models in which the large-scale turbulent motions are resolved, whereas scales below a certain cut-off are modeled. The smallest scales contain

only a small fraction of the turbulent kinetic energy, are more homogeneous and universal, and typically are less sensitive to modeling assumptions (Tennekes & Lumley, 1972; Pullin, 2000; Pope, 2004a). In the simulations presented here, LES with subgrid scale modeling (LES–SGS) is employed, where the effects of scales smaller than those resolved by the simulation are explicitly described by the turbulence model as opposed to relying on the dissipation supplied by the numerical scheme used to approximate the spatial derivatives.

LES is a widely used technique for the simulation of turbulent flows and a number of reviews have addressed this approach (e.g., Lesieur & Metais, 1996; Ghosal, 1999; Piomelli, 1999; Meneveau & Katz, 2000; Oefelein, 2006; Pitsch, 2006). The LES equations are derived from the Navier–Stokes equations by performing a filtering operation (Leonard, 1974) with a filter width usually of the size of the grid spacing. The filtering produces additional terms, a tensor in the momentum equations and fluxes for the energy and species equations. The subgrid-stress tensor and energy and species fluxes, cannot be expressed solely as functions of the filtered quantities and must be modeled.

LES has been successful in the simulation of many non-reacting flows (Lesieur & Metais, 1996) but the simulation of turbulent mixing in reacting and non-reacting flows still presents many challenges. See, for example, Peters (2000) and Poinsot & Veynante (2005). Turbulence models for momentum transport rely on theoretical advances like the eddy cascade and scale invariance in the inertial subrange (Tennekes & Lumley, 1972; Pope, 2004a). On the other hand, mixing on a molecular scale takes place only at the smallest scales of the flow (Dimotakis, 1991, 2005; Warhaft, 2000). Most of the fluid homogenization occurs subgrid, and SGS models must "infer" subgrid mixing based on the resolved scales. Turbulent mixing in reacting flows presents additional challenges since mixing produces changes in the composition of the fluid which can change the dynamics of the flow.

The subgrid terms are often modeled using the gradient-transport assumption in the context of Smagorinsky-type models (Smagorinsky, 1963). For such models, the SGS stress tensor takes the form

$$\tau_{ij} = -2\,\bar{\rho}\,C_{\mathrm{s}}\Delta^2|\widetilde{S}|\widetilde{S}, \tag{1.2}$$

and the subgrid scalar flux (Moin et al., 1991)

$$g_i = -\bar{\rho}\,\frac{C_{\mathrm{s}}\Delta^2|\widetilde{S}|}{Pr_{\mathrm{t}}}\frac{\partial\widetilde{Z}}{\partial x_i}, \tag{1.3}$$

where $\widetilde{S}$ is the resolved (filtered) strain tensor, Δ is the filter width, ρ is the density and Z the scalar concentration. Closure is attained by introducing the concept of turbulent Prandtl number, Pr_{t} in combination with the Smagorinsky coefficient, C_{s}. The SGS momentum transport can be expressed, similar to the SGS scalar flux, in terms of a turbulent viscosity coefficient, ν_{t}. These formulations are a generalization of Prandtl's mixing-length model (e.g., Tennekes & Lumley, 1972) and carry some of the same deficiencies. The Smagorinsky coefficient is found to be flow- and resolution-dependent

(Moin et al., 1991) and, for some flows, assuming constant values throughout the flow produces overly dissipative models (Ducros et al., 1996).

Germano et al. (1991) suggested a dynamic procedure for the estimation of the Smagorinsky coefficient by introducing a test filter $\hat{\Delta}$ in addition to the grid filter Δ. The width of the test filter is usually set to twice the grid filter. Moin et al. (1991) implemented the Dynamic Procedure to estimate the turbulent Prandtl number in Eq. 1.3.

Pullin et al. (Pullin & Saffman, 1994; Misra & Pullin, 1997; Voelkl et al., 2000; Pullin, 2000) proposed a vortex-based model for the SGS stresses and fluxes based on the exact Navier–Stokes solution by Lundgren (1982) for a vortex in a strain-rate field. In this model the subgrid fields are represented by a collection of vortical structures. The resulting expression for the subgrid tensor depends on the energy spectrum of the vortex, $E(k)$, and the distribution of the orientation of the vortical structures,

$$\tau_{ij} = 2 \int_{\pi/\Delta}^{\infty} E(k) \mathrm{d}k \langle E_{pi} Z_{pq} E_{qj} \rangle. \tag{1.4}$$

E_{pi} is the transformation matrix from the vortex-fixed to the laboratory frame of reference, Z_{pq} is a diagonal matrix with the elements (1/2, 1/2, 0), and $\langle E_{pi} Z_{pq} E_{qj} \rangle$ signifies the ensemble average over the orientations of the vortex structures.

In the case of subgrid scalar transport, the SGS flux is estimated by assuming that the scalar is wrapped by the SGS vortex velocity field, resulting in a tensor eddy-diffusivity model for SGS transport. The subgrid transport is not in the direction of the resolved gradient but orthogonal to the subgrid vorticity (Pullin, 2000; Pullin & Lundgren, 2001).

The basis for most nonpremixed combustion models is to track the mixing of fuel and oxidizer by a passive scalar. If the chemistry is fast enough (high Da) a reaction layer forms at approximately stoichiometric composition and the flame can be assumed to have a negligible thickness (Burke & Schumann, 1928). This is true for high activation energy reactions, such as combustion of hydrocarbon fuels, but is not the case for the $H_2/NO/F_2$ system. For infinitely fast chemistry, all species mass fractions and temperature can be expressed as function of a passive scalar Z. When parameterizing the combustion by the passive scalar Z, the effects of chemical reactions and heat release are entirely neglected. Akselvoll & Moin (1996) and Pierce & Moin (1998) conducted LES of passive scalar mixing of turbulent confined coannular jets using the gradient-transport model (Eq. 1.3) employing the Dynamic Procedure (Germano et al., 1991; Moin et al., 1991).

Laminar flamelet models are conserved-scalar models that account for finite-rate chemistry effects. Williams (1975) proposed that a turbulent flame can be considered as an ensemble of thin reactive-diffusive layers called flamelets. Flamelet models utilize passive scalars in combination with state relationships to account for the effects of chemistry (Peters, 1984, 2000). Pitsch & Steiner (2000) used a Lagrangian flamelet model (LFM) in LES of a jet diffusion flame.

Klimenko (1990) and Bilger (1993) independently introduced the concept of conditional moment closure (CMC); see also Klimenko & Bilger (1999) for a more recent review. Unlike the flamelet models, in CMC one solves the equations for reactive scalars conditioned on the mixture fraction Z. This can be advantageous from the modeling perspective and computationally more efficient (Klimenko, 1990), however, it adds more independent variables to the equations, namely the scalar(s) Z_i.

Another class of models is based on probability density function (PDF) transport equations. Pope (1990) proposed the use of the equation for the joint PDF of velocity, viscous dissipation and reactive scalars, corresponding to single realization of the subgrid state of the mixture. Gao & O'Brien (1993) and Colucci et al. (1998) also studied and extended the PDF transport method while Hulek & Lindstedt (1998) used a joint scalar-velocity formulation in simulations of mixing with chemical reactions in a scalar mixing layer in grid turbulence. Because of the high dimensionality of the PDF transport equations, numerical implementations typically rely on Monte-Carlo methods employing a large number of notional particles (Pope, 1985), resulting in high computational costs.

Linear-eddy models (LEM) were first introduced by Kerstein (1988, 1989, 1990) and model SGS mixing using a one-dimensional stochastic approach. An extension of the ideas of the LEM to the velocity field by Kerstein (1999) is called the one-dimensional turbulence (ODT) model.

More recently, Pantano & Sarkar (2001) and Mellado et al. (2003) introduced a class of reconstruction moments by combining an approximate reconstruction with additional physics-based information required to match specific scalar moments—the subgrid variance, for example.

LES of turbulent combustion is an active research field and despite the large number of proposed models there are many unresolved issues and challenges. The requirement for predictive simulations is generally acknowledged in combination with high-quality validation data sets. Some of the most recent methods were briefly described above. A more detailed discussion of methods can be found in the review by Pitsch (2006) and the books by Peters (2000) and Poinsot & Veynante (2005).

Chapter 2

Numerical Modeling

2.1 Governing equations

The governing equations, in the context of large-eddy simulation, are the two-component Favre-filtered (density weighted) compressible Navier–Stokes equations. The Favre-filtered quantities are defined as

$$\tilde{f} \equiv \frac{\overline{\rho f}}{\bar{\rho}}, \tag{2.1}$$

for an arbitrary field f, where ρ is the density. The overbar indicates the filtering operation

$$\bar{f}(\mathbf{x}, t) \equiv \int G(\mathbf{x} - \mathbf{x}') f(\mathbf{x}', t) \mathrm{d}\mathbf{x}', \tag{2.2}$$

with a convolution kernel $G(\mathbf{x})$ (Leonard, 1974).

The mixing in the expansion-ramp geometry is parameterized in terms of the mixture fraction Z. In the experiments, the rate of the chemical reactions is fast and the heat release is low. The adiabatic flame temperature rise is about 94 K for a mixture of 1% H_2 in the upper stream and 1% F_2 in the lower stream, both diluted with N_2 (Johnson, 2005), resulting in an essentially cold reaction. Therefore the passive scalar approximation is an adequate representation of reality. The mixing problem reduces to the mixing of a chemistry-independent conserved scalar Z, and most quantities of interest can be expressed as functions of Z (see also, Williams, 1985; Peters, 2000).

The conservation equations for mass, momentum, energy and a passive scalar are, respectively,

$$\frac{\partial \bar{\rho}}{\partial t} + \frac{\partial \bar{\rho} \tilde{u}_i}{\partial x_i} = 0, \tag{2.3}$$

$$\frac{\partial \bar{\rho} \tilde{u}_i}{\partial t} + \frac{\partial (\bar{\rho} \tilde{u}_j \tilde{u}_i + \bar{p} \delta_{ij})}{\partial x_j} = \frac{\partial \bar{\sigma}_{ij}}{\partial x_j} - \frac{\partial \tau_{ij}}{\partial x_j}, \tag{2.4}$$

$$\frac{\partial \overline{E}}{\partial t} + \frac{\partial (\overline{E} + \bar{p})\tilde{u}_i}{\partial x_i} = \frac{\partial}{\partial x_i}\left(\tilde{\kappa}\frac{\partial \tilde{T}}{\partial x_i}\right) + \frac{\partial (\bar{\sigma}_{ij}\tilde{u}_j)}{\partial x_i} - \frac{\partial q_i}{\partial x_i}, \tag{2.5}$$

$$\frac{\partial \bar{\rho}\tilde{Z}}{\partial t} + \frac{\partial \bar{\rho}\tilde{Z}\tilde{u}_i}{\partial x_i} = \frac{\partial}{\partial x_i}\left(\bar{\rho}\tilde{D}\frac{\partial \tilde{Z}}{\partial x_i}\right) - \frac{\partial g_i}{\partial x_i}. \tag{2.6}$$

The subgrid terms, τ_{ij}, q_i, and g_i, represent the subgrid stress tensor, and the heat and scalar transport flux, respectively. The filtered total energy per unit volume, $\overline{E}$, is the sum of the internal and kinetic energy (resolved and subgrid),

$$\overline{E} = \frac{\bar{p}}{\gamma - 1} + \frac{1}{2}\bar{\rho}(\tilde{u}_i\tilde{u}_i) + \frac{1}{2}\tau_{ii}, \tag{2.7}$$

where the filtered pressure, $\bar{p}$, is determined from the ideal-gas equation of state,

$$\bar{p} = \bar{\rho}R\tilde{T}. \tag{2.8}$$

Since the fully resolved fields are not available in LES, the filtering operation (Eq. 2.1) is purely formal, and only used to construct the LES equations. The subgrid terms cannot be evaluated using information derived from the resolved scales (closure problem) and a model, or additional information, are required to approximate them. Integration of the LES equations will yield the time evolution of the resolved fields. Any instantaneous realization of the resolved field carries limited information however, not only because of the characteristics of the modeling, but also because of the random nature of the turbulent flow. Therefore, one is primarily interested in the statistics of the resolved field and, through the use of models for the unresolved field structure, in pointwise quantities, such as the amount of mixed fluid on a molecular scale. A discussion on the conceptual foundations of LES can be found in Pope (2004b).

2.2 Subgrid closure

The subgrid turbulent transport terms are computed using the stretched-vortex subgrid scale (SGS) model of Pullin et al., originally introduced for incompressible LES by Misra & Pullin (1997) and Voelkl et al. (2000), and subsequently extended to compressible flows by Kosovic et al. (2002) and subgrid scalar transport by Pullin (2000) and Pullin & Lundgren (2001). In the version of the stretched-vortex SGS model used in this work, the subgrid tensor and fluxes in each computational cell are assumed to result from the flow produced by a Lundgren spiral vortex (Lundgren, 1982) aligned with the local resolved-scale strain.

The expressions for the subgrid tensor and fluxes are

$$\tau_{ij} = \bar{\rho}\tilde{k}\left(\delta_{ij} - e_i^v e_j^v\right), \tag{2.9}$$

$$q_i = -\bar{\rho}\frac{\Delta_c}{2}\tilde{k}^{1/2}\left(\delta_{ij} - e_i^v e_j^v\right)\frac{\partial(\tilde{c}_p\tilde{T})}{\partial x_j}, \tag{2.10}$$

$$g_i = -\bar{\rho}\frac{\Delta_c}{2}\tilde{k}^{1/2}\left(\delta_{ij} - e_i^v e_j^v\right)\frac{\partial\tilde{Z}}{\partial x_j}, \tag{2.11}$$

where

$$\tilde{k} = \int_{k_c}^{\infty} E(k)\mathrm{d}k \tag{2.12}$$

is the subgrid kinetic energy, $\mathbf{e} = [e_1, e_2, e_3]$ is the unit vector of the subgrid vortex axis, and Δ_c is the subgrid cutoff scale, here taken to be equal to the grid spacing Δx. The largest resolved wave number is then $k_c = \pi/\Delta_c$. The energy spectrum for the Lundgren spiral vortex is

$$E(k) = \mathcal{K}_0\epsilon^{2/3}k^{-5/3}\exp[-2k^2\nu/(3|\tilde{\alpha}|)], \tag{2.13}$$

where $\mathcal{K}_0$ is the Kolomogorov prefactor, ϵ is the local cell-averaged dissipation rate, and

$$|\tilde{\alpha}| = \tilde{S}_{ij}e_i^v e_j^v \tag{2.14}$$

is the axial strain along the subgrid vortex axis.

$$\tilde{S}_{ij} = \frac{1}{2}\left(\frac{\partial\tilde{u}_i}{\partial x_j} + \frac{\partial\tilde{u}_j}{\partial x_i}\right) \tag{2.15}$$

is the resolved rate-of-strain tensor. The factor $\mathcal{K}_0\epsilon^{2/3}$ is estimated from the local, resolved-scale, second-order velocity structure function $\tilde{F}_2(r;\mathbf{x})$ (Metais & Lesieur, 1992; Voelkl et al., 2000),

$$\mathcal{K}_0\epsilon^{2/3} = \frac{\tilde{F}_2}{A\Delta^{2/3}}, \tag{2.16}$$

with,

$$A = 4\int_0^{\pi} s^{-5/3}\left(1 - \frac{\sin s}{s}\right)\mathrm{d}s \approx 1.90695. \tag{2.17}$$

A local spherical average is used to estimate $\tilde{F}_2$,

$$\tilde{F}_2(\Delta;\mathbf{x}) = \frac{1}{6}\sum_{j=1}^{3}\left(\delta\widetilde{u_1^+}^2 + \delta\widetilde{u_2^+}^2 + \delta\widetilde{u_3^+}^2 + \delta\widetilde{u_1^-}^2 + \delta\widetilde{u_2^-}^2 + \delta\widetilde{u_3^-}^2\right)_j, \tag{2.18}$$

where

$$\delta\widetilde{u_i^{\pm}} = \widetilde{u}_i(\mathbf{x} + \mathbf{e}_j\Delta) \pm \widetilde{u}_i(\mathbf{x}) \tag{2.19}$$

is the velocity difference of component u_i in direction x_j at $\mathbf{x}$. This allows the SGS terms to be estimated dynamically only from the local instantaneous resolved fields without performing any temporal or spatial averages.

The SGS scalar mixing model, which is of particular interest here, is based on an analytical solution of the Navier–Stokes equations for the winding of the scalar field by the subgrid vortex (Lundgren, 1982; Pullin, 2000; Pullin & Lundgren, 2001). The anisotropic SGS mixing of the scalar by the vortex results in a tensor eddy-diffusivity model for the SGS scalar flux (Eq. 2.11). In LES of isotropic turbulence with an imposed mean scalar gradient, Pullin (2000) predicted the expected behavior for the normalized scalar variance as a function of the Taylor Reynolds number (Dimotakis, 2000). The model has also been applied to two-fluid mixing in Rayleigh–Taylor (Mattner et al., 2004) and Richtmyer–Meshkov (Hill et al., 2006) instabilities.

2.3 Numerical method

The numerical method is discussed in detail in Hill & Pullin (2004) and Pantano et al. (2007). The main features of the numerical method will be summarized here. The conservation equations are discretized on a regular Cartesian mesh using the second-order accurate, collocated tuned center-difference (TCD) scheme of Hill & Pullin (2004). The center-difference scheme uses a bandwidth-optimized five-point stencil constructed to minimize the spatial truncation error for the Navier–Stokes equations for a von Kármán spectrum (Ghosal, 1996, 1999).

The hybrid method of Hill & Pullin (2004) was developed for the simulation of flows with discontinuities, such as shock waves, and can switch to an upwinding weighted essentially non-oscillatory (WENO) scheme (Liu et al., 1994) from the centered differences in a cell-based fashion. In this study, all flows simulated were subsonic and WENO was not used in any part of the flow domain.

Both the finite differences and WENO are implemented with conservative flux-based discretizations (Rai, 1986) and formulated in energy-conserving form (Zang, 1991; Honein & Moin, 2004), with stable boundary closures (Strand, 1994). Inflow and outflow boundary conditions on planes aligned with the grid are implemented in characteristic form, as suggested by Thompson (1987) and Poinsot & Lele (1992). A third-order strong stability preserving (SSP) Runge–Kutta method (Gottlieb et al., 2001) is used for time stepping.

2.4 Implicit geometry representation

Geometrical features of the flow domain that are not aligned with the regular Cartesian mesh are implicitly represented by a level set function (Osher & Sethian, 1988), $\phi(t, x, y, z)$. Figure 2.1 shows a configuration of a two-dimensional grid intersected by the contour of $\phi(t, x, y) = 0$, which defines

the boundary of the physical domain, $\partial\Omega_{\mathrm{f}}$. The level-set function is defined as the signed distance from the boundary $\partial\Omega_{\mathrm{f}}$. The computational cells are divided into two groups, depending on the sign of the distance function $\phi(x_i, y_j, z_k)$ at the center of each cell, with the physical cells (fluid domain, Ω_{f}) having positive distance from the boundary and ghost cells at negative distance (ghost fluid domain, Ω_{g}).

The vector of state in the ghost cells is not part of the solution, and can even assume non-physical values. The thin layer of ghost cells adjacent to the boundary is used to apply the desired boundary condition on $\partial\Omega_{\mathrm{f}}$. This method of applying the boundary condition was first introduced by Fedkiw et al. (1999) and is known as the ghost fluid method (GFM). The band of cells that are modified in the ghost fluid is chosen to be wide enough to ensure that stencils centered on cells in the physical domain will not reach beyond this band of ghost cells, for the simulations in the current study are three cells deep in each direction in order to accommodate calculation of quantities used by the LES model.

The GFM method allows the governing equations to be solved on a Cartesian mesh without the need to generate boundary-conforming grids. The solution in the entire computational domain, physical and ghost fluid, is updated by the solver at each time step, thus avoiding the stability constraints associated with the generation of arbitrary small "cut cells" where the boundary intersects the regular Cartesian grid. Moreover, computational complexity is reduced since ghost fluid cells require no special treatment by the integration algorithm.

2.4.1 No-penetration boundary condition—Slip wall

For the current simulations, two types of boundary conditions have to be imposed: a no-penetration condition on solid walls (slip wall) and an inflow condition for the injection ramp. The linear extrapolation or mirroring described in Arienti et al. (2003) is used to populate the ghost cells in the case of the no-penetration condition. The goal here is to construct ghost-cell states such that the interpolated normal component to the boundary velocity component is zero. For each ghost cell at $\mathbf{x}_{\mathrm{g}}$ the mirror image $\mathbf{x}_{\mathrm{g}'}$ is found and then the vector of state $\mathbf{U}(\mathbf{x}_{\mathrm{g}'})$ is interpolated at $\mathbf{x}_{\mathrm{g}'}$ from the neighboring cells in the physical domain (Fig. 2.1). The value $\mathbf{U}(\mathbf{x}_{\mathrm{g}})$ is then computed by inverting the sign of the normal velocity component of $\mathbf{U}(\mathbf{x}_{\mathrm{g}'})$ with respect to $\partial\Omega_{\mathrm{f}}$.

2.4.2 Subsonic-inflow boundary condition

The perforated ramp is modeled as a uniform subsonic inflow to avoid the resolution requirements imposed by the fine scales produced by the small holes. In this case, the ghost cells must be filled with values corresponding to a prescribed mass flux through the subsonic-inflow plane while preserving the well-posed character (in the sense that it should lead no drifting in the mean flow fields with respect

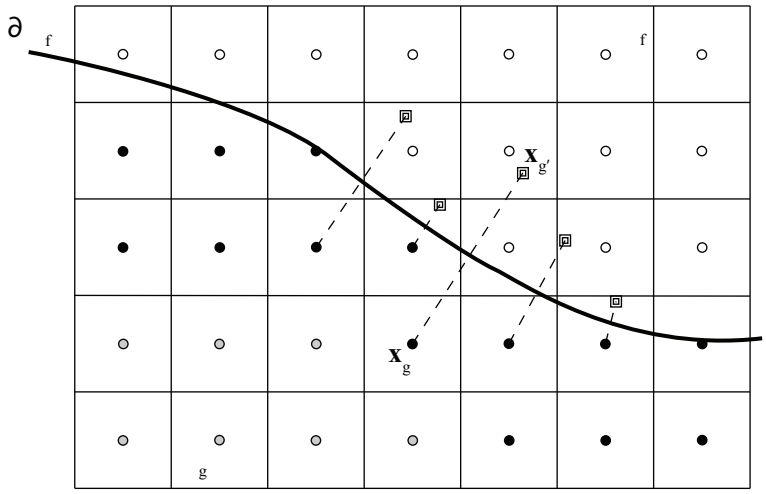

- Cell in the physical domain
- Cell in the ghost fluid domain
- Ghost cell used in the application of boundary condition
- Mirror points corresponding to ghost cells

Figure 2.1: Schematic showing a two-dimensional computational grid intersected by a level set defined boundary, $\partial\Omega_{\mathrm{f}}$ (thicker line). The grid is divided in two regions, the physical domain (Ω_{f}) and the ghost fluid (Ω_{g}). Filled black circles denote the band of cells adjacent to the boundary that have to be populated by the ghost fluid method, assuming here that the width of the stencil is 5 cells. The mirror points, $\mathbf{x}_{\mathrm{g}'}$, of $\mathbf{x}_{\mathrm{g}}$, with respect to the boundary, are also shown (squares) for some of the ghost cells.

to time) of the overall discrete method. A method akin to the ones used for finite-volume schemes (Wesseling, 2001) was chosen to fill the ghost cells that accounts for the outgoing characteristic.

The number of "Euler" boundary conditions that must be prescribed at a subsonic inflow boundary is equal to the number of the incoming characteristics, that is, four in three-dimensional flow. In the experiments, the mass flux through the ramp is fixed by the flow through a sonic valve supplying an upstream plenum. Therefore the density and the velocity vector in the ghost cells are set to constant values corresponding to the set mass flux of the lower stream. An extrapolation along the outgoing characteristic is carried out to completely determine the vector of state in the ghost cells.

When the computational grid conforms to the boundary, the extrapolation is between the two adjacent cells on either side of the boundary, however, here the extrapolation must be adapted to the GFM implementation. The method as is implemented supplies a list of mirror pairs, $(\mathbf{U}(\mathbf{x}_{\mathrm{g}}), \mathbf{U}(\mathbf{x}_{\mathrm{g}'}))$, thus the extrapolation is from $\mathbf{x}_{\mathrm{g}'}$ to $\mathbf{x}_{\mathrm{g}}$. This may cause a degradation in accuracy if the distance of $\mathbf{x}_{\mathrm{g}'}$ from the boundary is large. In practice, the flow within several cells downstream of the inflow is uniform, thus extrapolating using the values at the mirror points does not cause any noticeable deleterious effects in the particular configuration of interest.

The conservative-variables vector of state

$$\mathbf{U} = [\rho,\ \rho u_1,\ \rho u_2,\ \rho u_3,\ E,\ \rho Z]^{\mathrm{T}} \tag{2.20}$$

must be prescribed inside the ghost fluid. Setting the density and the velocity vector to constant values corresponding to the mass flux through the ramp leaves the total energy, E, to be computed by extrapolation along the outgoing invariant. For the calculation of the total energy in the ghost cells, first the outgoing Riemann invariant is considered,

$$\mathcal{R}_5 = u + \frac{2}{\gamma - 1}c, \tag{2.21}$$

where c is the speed of sound and u is the velocity component normal to the inflow boundary. The speed of sound in the ghost cell is

$$c_{\mathrm{g}} = \frac{\gamma - 1}{2}\left(u_{\mathrm{g}} + \frac{2}{\gamma - 1}c_{\mathrm{g}'} - u_{\mathrm{g}'}\right), \tag{2.22}$$

which is used to compute the unknown total energy

$$E_{\mathrm{g}} = \rho_{\mathrm{g}}\left[\frac{1}{\gamma(\gamma - 1)}c_{\mathrm{g}}^2 + \frac{1}{2}\left(u_{\mathrm{g}}^2 + v_{\mathrm{g}}^2 + w_{\mathrm{g}}^2\right)\right], \tag{2.23}$$

where v and w are the two tangential to the boundary components of the velocity vector.

Due to the continuous update of the ghost fluid cells adjacent to the boundary, so that the boundary condition on the boundary is satisfied at the beginning of each time step, the flow in the interior ghost fluid can be quite severe and even unphysical. Nevertheless, the integration algorithm does not distinguish between the physical fluid and the ghost fluid, therefore, in order to avoid a breakdown or "blowup" of the integration, the dissipative WENO scheme is used to advance the solution (only) in the ghost fluid.

Although integrating the entire domain has many advantages from an algorithmic point of view, it may negatively affect the performance of the overall simulation by restricting the time step in the case of some unusual flow feature developing in the ghost fluid region. In this work, there is no evidence that the time step is restricted by the ghost fluid, possibly because the geometry of the simulation domain is not particularly complex.

2.5 Implementation framework

The flow solver described, including the SGS model and the GFM implementation, exists at the bottom of an adaptive mesh refinement (AMR) controller called AMROC (Deiterding, 2003, 2004)

that provides a generic infrastructure for the solution of hyperbolic problems and handles mesh adaptation, message-passing in parallel architectures, and most of the IO responsibilities in a relatively transparent manner. In this study, the AMR capability of AMROC was not employed because the gain in computational efficiency from using the AMR capability was not significant compared to non-adaptive simulations.

Chapter 3

Verification

The American Institute of Aeronautics and Astronautics defines verification as follows (AIAA, 1998):

Definition 1 (Verification) *The process of determining that a model implementation accurately represents the developer's conceptual description of the model and the solution to the model.*

The model in the case of computational fluid dynamics is, typically, a set of differential equations with the corresponding boundary conditions. Computational simulation seeks solutions to the conceptual model by converting the continuum equation(s) to a discrete model and then applying a suitable computational algorithm. Verification provides substantiation that the technique of computing the solution is correct. Since the method of acquiring numerical solutions is comprised of a mathematics part, discretizing the continuum equations, and a computer-science part, implementing (that is programming) a suitable algorithm, verification has two fundamental aspects: solution verification and code verification. In this work, the distinction is not made between the two since all the verification techniques applied test both the discretization and the computer program.

From the definition of the verification process, it is evident that the model is not required to describe any real-world physics. The assessment of the accuracy of a model in predicting experimental data is undertaken by the validation process. The definition of validation according to AIAA (1998) is given here for completeness:

Definition 2 (Validation) *The process of determining the degree to which a model is an accurate representation of the real world from the perspective of the intended uses of the model.*

Model validation will be discussed in the next chapter.

As is stated in the definition by AIAA (1998), verification for a computer code is a process, with the consequence that there is no single test, or a set of tests, that will render a code verified. However, a thorough verification program should be able to assess all key elements of the schemes and algorithms used such that there will be a high level of confidence in the correctness of the computed solutions as a result. This task poses many difficulties, because parallel to the exponential growth

in computer performance there has been a similar growth in program size and complexity (Post & Votta, 2005), which makes the challenge of verifying a code with tens or hundreds of thousands of lines in which multi-physics models are involved considerable (Hatton, 1997).

Verification techniques in computational fluid dynamics can rely on grid convergence, order of accuracy, Richardson extrapolation, and comparison to benchmark solutions. Numerical results can also be compared against known analytical solutions or against fictitious manufactured solutions (Knupp & Salari, 2003; Steinberg & Roache, 1985). A number of reviews have compiled these and other techniques to assess program code accuracy (Knupp & Salari, 2003; Oberkampf & Trucano, 2002; Roache, 1998; Roy, 2005).

In the simulations of the reattaching shear layer, the unsteady, compressible, filtered Navier–Stokes equations are integrated numerically. Verification of the solver would require using a viscous flow as a test case. However, in the high Reynolds number flows of interest, the viscous terms are much smaller than the convective and subgrid terms and will be neglected for the purposes of verifying the solver.

Our experience has showed that, because of their lack of dissipation terms, the Euler equations are a very good test for verification purposes. In the turbulence simulations considered, the LES model has a stabilizing action on the under-resolved flow and can also act to stabilize mild instabilities that may be produced by the numerical scheme. Therefore, although the Euler equations are missing some of the physics of the Navier–Stokes equations, they constitute a strict test for the numerical scheme.

3.1 Exact solution of the Euler equations using periodic boundary conditions

The simple two-dimensional vortical solution of the Euler equations with periodic boundary conditions in both dimensions employed by Balsara & Shu (2000) was used to study the convergence of the interior stencil. The tangential velocity distribution is

$$u_\theta(r) = r\exp(-r^2), \tag{3.1}$$

where r is the radial coordinate from the center of the vortex. Assuming a perfect gas equation of state, from the radial momentum equation the pressure distribution is

$$p(r) = p_0\left[1 - \frac{\gamma-1}{\gamma}\frac{\rho_0}{4p_0}\exp(-2r^2)\right]^{\frac{\gamma}{\gamma-1}}, \tag{3.2}$$

where, p_0 and ρ_0 are the free-stream pressure and density respectively. The density is computed from the pressure and the free-stream state, $p/\rho^\gamma = p_0/\rho_0^\gamma$. For the test presented here $\rho_0 = 1$ and $p_0 = 2$.

A passive scalar distribution of the form

$$Z(r) = \exp(-r^2), \tag{3.3}$$

is superimposed on the velocity field in order to assess the solution of the passive scalar transport equation.

The flow is computed on a grid of $[-5, 5] \times [-5, 5]$ units. The vortex radius is about one unit. The computation is initialized with Eqs. 3.1, 3.2 and 3.3 and computed to time $t/t_\mathrm{r} = 1$ using the second-order-accurate tuned-centered-difference (TCD) stencil. t_r is the time of a single revolution of the vortex and is defined as

$$t_\mathrm{r} = 2\pi r/u_\theta(r), \tag{3.4}$$

with $r = 1$.

Convergence is assessed by computing the L_∞ and L_1 norms of the error at $t/t_\mathrm{r} = 1$ for mass, momentum, total energy and, mixture fraction for four grid resolutions. Because the solution and discretization are symmetric in the x and y directions, errors in x and y momentum are identical and a distinction between the two is not made here. The grid was refined by a factor of 2 in each dimension, starting with a coarse grid of 128 cells and leading to a finest at 1024 cells, in each direction.

The expected second-order convergence is observed for all quantities as can be seen in Fig. 3.1 and Table 3.1.

	Mass		Momentum		Energy		Mixture fraction	
N	Log Error	Rate	Log Error	Rate	Log Error	Rate	Log Error	Rate
128	-5.73		-4.38		-3.77		-3.73	
256	-7.21	2.14	-5.74	1.96	-5.24	2.11	-5.10	1.98
512	-8.61	2.02	-7.12	1.99	-6.64	2.02	-6.50	2.02
1024	-10.00	2.00	-8.51	2.00	-8.03	2.00	-7.88	1.99

Table 3.1: L_1 convergence rates for the vortex test case

The velocity distribution of the vortex is unstable to axisymmetric disturbances. The Rayleigh discriminant (e.g., Drazin & Reid, 2004) defined by

$$\Phi(r) = \frac{1}{r^3}\frac{\mathrm{d}}{\mathrm{d}r}(r^2\Omega)^2, \tag{3.5}$$

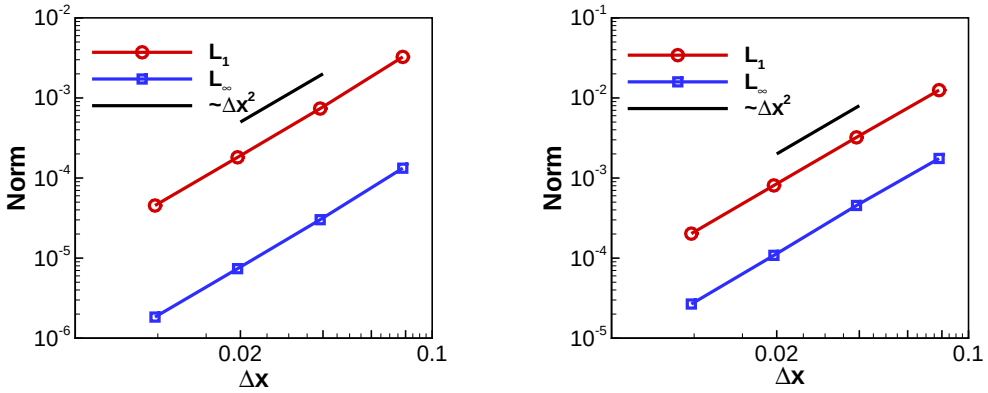

(a) Mass

(b) Momentum

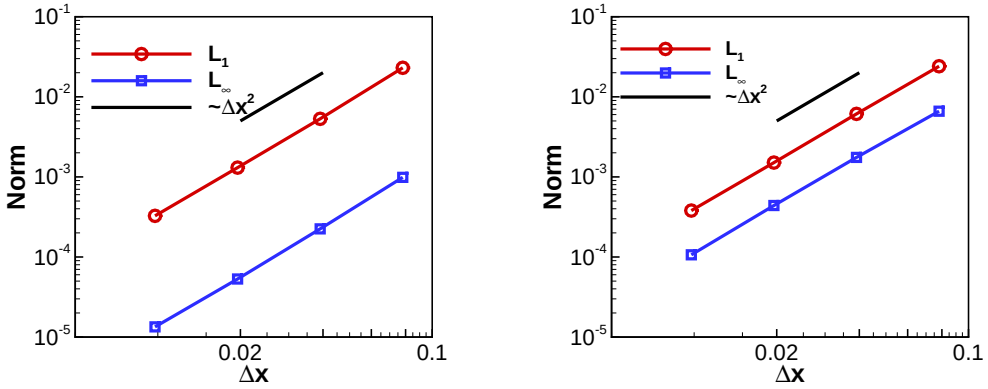

(c) Energy

(d) Mixture fraction

Figure 3.1: L_1 and L_∞ norm of the error versus grid spacing for mass, momentum, energy, and mixture fraction for the vortex test case with periodic boundary conditions

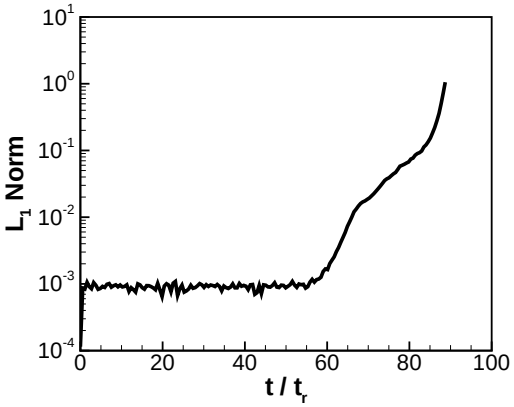

Figure 3.2: L_1 norm of the density error versus time for a grid resolution of 256×256. A unit of normalized time t/t_r corresponds to about one vortex revolution.

where $\Omega(r) = \exp(-r^2)$ is the angular velocity distribution of the vortex, is negative for $r > 1$. A necessary and sufficient condition for stability to axisymmetric disturbances is that the square of the circulation does not decrease anywhere, that is, $\Phi \geq 0$.

Although the initial condition has no perturbations, the accumulation of numerical error after sufficient time causes the flow to become unstable and the numerical integration eventually fails. Figure 3.2 shows the L_1 norm of the error in density with respect to time. At the resolution of 256×256 it takes about 60 revolutions of the vortex before the instability develops. The norms in the convergence study were computed after one revolution, well before the instability develops.

3.2 Verification of the passive scalar diffusion term implementation

In order to verify the implementation of the diffusion term in the passive scalar equation, a two-dimensional diffusion problem for the scalar is considered. The initial condition has a scalar concentration in polar coordinates (r, θ),

$$Z(r, \theta, t = 0) = \exp[-(\sin 8\theta + 2)(r/r_0)^2], \tag{3.6}$$

with $r_0 = 1$. The velocity vector is set to zero and the density and pressure are uniform. The equations of motion and the equation for the scalar are integrated up to a time of $t_{\text{final}}\ D/r_0^2 = 0.035$, where D is the diffusion coefficient of the passive scalar. The initial and final concentration fields are shown in Fig. 3.3.

Since there is no exact solution for the evolution of $Z(x, y, t)$ the observed order of accuracy is calculated following Roy (2005). The method for calculating the observed order of accuracy is similar to Richardson extrapolation (Richardson, 1910, 1927), however, unlike Richardson extrapolation, the order of accuracy of the scheme does not need to be assumed.

Consider three grids with uniform grid spacing Δx_1, Δx_2, and Δx_3, having a constant refinement factor, $h > 1$,

$$h = \frac{\Delta x_2}{\Delta x_1} = \frac{\Delta x_3}{\Delta x_2}, \tag{3.7}$$

or

$$\Delta x_1 = \Delta x, \quad \Delta x_2 = h\Delta x, \quad \Delta x_3 = h^2\Delta x. \tag{3.8}$$

If the solution of $Z(x, y, t)$ at t_{final} is accurate to order p, then the solutions on the three grids can be expressed as a function of the exact solution Z_{exact}, a coefficient of the error, g_p, and the grid

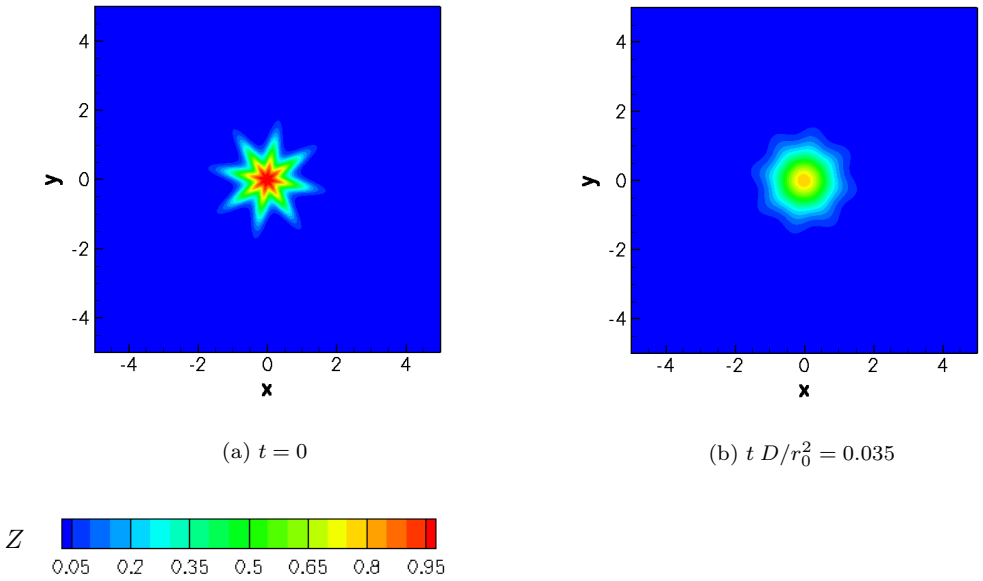

(a) $t = 0$

(b) $t\ D/r_0^2 = 0.035$

Figure 3.3: Initial condition for the passive scalar diffusion test case (left) and the scalar distribution at the end of the integration

spacing, Δx:

$$Z_1(x, y, t_{\text{final}}) = Z_{\text{exact}}(x, y, t_{\text{final}}) + g_p(x, y, t_{\text{final}})\Delta x^p + O\left(\Delta x^{p+1}\right) \tag{3.9}$$

$$Z_2(x, y, t_{\text{final}}) = Z_{\text{exact}}(x, y, t_{\text{final}}) + g_p(x, y, t_{\text{final}})(h\Delta x)^p + O\left([h\Delta x]^{p+1}\right) \tag{3.10}$$

$$Z_3(x, y, t_{\text{final}}) = Z_{\text{exact}}(x, y, t_{\text{final}}) + g_p(x, y, t_{\text{final}})(h^2\Delta x)^p + O\left([h^2\Delta x]^{p+1}\right). \tag{3.11}$$

Neglecting higher-order terms and solving in terms of p, yields the observed order of accuracy,

$$p = \frac{\ln\left(\frac{Z_3 - Z_2}{Z_2 - Z_1}\right)}{\ln(h)}. \tag{3.12}$$

The diffusion problem for the scalar was computed for four grid resolutions having $h = 2$ as shown in Table 3.2. Because the expressions for the error in Eqs. 3.9–3.11 are asymptotic with respect to $\Delta x \to 0$, relatively fine grids were used to compute the solution. The computational domain has a size of $[-5, 5] \times [-5, 5]$ units.

The observed order of accuracy calculated using the L_1, L_2, and L_∞ norms of the difference

N	Solution
256	$Z_4(x, y, t_{\text{final}})$
512	$Z_3(x, y, t_{\text{final}})$
1024	$Z_2(x, y, t_{\text{final}})$
2048	$Z_1(x, y, t_{\text{final}})$

Table 3.2: Number of cells along each direction, N, and the corresponding approximate solutions at t_{final}

$Z_m - Z_n$. For solutions Z_1–Z_3 yields:

$$p = \frac{\ln\left(\frac{\|Z_3 - Z_2\|_1}{\|Z_2 - Z_1\|_1}\right)}{\ln(2)} = 1.9998 \tag{3.13}$$

$$p = \frac{\ln\left(\frac{\|Z_3 - Z_2\|_2}{\|Z_2 - Z_1\|_2}\right)}{\ln(2)} = 1.9999 \tag{3.14}$$

$$p = \frac{\ln\left(\frac{\|Z_3 - Z_2\|_\infty}{\|Z_2 - Z_1\|_\infty}\right)}{\ln(2)} = 2.0011 \tag{3.15}$$

Also, for solutions Z_2–Z_4,

$$p = \frac{\ln\left(\frac{\|Z_4 - Z_3\|_1}{\|Z_3 - Z_2\|_1}\right)}{\ln(2)} = 1.9987 \tag{3.16}$$

$$p = \frac{\ln\left(\frac{\|Z_4 - Z_3\|_2}{\|Z_3 - Z_2\|_2}\right)}{\ln(2)} = 1.9989 \tag{3.17}$$

$$p = \frac{\ln\left(\frac{\|Z_4 - Z_3\|_\infty}{\|Z_3 - Z_2\|_\infty}\right)}{\ln(2)} = 1.9989 \tag{3.18}$$

The observed order of accuracy agrees with the order of accuracy of the scheme.

3.3 Assessment of the solver using correlations with linear stability analysis

The vortical flow considered in Section 3.1 is sufficient to establish convergence of the interior scheme, however, it is rather simple and non-representative of the turbulent shear flow and, more importantly, does not assess the performance of the boundary closure. For this reason, an unsteady and spatially developing flow is used to assess those aspects of the code.

While the number of exact solutions to the Euler equations is limited, linear stability analysis (LSA) can provide solutions *subject to certain approximations*. Previous comparisons of numerical codes with results from linear stability analysis were performed by Cook & Dimotakis (2001), Kaiktsis & Monkewitz (2003), and Ravier et al. (2006). In these studies, growth is temporal. Only Cook &

Dimotakis (2001) performed a comparison with a Navier–Stokes solver that includes the non-linear terms.

In the present study, the LSA solution for a spatially developing shear layer is used because of the simplicity of the basic flow and the similarity to the turbulent shear flow of interest. Spatially developing, inviscid, compressible shear layers are computed using the present computational framework. The flow is forced at the inflow using the eigenfunctions and the corresponding frequency of the most unstable mode as computed from LSA. This is a common way for providing initial/boundary conditions or perturbations to shear flows (e.g., Colonius et al., 1997).

Direct comparison of the numerically computed solution with the LSA result presents many challenges. There are many reasons why the computed solution from an Euler solver may differ from the LSA solution. Solution of the boundary value (LSA) and the initial value (Euler solver) problem may not yield the same result, differences can be due to limitations of the boundary conditions, as a consequence of the practical difficulties associated with comparing an exponentially growing field, or because of differences in the basic flow.

Since the goal of comparison between the LSA prediction and the solution from an Euler solver is to assess computer code accuracy, a detailed listing and analysis of the reasons leading to differences of the two solutions becomes of limited importance. LSA can be used to compute unstable perturbations to a flow, which are then used to force the flow computed by the solver been assessed.

Therefore, the question posed here is different than determining whether a numerical solution converges to an analytical exact solution of the equations. That is, instead of attempting to obtain a hard measurement of the numerical error, one can attempt to determine how close the numerical solution is to the *expected prediction* from LSA. The value of such a metric, however, can be lower than that provided by convergence and accuracy tests since a solution that appears to be approaching an exact solution may ultimately not even be a mathematically consistent one. As a complement to traditional error metrics, one can exploit statistical metrics.

The closeness of the solutions can be measured in a number of ways, through projection techniques (Powell, 1981) to two-point correlations (Goldberg, 1960; McDonald, 1985). For the purpose of solver assessment, correlations can be used in a manner akin to that of identification techniques in image processing where geometrical shapes are identified by correlating an image against all possible sizes, orientations and positions of the corresponding primitive (e.g., Partridge, 1991).

3.3.1 Linear stability solution

The stability of laminar shear flows has been considered in many studies. Michalke (1964) studied the stability of the temporally growing shear layer with a hyperbolic tangent profile, Lessen et al. (1965, 1966) considered compressible temporal shear layers under the assumption that the flow is iso-energetic (the total enthalpy is constant), while Blumen (1970), Blumen et al. (1975), and

Drazin & Davey (1977) assumed that the thermodynamic state of the flow is constant. Discussion of a secondary instability in three-dimensional shear layers appearing as streamwise counter-rotating vortices can be found in Metcalfe et al. (1987). In this work, the LSA solution for inviscid compressible free and confined spatial shear layers by Zhuang et al. (1990a,b) is utilized. Their method for deriving the stability characteristics for compressible spatial shear layers is summarized here. The reader is referred to Zhuang et al. (1990a,b) for details on deriving the stability characteristics and to Matheou et al. (2008) for the use of the present LSA solution for verification.

Consider a two-dimensional flow of two parallel steams. All quantities can be written as a basic profile $\bar{Q}(y)$ plus a perturbation:

$$Q(x, y, t) = \bar{Q}(y) + Q'(x, y, t). \tag{3.19}$$

Disturbance quantities denoted by primes can be written as an eigenmode expansion,

$$Q' = f(y) \exp[i(\alpha x - \omega t)]. \tag{3.20}$$

For spatially growing fluctuations, like the ones considered here, ω is a real frequency and $\alpha = \alpha_\mathrm{r} + i\ \alpha_\mathrm{i}$ a complex wave number. The corresponding complex wave velocity can then be written as $c = \omega/\alpha$.

Substituting the expressions for the disturbance quantities into the compressible Euler equations and neglecting quadratic and higher-order terms yields a system of ordinary differential equations for the amplitude functions. These equations can be reduced to a single equation for the pressure disturbances.

For a given disturbance frequency, ω, and a basic flow, the solution of the boundary-value problem for the pressure eigenfunction gives the complex eigenvalue, α. The eigenfunctions for the velocity and density can then be expressed as functions of the pressure eigenfunction and its derivatives and the complete two-dimensional field can then be constructed.

A shooting Runge–Kutta–Fehlberg method is used to solve the eigenvalue problem by matching the asymptotic boundary conditions away from the shear layer. Even though analytical solutions are generally preferred for verification, numerical solution methods of ordinary differential equations are well developed and solution techniques are reliable. The numerical solutions of the eigenfunctions are obtained independently of the code being verified, with a typical error of $O(10^{-6})$.

3.3.2 Correlation metric

The correlation r, between the computed perturbation field u'_comp and the corresponding field from the LSA, u'_LSA, is given by,

$$r = \frac{\langle u'_\mathrm{comp}\, u'_\mathrm{LSA} \rangle}{\langle u'^2_\mathrm{comp} \rangle^{1/2} \langle u'^2_\mathrm{LSA} \rangle^{1/2}}, \tag{3.21}$$

where,

$$\langle \bullet \rangle = \int_V \bullet \, \mathrm{d}\mathbf{x}. \tag{3.22}$$

The LSA perturbation field is

$$f(y)\ \mathrm{e}^{-\alpha_\mathrm{i} x + i\alpha_\mathrm{r}(x-x_0)}, \tag{3.23}$$

where the complex eigenfunction f is a function of the vertical coordinate y and also depends implicitly on the mode α, with x_0 a phase shift that will be treated as an independent variable. If a numerical code is correct and the flow is perturbed with the most amplified mode, the correlation r will have a maximum at the value of the most amplified mode.

This correlation may be computed in two different ways. One may assume that near the most amplified mode the shape of the eigenfunction f does not change significantly and neglect the dependence on α. In this case, r is computed for all values of the three-dimensional parameter space α_r, α_i, and x_0, i.e.,

$$r_1(\alpha_\mathrm{r}, \alpha_\mathrm{i}, x_0) = \frac{\langle u' f(y)\ \mathrm{e}^{-\alpha_\mathrm{i} x + i\alpha_\mathrm{r}(x-x_0)} \rangle}{\langle u'^2 \rangle^{1/2} \langle \big(f(y)\ \mathrm{e}^{-\alpha_\mathrm{i} x + i\alpha_\mathrm{r}(x-x_0)} \big)^2 \rangle^{1/2}}. \tag{3.24}$$

An alternative is to keep the dependence of the eigenfunction f on the mode α and compute r for values of α along the dispersion relation. In this case, the value of x_0 can be left as a free parameter that can be varied, i.e.,

$$r_2(\alpha(\omega), x_0) = \frac{\langle u' f(\alpha; y)\ \mathrm{e}^{-\alpha_\mathrm{i} x + i\alpha_\mathrm{r}(x-x_0)} \rangle}{\langle u'^2 \rangle^{1/2} \langle \big(f(\alpha; y)\ \mathrm{e}^{-\alpha_\mathrm{i} x + i\alpha_\mathrm{r}(x-x_0)} \big)^2 \rangle^{1/2}}. \tag{3.25}$$

3.3.3 Flow description

The shear layer is assumed to be formed between two parallel streams of the same gas governed by the perfect-gas equation of state and subjected to a two-dimensional, spatially growing disturbance. We assume a hyperbolic-tangent basic velocity profile of the form,

$$\bar{u}(y)/U_1 = \eta(y) + u_\mathrm{r}(1 - \eta(y)), \tag{3.26}$$

where $u_\mathrm{r} = U_2/U_1$ is the velocity ratio of the two streams, and

$$\eta(y) = \frac{1}{2}(1 + \tanh(y)). \tag{3.27}$$

As in Zhuang et al. (1990a,b), the Crocco–Busemann relation is used to obtain the temperature profile.

The most-amplified mode and the corresponding eigenfunctions are computed from the LSA and

used to force the shear layer at the inflow. For example, the streamwise velocity inflow condition is:

$$u(0, y, t) = \bar{u}(y) + \mathcal{A}\,(f_{\mathrm{r}}(y)\cos(\omega t) - f_{\mathrm{i}}(y)\sin(\omega t)), \tag{3.28}$$

where f is the complex streamwise velocity eigenfunction, $f = f_{\mathrm{r}} + i f_{\mathrm{i}}$, and $\mathcal{A}$ is the forcing amplitude. For the present study, the eigenfunctions were normalized such that the maximum of the absolute value of the real part of the streamwise velocity eigenfunction is unity,

$$\max_{y}(|f_{\mathrm{r}}(y)|) = 1. \tag{3.29}$$

Two-dimensional numerical simulations of two shear layers were performed. Shear Layer A is low-Mach-number flow, with a convective Mach number (Papamoschou & Roshko, 1988) of $M_{\mathrm{c}} = 0.09$. For shear layers composed of the same gas with matched static free-stream pressures and temperatures, the convective Mach numbers, $M_{\mathrm{c}1}$ and $M_{\mathrm{c}2}$, are the same from both streams and equal to

$$M_{\mathrm{c}} = \frac{(U_1 - U_2)/2}{a}, \tag{3.30}$$

where a is the common speed of sound of the two free streams. Shear Layer B has a supersonic top stream over a subsonic stream with $M_{\mathrm{c}} = 0.8$. Shear Layer A is unconfined whereas Shear Layer B is confined. Table 3.3 summarizes the conditions for the two cases.

Case	A	B
Transverse boundary	Unconfined	Confined
Top stream Mach number, M_1	0.2	2.133
Convective Mach number, M_{c}	0.09	0.8
Velocity ratio, U_2/U_1	0.5	0.25
Density ratio, ρ_2/ρ_1	1.	1.
Temperature ratio, T_2/T_1	1.	1.

Table 3.3: Flow conditions for the two shear layers

The computational domain has a streamwise length of 100 units and a transverse length of 40 units. The shear layer basic profiles are given by Eq. 3.26. Both cases are computed at four different resolutions to investigate convergence and the effect of grid spacing on the growth rate of the perturbation. Correlations and error metrics are computed up to a streamwise distance of $x = 80$, excluding thereby the region near the outflow boundary.

The computations are initialized with the LSA solution at time $t = 0$ and then the forcing is applied as an inflow perturbation. The amplitude of the forcing ($\mathcal{A}$ in Eq. 3.28) is $\mathcal{A} = 0.5 \times 10^{-4}\, U_1$ for both test cases. Figure 3.4 shows a comparison between the computed and the LSA streamwise velocity perturbation fields for Case A.

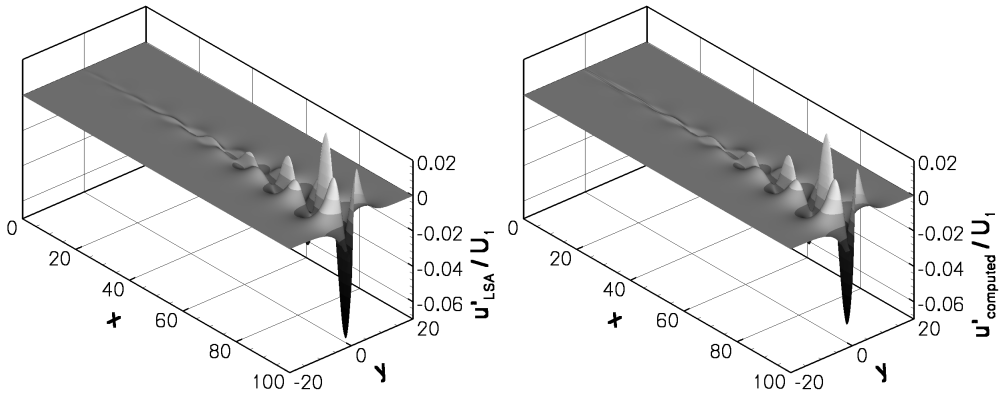

Figure 3.4: Streamwise velocity perturbation fields. The panel on the left depicts the linear stability analysis prediction and the one on the right the computed field for Case A, $\Delta x = 0.0625$ and $t = 20$. Note the exponential growth of the perturbation.

For the comparison of the solution between the full non-linear and linearized equations to be valid, perturbations must be sufficiently small such than the non-linear terms are much smaller than the linear terms throughout the domain. The validity of this assumption for the Euler equations is assessed by expressing the system of equations in terms of the primitive-variables vector of state

$$\mathbf{q} = [\rho \; u \; v \; T]^{\mathrm{T}} \tag{3.31}$$

as

$$\mathcal{M}(\mathbf{q}) = \mathcal{M}(\bar{\mathbf{q}}) + \mathcal{L}(\mathbf{q}') + \mathcal{N}(\mathbf{q}'), \tag{3.32}$$

where the terms linear in $\mathbf{q}'$, are in $\mathcal{L}(\mathbf{q}')$ and quadratic and higher-order terms in $\mathcal{N}(\mathbf{q}')$. The linearized equations are a valid approximation to the original set of equations if,

$$\|\mathcal{L}(\mathbf{q}')\| \gg \|\mathcal{N}(\mathbf{q}')\|. \tag{3.33}$$

For example, for the mass-conservation equation, we must have:

$$\left(\int |\mathcal{L}(\rho')|^2 \mathrm{d}\mathbf{x} \right)^{1/2} \gg \left(\int |\mathcal{N}(\rho')|^2 \mathrm{d}\mathbf{x} \right)^{1/2}. \tag{3.34}$$

The analytical LSA solution was used to compute the norms of the linear and non-linear contributions. Tables 3.4 and 3.5 show the results using the L_2 norm. The contribution of the non-linear terms in the momentum equations is always at least two orders of magnitude less than the linear terms. For both test cases, we will accept this as the proper metric for the validity of the linear approximation and that the LSA solution can be compared with the computed fields.

Equation	Linear	Non Linear	Ratio
Mass	1.41×10^{-1}	2.67×10^{-4}	522
x-momentum	$4.00\times10^{+1}$	5.50×10^{-3}	7300
y-momentum	$6.98\times10^{+1}$	3.28×10^{-3}	21265
Energy	5.62×10^{-1}	6.02×10^{-2}	9

Table 3.4: L_2 norms of the linear and non-linear terms for the unconfined, incompressible Shear Layer A

Equation	Linear	Non Linear	Ratio
Mass	1.40×10^{-2}	2.60×10^{-7}	53838
x-momentum	4.17×10^{-1}	3.31×10^{-5}	12604
y-momentum	1.26	1.85×10^{-5}	68184
Energy	1.78	8.37×10^{-3}	212

Table 3.5: L_2 norms of the linear and non-linear terms for confined, compressible Shear Layer B

3.3.4 Classical error metrics

Classical error metrics are computed based on the L_∞ norm. Figure 3.5 shows the error norms of the streamwise and transverse velocity perturbations at scaled time, $t = 20$. All times reported are normalized by the mean convective time, $t_c = L_x/U_c$, where L_x is the streamwise length of the computational domain and $U_c = (U_1 + U_2)/2$. The behavior of the error norms is substantially different in the two cases. For Shear Layer B, the error converges at the expected second-order rate. Unlike Case B, the error for Shear Layer A decreases rapidly at coarse resolution but tends to a constant for the finer grids. Two different kinds of error appear to dominate at low and high resolution. At large grid spacings, dispersion errors dominate, but as the grid spacing becomes smaller and all wavenumbers become sufficiently resolved, this type of error decreases rapidly. The analysis based on the correlation metric that follows shows that the perturbations in Case A grow at a different rate than the one predicted from LSA. Although the mismatch in the growth rate is quite small it is sufficient to destroy the convergence of the norms.

The observed different error norm behavior between the two cases cannot be attributed to code error since the identical code produces perfectly converging results for Case B. Quite likely, boundary condition implementation limitations leave an imprint on the solution that cannot be removed by mesh refinement alone. This hypothesis is consistent with the change in the type of characteristic boundary conditions from Case A to B, i.e., different number of characteristics specified at the boundary: subsonic (A) to supersonic (B). Since the local boundary treatment is based on one-dimensional projection methods, there is always possibility that waves transverse to the boundary remain close to it and that may contribute to a local contamination of the solution. The limitations and performance of the discrete boundary conditions for hyperbolic problems such as the one considered here are discussed in more detail in the review article by Colonius (2004).

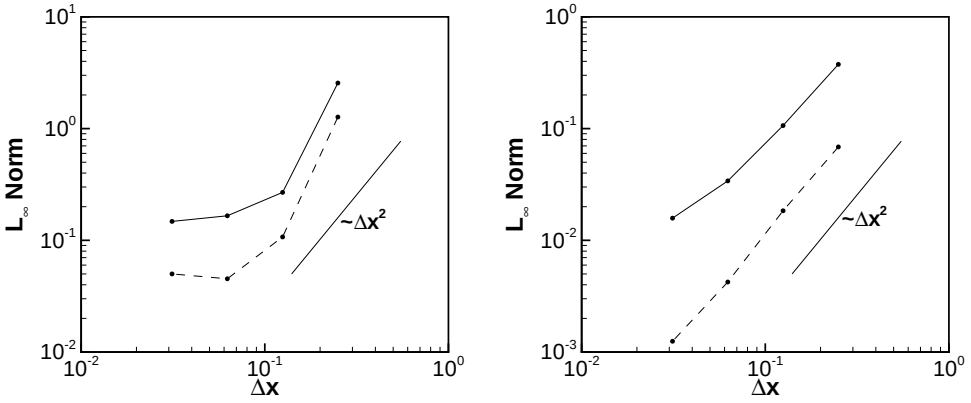

Figure 3.5: L_∞ norm of the error versus grid spacing for Shear Layer A (left) and B at $t = 20$. Solid lines correspond to the error norm of the streamwise velocity perturbation, u', and dashed to the transverse, v'. The error for Shear Layer A tends to a constant as grid spacing decreases due to a mismatch in the growth rate with the linear stability analysis prediction. Perturbations in Case B grow at the expected rate and the error converges at second-order rate.

3.3.5 Correlation metrics

The r_1 correlation is evaluated for both test cases for values of the three-dimensional parameter space $\alpha_\mathrm{r}, \alpha_\mathrm{i}$, and x_0. If the computed solution is identical with that from LSA, r_1 has a global maximum in a period of x_0 with a value of unity. In reality, the computed solution will be close to the analytical solution, but will not be identical. Thus a maximum of the correlation is sought and this yields the values of α_r, α_i, and x_0 at the maximum. Their values should be close to the exact values used to force the shear layer. Since this is an unsteady flow, the correlation is computed at various times. Its maximum value and the values $(\alpha_\mathrm{r}, \alpha_\mathrm{i}, x_0)$ at the maximum will actually vary with time. In this study, the correlation maximum was always found to be near the value of the most-unstable mode with which the shear layer was forced and the correlation maximum was very close to unity.

Figures 3.6 and 3.7 show results based on correlation r_1 for the streamwise velocity perturbation, u', and transverse velocity, v', at various grid spacings and times. The results can be seen to converge as the grid is refined with the value of the maximum of the correlation approaching unity, an indication that the shape of the perturbation field is the one predicted from the LSA.

Even though the correlation maximum is very close to unity for both cases, only in Case B does the growth rate converge to the value predicted by LSA. Perturbations in Shear Layer A appear to be growing at a slightly lower rate than expected. The discrepancy in the growth rate is about 1%.

Also shown in Figs. 3.6 and 3.7 is the real part of the mode, which appears to converge to the correct result. Tables 3.6 and 3.7 show results at a resolution of 1600×640 ($\Delta x = 0.0625$) at time $t = 20$.

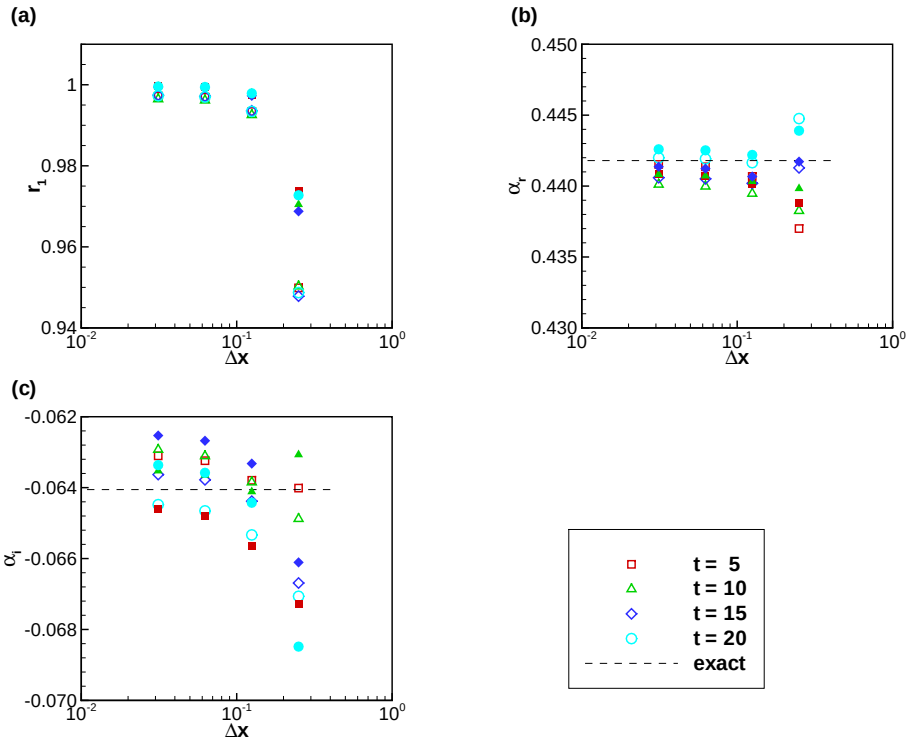

Figure 3.6: Results for Shear Layer A at different times and resolutions. Correlation r_1 (a), the real part of the mode, (b) and the imaginary part of the mode (c). Open symbols correspond to correlation with u' and filled symbols with v'

Scaled Time, t	Real Part	Imaginary Part	Correlation
exact	0.441798	-0.064055	-
Correlation with u'			
5.	0.441359	-0.063240	0.996917
10.	0.439975	-0.063110	0.996149
15.	0.440510	-0.063780	0.997158
20.	0.441920	-0.064655	0.996986
Correlation with v'			
5.	0.440709	-0.064812	0.999453
10.	0.440722	-0.063648	0.999467
15.	0.441230	-0.062678	0.999276
20.	0.442520	-0.063581	0.999457

Table 3.6: Comparison of the exact and computed real and imaginary parts of the most unstable mode for Shear Layer A for u' and v'. The grid resolution is 1600×640 ($\Delta x = 0.0625$).

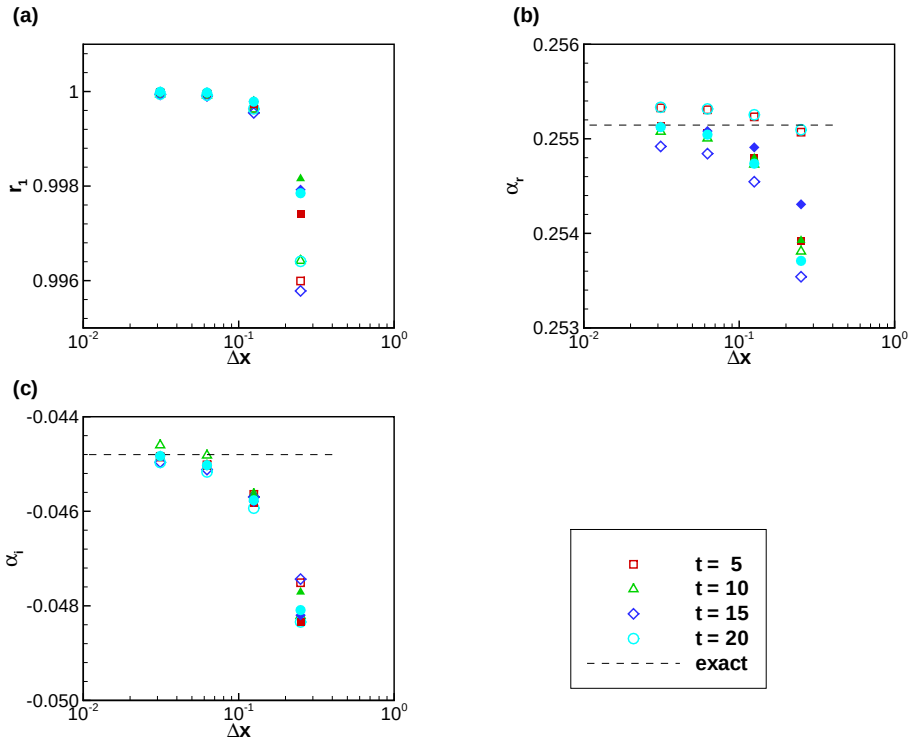

Figure 3.7: Results for Shear Layer B at different times and resolutions. Correlation r_1 (a), the real part of the mode, (b) and the imaginary part of the mode (c). Open symbols correspond to correlation with u' and filled symbols with v'

Scaled Time, t	Real Part	Imaginary Part	Correlation
exact	0.255145	-0.044802	-
Correlation with u'			
5.	0.255307	-0.045018	0.999941
10.	0.255005	-0.044818	0.999922
15.	0.254843	-0.045118	0.999908
20.	0.255316	-0.045169	0.999922
Correlation with v'			
5.	0.255064	-0.045047	0.999975
10.	0.255055	-0.045001	0.999980
15.	0.255081	-0.045030	0.999978
20.	0.255044	-0.045026	0.999978

Table 3.7: Comparison of the exact and computed real and imaginary parts of the most unstable mode for Shear Layer B for u' and v'. The grid resolution is 1600×640 ($\Delta x = 0.0625$).

As a way of visualizing the relationship between the computed and LSA perturbation fields, scatter plots of the computed u' and v' versus the LSA values are shown in Figs. 3.8 and 3.9 for $\Delta x = 0.0625$ and $t = 20$. Each point $(u'_{\text{LSA},\,ij}, u'_{\text{comp},\,ij})$ on the scatter plots represents the value of u' in the computational cell (x_i, y_j), $u'_{\text{comp},\,ij}$, and the LSA value, $u'_{\text{LSA},\,ij}$, at the same location and time. A closer look of Fig. 3.9 reveals that the computed solution for Case B grows slightly faster than the LSA predicted growth rate in accord with the results of Table 3.7.

The second type of correlation defined, r_2, is an implicit function of the disturbance frequency ω, in other words, this is a correlation along the dispersion relation. The eigenfunctions in this case are different for each value of $\alpha = \alpha(\omega)$. Figure 3.10 shows the values of the correlation r_2 as a function of the frequency for both shear layers at time $t = 20$ computed on a 1600×640 grid. As in the case of the r_1 correlation, the maximum occurs at the most unstable mode and the value of r_2 decreases significantly away from the most unstable mode.

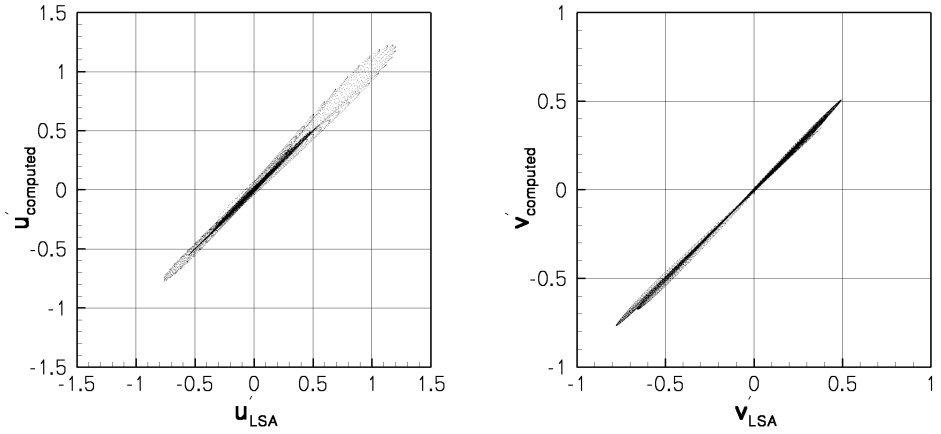

Figure 3.8: Scatter plots for u' (left) and v' for Shear Layer A, $\Delta x = 0.0625$ and $t = 20$

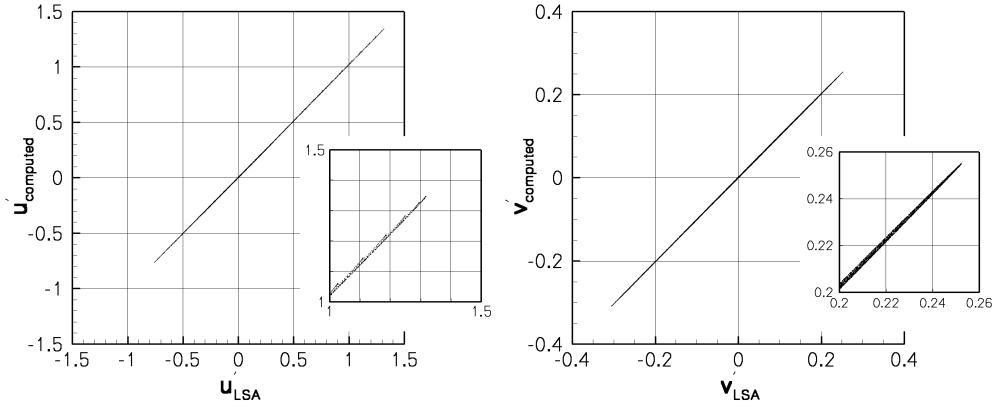

Figure 3.9: Scatter plots for u' (left) and v' for Shear Layer B, $\Delta x = 0.0625$ and $t = 20$

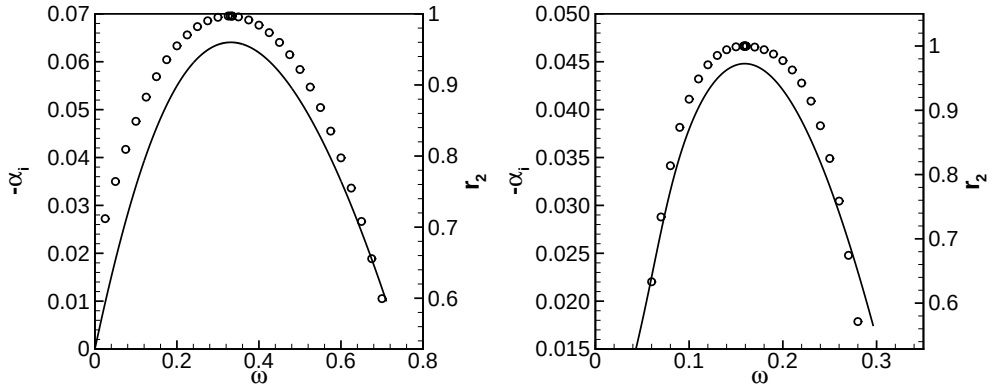

Figure 3.10: Correlation r_2 (circles) as a function of the frequency ω for Shear Layer A (left) and B at time $t = 20$. Also plotted is the dispersion relation (continuous line). This tests the value of ω where the maximum in r_2 occurs. The maxima of $-\alpha_{\mathrm{i}}$ and r_2 correspond to the same value ω, therefore the correlation is maximum at the forcing frequency. The forcing frequency chosen corresponds to the maximum of $-\alpha_{\mathrm{i}}$

3.3.6 Discussion

Convergence of the error norm is only possible when the growth rate converges to the one predicted from LSA. In one of the test cases considered here, Shear Layer A, the growth rate of the computed solution somewhat differs from the one predicted from LSA and, as a result, the L_∞ norm does not converge within the resolution range explored. The discrepancy in the growth rate was quantified using the developed correlation metric. Correlation metrics assume only the "shape" of the solution and not the growth rate. The present results show that this assumption is valid since the maximum of the correlation was always very close to unity.

While correlation metrics differ from classical error metrics and cannot be used as the only test in the verification of a fluid-dynamics solver. They complement to classical error assessment tools in a numerical-simulation verification program. A limitation of the correlation metric, as is implemented here, is that the magnitude of the solution is not assessed because of the normalization of the correlation coefficient (Eq. 3.21). Thus, at least an additional test is required.

While simple flows can be used to verify order-of-accuracy and convergence, the present technique utilizes results from LSA that provides solutions to the linearized partial differential equations of fluid flow so that a solver can be tested on a more complex problem with realistic boundary conditions. As is evident from the example of the spatial shear layer used in this study, boundary conditions are of particular significance. Perturbations are introduced at the inflow, convect downstream, and must exit at the outflow boundary without excessively contaminating the flow with spurious reflections. Failure to impose the correct inflow condition or the presence of spurious reflected waves at outflow boundaries will cause a reduction in the correlation and a deviation of the growth rate

from LSA predictions. For this reason, while the methodology described here assesses the solver, it is particularly valuable in that it also assesses the particular boundary closure.

Furthermore, the current method does not require modification of the solver—as does the method of manufactured solutions, where additional/separate treatment for source terms is required—and can be used for the assessment of "black-box" solvers where the user has no access to the source code.

Although in the example of the instability of a spatially developing laminar shear layer presented here, a normal-mode methodology is used to derive the stability characteristics of the basic flow, the current methodology is not restricted to normal linearized operators. If the linearized equations about a basic flow exhibit non-normal behavior and therefore transient growth (Han et al., 2000), a modified technique from that presented here may be required. The main idea is to compare a solution of the linearized equations to a solution from a non-linear solver using a projection-based method. In many cases, the linearized problem reduces to the solution of an ordinary differential equation for which solution methods are well developed and can be readily verified. This feature of the use of LSA solutions makes them attractive for verification of non-linear multi-dimensional partial differential equations solvers.

The proposed method can be extended to three dimensions and other flows for which LSA can be applied. Extending the example discussed here, one could consider oblique wave disturbances, for example, of the form,

$$Q'(x, y, z, t) = f(y) \exp[i(\alpha x + \beta z - \omega t)]. \tag{3.35}$$

In this case, the parameter space of the correlation would be expanded to include the values of the spanwise component.

Chapter 4

Simulations

Two sets of simulations were conducted to study the dependence of flow characteristics on inflow conditions and grid resolution. In the first group, the flow conditions remain unchanged while the grid is refined, whereas in the second group, the effect of variable mass injection is considered for two different mass-injection ratios at a fixed top-stream velocity. In all cases simulated, the flow is compressible but subsonic with top-stream Mach numbers of 0.35 or 0.5.

The two streams are assumed to be of the same gas with constant specific heats ratio, $\gamma = 1.4$. The dynamic viscosity, μ, is assumed to be constant (independent of temperature), the Prandtl and Schmidt numbers are also constant and equal to the corresponding molecular diffusivity values of $Pr = 0.7$ and $Sc = 1$, respectively. The approximation of the transport coefficients as constant is adequate given the low Mach number of the flows simulated and the matched free-stream density and temperature of the two streams.

The computational domain has dimensions $L_x \times L_y \times L_z$, in the streamwise, transverse, and spanwise directions, respectively, with uniform grid spacing in all dimensions. The top stream inflow boundary is at distance L_i upstream of the end of the splitter plate, as shown in Fig. 4.1. In all the simulations, $L_z = L_y = 2h$. In the spanwise direction, the flow is assumed to be statistically homogeneous and periodic boundary conditions are used. For reference, the spanwise extent of

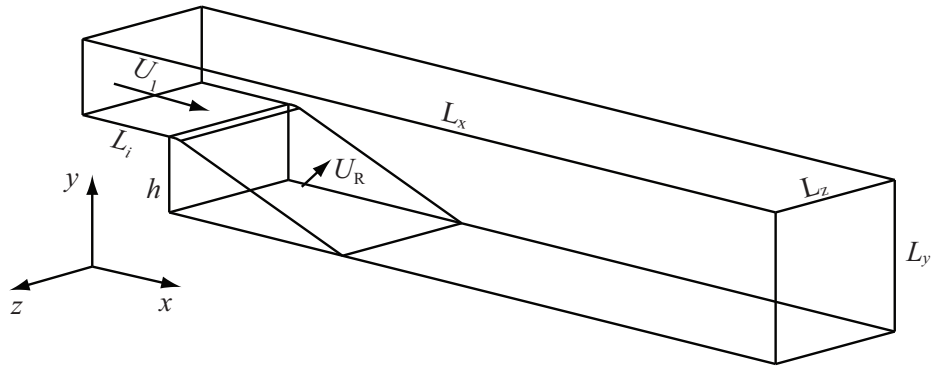

Figure 4.1: Computational domain configuration

the test section in the experiments is $3h$. All lengths reported are normalized by the step height $h = 0.05$ m.

It is useful to define a global Reynolds number for the flow. The Reynolds number is based on the velocity difference between the top free stream, U_1, and the velocity magnitude on the ramp, U_R, $\Delta U = U_1 - U_\mathrm{R}$. The step height, h, is used as the reference length scale,

$$Re \equiv \frac{\Delta U\ h}{\nu}. \tag{4.1}$$

The velocity U_R is obtained from the mass flux of the lower stream after dividing by the density and the area of the ramp, in accord with the definition of U_R in the experiments. In a similar manner, the convective velocity is defined as

$$U_\mathrm{c} \equiv \frac{U_1 + U_\mathrm{R}}{2}. \tag{4.2}$$

Table 4.1 summarizes the conditions for the different cases simulated.

Case	C1	C2	C3	D2	E2
M_1	0.35	0.35	0.35	0.5	0.5
U_1 [m/s]	120	120	120	170	170
$\dot{m}_2/\dot{m}_1$	0.09	0.09	0.09	0.11	0.23
Re	3.8×10^5	3.8×10^5	3.8×10^5	5.5×10^5	4.8×10^5
$\Delta x/h$	1/20	1/40	1/80	1/40	1/40
L_x/h	22	22	22	25	25
L_y/h	2	2	2	2	2
L_z/h	2	2	2	2	2
L_i/h	2	2	2	1	1
Number of cells	0.7×10^6	5.4×10^6	43.1×10^6	6.3×10^6	6.3×10^6

Table 4.1: Conditions for the cases simulated

4.1 Initial condition

The flow is initialized with a hyperbolic-tangent velocity profile

$$u(y)/U_1 = \eta(y-h) + u_\mathrm{r}(1 - \eta(y-h)), \tag{4.3}$$

where $u_\mathrm{r} = u_2/U_1$ is the velocity ratio of the two streams, with u_2 the streamwise component of U_R and,

$$\eta(y) = \frac{1}{2}(1 + \tanh(\alpha y)). \tag{4.4}$$

The parameter α is chosen such that the 99% half-thickness of the shear layer, δ, defined as

$$\frac{U_1 - u(\delta)}{U_1} = 0.01, \tag{4.5}$$

is 10% of the step height: $\delta = 0.1h$.

For the particular flow of interest here, the initial condition does not affect the final statistically stationary state since the initial field is "washed out" and subsequent realizations depend only on the boundary conditions. All flow statistics are collected after the first three "flow-through" times, defined as $t_c \equiv (L_x - L_\mathrm{i})/U_\mathrm{c}$, to allow for the flow to become uncorrelated from the initial condition. The specific initial condition was chosen because of its simplicity and the closeness to the quasi-steady state, factors that contribute to the reduction of the initial transient time.

4.2 Boundary conditions

Two central aspects of the numerical modeling employed in this study are associated with the choice of boundary conditions: the ability to integrate for long times (time stability) and the treatment of solid boundaries (walls). The resolution of the turbulent boundary layers that develop on the lower and upper guide walls poses a severe computational challenge for the computational framework used. The Reynolds number based on the distance from the inlet for locations near the downstream boundary is of the order of a few million. Even though in the context of the SGS modeling methodology the resolution requirements can be significantly reduced compared to direct simulation (e.g., Pantano et al., 2008); there is an additional modeling challenge that arises from the unsteady three-dimensional character of the flow near the reattachment of the shear layer. So far, very few LES results for three-dimensional turbulent boundary layers (3DTBL) have appeared in the literature, the work of Kannepalli & Piomelli (2000) is one example.

Due to the aforementioned difficulties introduced by the no-slip condition on the solid boundaries, the lower and upper guide walls and the splitter plate are assumed to be stress-free, adiabatic boundaries, enforcing only the no-penetration condition,

$$v = 0, \qquad \frac{\partial u}{\partial y} = \frac{\partial w}{\partial y} = 0, \tag{4.6}$$

and,

$$\frac{\partial E}{\partial y} = 0. \tag{4.7}$$

Although at the high Reynolds numbers of interest, the boundary layer thickness remains small compared to the duct height and does not directly affect the mixing in this respect, the likely separation of the flow on the upper guide wall in the adverse pressure gradient region downstream of the reattachment can have a significant effect on the large-scale flow, potentially altering the mixing. This is the most significant of the modeling assumptions of the simulations. Its impact on the prediction of the flow and mixing performance in the geometry will be assessed in the analysis of the results.

The top stream inflow velocity profile is of the form of a mean field that is only a function of the transverse coordinate, plus a perturbation,

$$\mathbf{u}(t,x,y,z) = \bar{\mathbf{U}}(y) + \mathbf{u}'(t,x,y,z). \tag{4.8}$$

The mean velocity profile, $\bar{\mathbf{U}}(y)$, has the hyperbolic-tangent form of Eq. 4.3 for $y > h$. The perturbation is of the form[1]

$$\mathbf{u}'(t,x,y,z) = f(y)\exp[i(U_1 t k_x + (y-h)k_y + z k_z)], \tag{4.9}$$

with

$$f(y) = \mathcal{A}\ \exp(-\beta(y-h)^2)\ \tanh(2\alpha(y-h)). \tag{4.10}$$

The parameters $\mathcal{A}$ and β are chosen such that the magnitude of the perturbation is 5% of the free-stream velocity U_1 and its thickness is the same as the thickness of the hyperbolic-tangent profile of Eq. 4.3. In practice the additional constraints

$$\nabla \cdot \mathbf{u}' = 0, \tag{4.11}$$

$$v' = w', \tag{4.12}$$

and

$$k_x = k_y = k_z \tag{4.13}$$

are imposed, with

$$k_x = 2\frac{2\pi}{h}. \tag{4.14}$$

Since the shear layer is convectively unstable, inflow forcing contributes to a faster development of the instability and provides a surrogate model of the turbulent boundary layer that forms on the top of the splitter plane in the experiments. The wavenumber used in the forcing was chosen from several values tried in simulations of flows over backward-facing steps and with ramp injection with the criterion of the fastest resulting growth of the instability.

The density and static pressure at the inflow are uniform.

The top stream has a mixture fraction value of $Z = 1$ and the lower stream, $Z = 0$.

At the outflow, the condition of constant pressure at infinity of Poinsot & Lele (1992) is imposed. The "pressure at infinity" is set to be the atmospheric pressure since, in the experiments the test section discharges to atmospheric conditions.

The flow through the ramp is assumed to be uniform, because the geometry of the perforation

[1] The form of the inflow perturbation and the divergence-free condition of $\mathbf{u}'$ was suggested by C. Pantano.

cannot be resolved by the computational grid, with the mass flux matched to the measured value. The assumption of uniform inflow causes a discrepancy in the momentum flux through the ramp compared to the experiment. Moreover, the jets that emerge from the perforations may have an effect on the development of the instability characteristics on both the primary and secondary shear layers that cannot be reproduced in the simulations.

4.3 Results at $U_1 = 120$ m/s—Grid refinement study

4.3.1 Flow characteristics

The instantaneous passive scalar fields in Figs. 4.2 and 4.3 show spanwise-organized structures, similar to the ones observed in free shear layers and the experiments of Johnson (2005) and Bergthorson et al. (2008). The primary shear layer appears more two-dimensional than the secondary because of the unsteady three-dimensional character of the flow in the recirculation region. The unsteady, complex nature of the flow is also illustrated in Fig. 4.4 where contours of the streamwise velocity corresponding to the scalar field of Fig. 4.3 are plotted. The recirculation "bubble" is comprised of several pockets of upstream-moving fluid, same of them not extending through the whole span. From the contour plots of instantaneous velocity and scalar fields, it appears that the large structures of the primary shear layer have a large effect on the flow in the recirculation region.

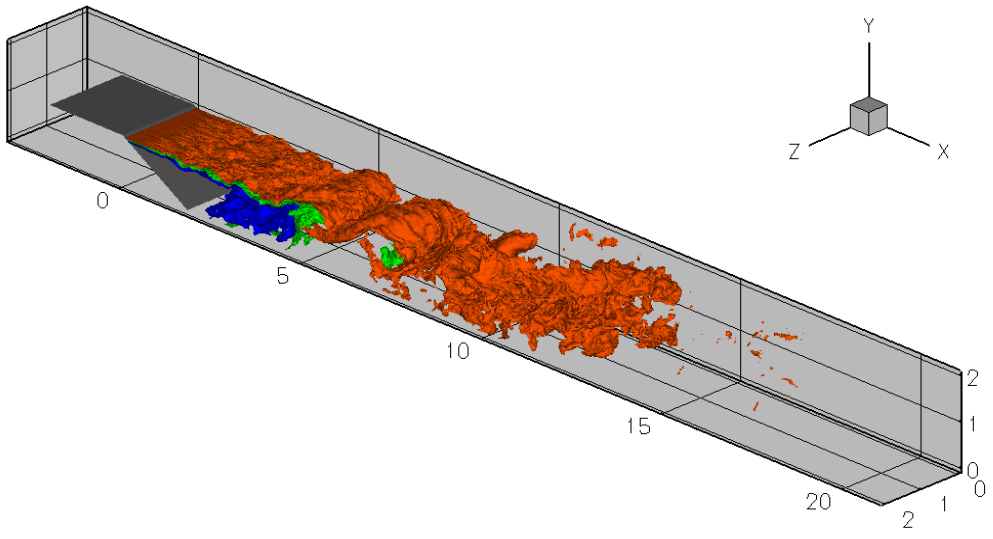

Figure 4.2: Instantaneous scalar iso-surfaces for Case C2. Iso-surfaces correspond to $Z = 0.8$ (red), $Z = 0.5$ (green), and $Z = 0.2$ (blue). Notice the large spanwise-organized structures in the primary shear layer.

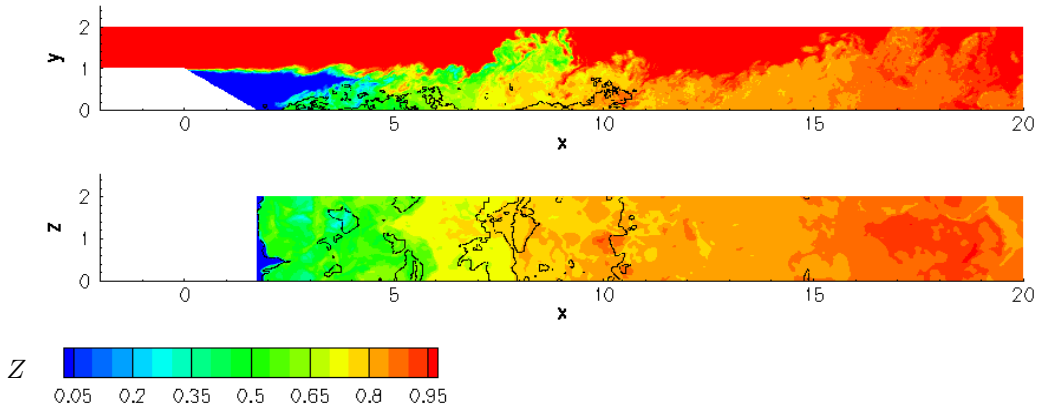

Figure 4.3: Instantaneous scalar contours on the mid span plane (top) and bottom wall for Case C3. Black contour corresponds to the value of zero streamwise velocity. The flow is moving upstream in regions between the black contour and the lower wall or when surrounded by the black contour. The corresponding u-velocity field is shown in Fig. 4.4.

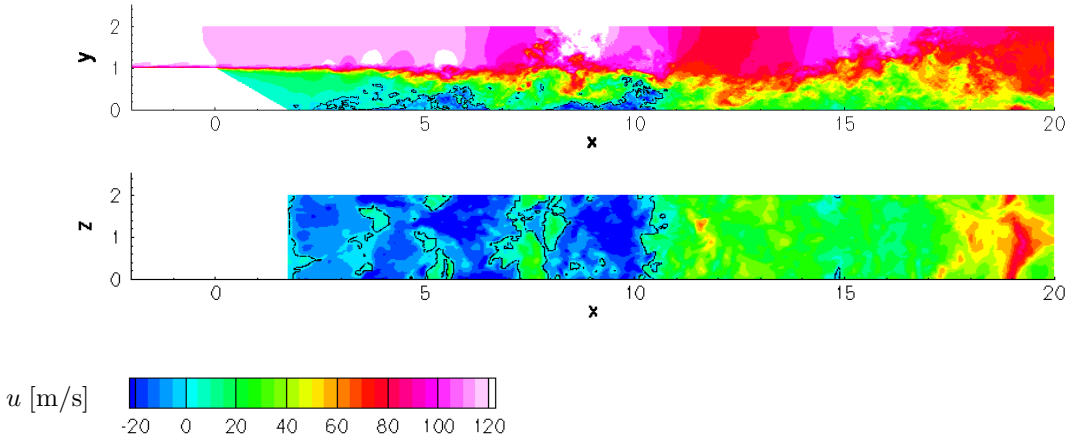

Figure 4.4: Instantaneous scalar contours on the mid span plane (top) and bottom wall for Case C3 at the same time as the scalar field of Fig. 4.3. Black contour corresponds to the value of zero streamwise velocity.

4.3.2 Mean fields

Before averages of the time-dependent fields are considered, the assumption of quasi-steady state is assessed. Failure to implement a well-posed boundary closure can result in the drift of mean quantities in the computational domain (Poinsot & Lele, 1992), in which case, statistics cannot be accumulated over time. For all the simulations performed the average pressure and u-velocity on planes normal to the streamwise direction near the inflow of the top stream and the outflow were recorded as a function of time. In this manner, the boundary closure is verified for a turbulent flow and the effect of the injection of the lower stream through the ghost fluid on the well-posedness of the boundary conditions is evaluated.

Figure 4.5 shows plane-averaged pressure at the inflow and outflow as a function of time. The pressure trace at the outflow fluctuates as a result of the large scale structures crossing the plane where the average is computed. As the structures exit the domain, they generate disturbances that travel upstream and exit through the inflow boundary. The upstream-traveling pressure waves are recorded in Fig. 4.5 as the fluctuations of the pressure trace at the inflow. Similar behavior for free shear layers has been observed experimentally (Dimotakis & Brown, 1976; Hall, 1991) and is one of the factors that contribute to the generation of the instability.

In order to remove the fluctuating part of the pressure traces, a rolling average is employed with a period of three convective times ($T_{\text{roll. ave.}} = 3t_c$). The flow configuration, for the values of relatively small injection velocities studied, acts as a diffuser. The velocity profile at the outflow becomes more uniform compared to the inflow and the static pressure increases, as can be seen from the rolling averages of pressure in Fig. 4.5. The average outflow pressure remains constant with time at a value modestly larger than 10^5 Pa, which is the value of the "pressure at infinity," as specified in the implementation of the characteristic boundary condition. Inflow pressure also remains almost constant with a small increase in later times. This can be attributed to the variation of the recirculation zone length[2] in the duration of the run. For all cases simulated, no indication of drifting of the mean fields was observed in the time length of the integration.

Mean fields are two-dimensional (on $x-y$ plane) and for an arbitrary scalar field f are computed as (Veynante & Knikker, 2006)

$$\{f\} = \frac{\langle \rho f \rangle}{\langle \rho \rangle}, \tag{4.15}$$

where $\{f\}$ is an approximation of the density-weighted variable f. The angle brackets denote ensemble average in span and time, the two statistically homogeneous dimensions of the flow. The curly braces will be omitted for clarity.

Mean u-velocity profiles for Case C2 are shown in Fig. 4.6 for different streamwise locations. Near the lower wall, in the recirculation region, the velocity is about 10–15% of the top free stream.

[2] A shorter recirculation zone will lead to a larger pressure recovery resulting in a lower pressure at the inflow given the constant (atmospheric) pressure of the outflow.

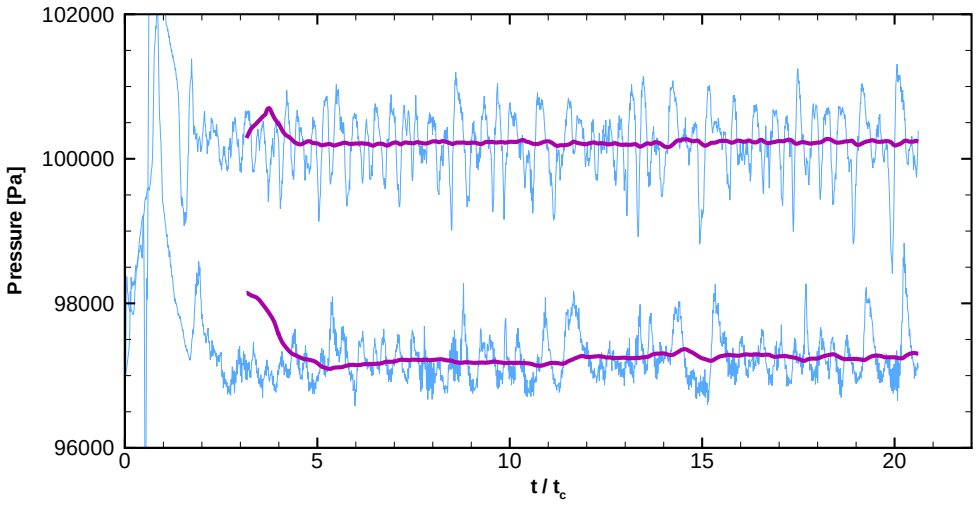

Figure 4.5: Plane-averaged inflow and outflow pressure as a function of time for Case C2. Thin lines denote pressure averaged over planes normal to the streamwise direction near the inflow and outflow. Outflow pressure is always higher than the inflow. Thick lines are a rolling average of the pressure traces, with an averaging period of 3 t_c.

The mean reattachment point is at about 10 step heights.

The improved mixing characteristics of the current configuration compared to free shear layers are illustrated in Fig. 4.7, showing the mean scalar field and streamlines. Mixed fluid is convected upstream near the lower wall where it mixes in the secondary shear layer with the lower stream as observed in the experiments and documented by Johnson (2005), Bergthorson et al. (2008), and Bonanos et al. (2008b). As a result, the pure lower-stream fluid is consumed by $x = 4$, something that cannot be achieved by a free shear layer with the same free stream conditions.

4.3.3 Effect of grid resolution on mean fields and the passive scalar probability density functions

The turbulence modeling methodology employed in this study explicitly models all residual motions. An ideal SGS model should produce solutions that are grid-independent when a sufficient range of scales is resolved. Also, the SGS terms are expected to vanish as the grid is refined to resolve all flow scales. The first requirement is, in practice, hard to achieve because numerical errors from the spatial derivatives discretization interact with modeling errors (Ghosal, 1996).

In one of the few studies to analyze the dependence of LES predictions on resolution, Meyers et al. (2003) constructed a database of decaying isotropic turbulence LES and DNS predictions and examined the modeling and numerical errors for different simulation parameters using a Smagorinsky subgrid model (Smagorinsky, 1963). Although their results are specific to the variant of the Smagorinsky subgrid model they used, they found that modeling and discretization errors may

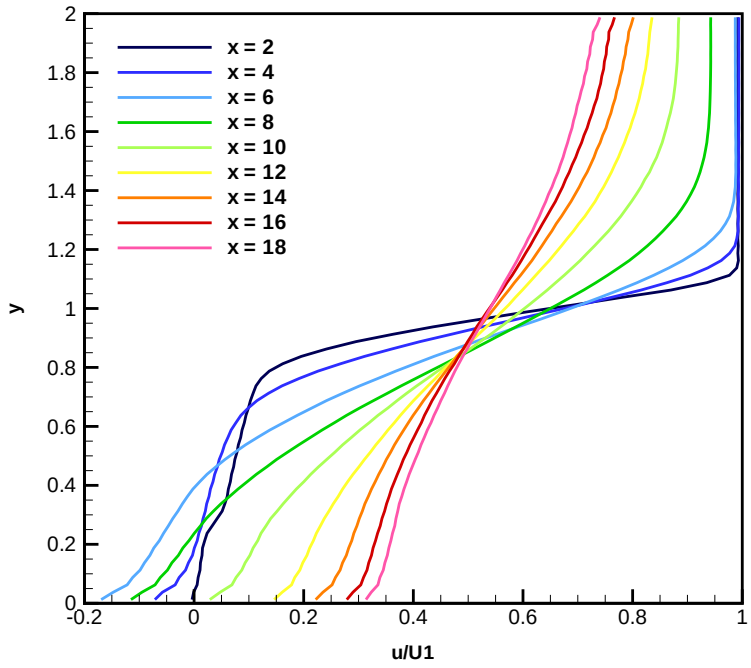

Figure 4.6: Change of the mean streamwise velocity profile for Case C2 with respect to the streamwise coordinate

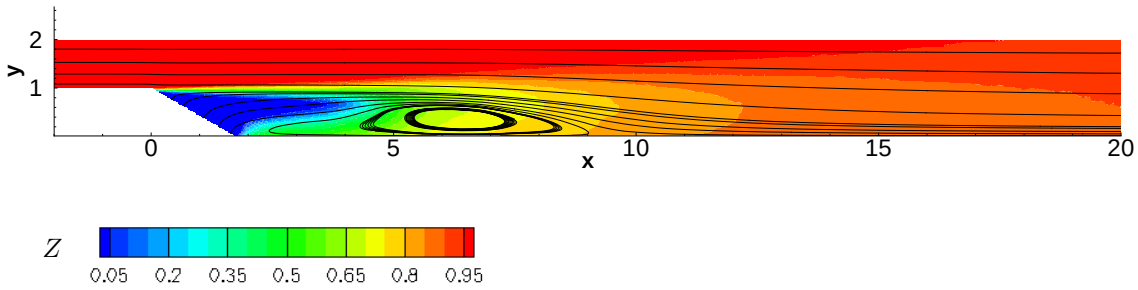

Figure 4.7: Contours of mean passive scalar and mean streamlines for Case C2

partially cancel each other and formulated an optimal refinement strategy, which depends on the Reynolds number. In an earlier grid-refinement study of LES of temporal mixing layers, Vreman et al. (1996) reported a similar cancelation of modeling and discretization error.

In the results reported here, the effect of the grid spacing on the prediction of the mean fields and the probability density functions of the scalar is considered. An analysis similar to Meyers et al. (2003) cannot be carried out since direct simulation is not feasible for the Reynolds number of Cases C1–3. Nevertheless, the current refinement study is significant as it attempts to answer two main questions: (a) are the predictions grid-independent, and (b) if there is grid dependence, do statistics tend to converge as the grid is refined?

It is expected that at coarser resolutions, where a significant fraction of the turbulent kinetic

energy is not resolved, the modeling error is going to be larger. As the grid is refined, in a self-consistent LES–SGS scheme, the modeling error should become smaller. However, it may not continue to decrease, or even monotonically with increasing resolution. Table 4.2 shows a comparison of the cell size with the Kolmogorov, λ_{K}, and Liepmann–Taylor, λ_{T}, (Dimotakis, 2000) scales for the three cases of the refinement study. The Liepmann–Taylor scale is an estimate for the thickness of the internal laminar layers of the shear layer. The Kolmogorov and Liepmann–Taylor scales are estimated from the Reynolds number of the flow as defined in Eq. 4.1,

$$\lambda_{\mathrm{K}} = h\, Re^{-3/4}, \tag{4.16}$$

and

$$\lambda_{\mathrm{T}} = 5.0\, h\, Re^{-1/2}. \tag{4.17}$$

The coarsest simulation has cells that are almost 800 times larger than the smallest flow scales, while the grid cells at the finest resolution are 200 times larger than the smallest flow scales. In the highest resolution run, the Liepmann–Taylor scale is of the order of the cell size. For all simulations, the SGS cut-off length is taken equal to the grid spacing.

Case	C1	C2	C3
Re	3.8×10^5	3.8×10^5	3.8×10^5
Number of cells	0.7×10^6	5.4×10^6	43.1×10^6
$\Delta x/h$	1/20	1/40	1/80
$\Delta x/\lambda_{\mathrm{K}}$	770	385	192
$\Delta x/\lambda_{\mathrm{T}}$	6.2	3.1	1.5

Table 4.2: Ratio of grid spacing to the Kolmogorov, λ_{K}, and Liepmann-Taylor scale, λ_{T}

The computed mean quantities for Cases C1–3 show differences between the three cases, with Case C1, the coarsest grid, exhibiting the largest variation between them, while Cases C2 and C3 appear to agree well. As expected, the grid C1 is too coarse to accurately capture the flow, a fact that is illustrated by the mean length of the recirculation region shown in Fig. 4.8. The mean reattachment point is 14 step heights downstream of the splitter plate in Case C1, whereas in Cases C2 and C3 it is at $x = 9$ and $x = 8.5$, respectively. The differences in the mean flow fields result in different scalar fields (Fig. 4.8).

Figure 4.9 provides a more detailed picture of the flow and supports the observation that mean profiles converge as the grid is refined, with Cases C2 and C3 being in good agreement with each other. An interesting observation is that dependence on grid spacing of the profiles is not the same for all quantities. The streamwise velocity, u, is less sensitive than the passive scalar, Z, for example. As a consequence, agreement in u does not necessarily imply agreement in the mean scalar, as can be seen for Cases C2 and C3 in Fig. 4.9.

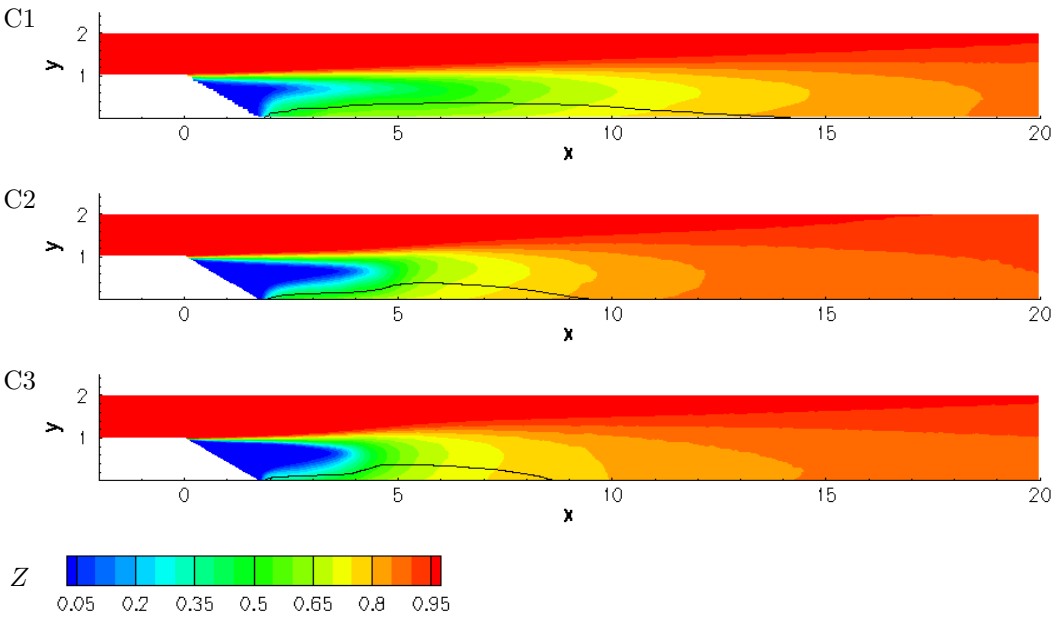

Figure 4.8: Mean scalar fields for Cases C1–3. Black contour corresponds to the value of zero streamwise velocity. The flow is moving upstream in regions between the black contour and the lower wall. Case C1, the lowest resolution simulation, predicts a longer mean recirculation zone.

Also shown in Fig. 4.9 is the pressure coefficient, a non-dimensional measure of the pressure and an important operation parameter for the combustor (Bergthorson et al., 2008). The pressure coefficient is computed as

$$C_p(x,y) = \frac{p(x,y) - p_1}{\frac{1}{2}\rho_1 U_1^2}, \tag{4.18}$$

where p_1 and ρ_1 are the top stream inlet pressure and density, respectively. The different lengths and shapes of the recirculation region affect pressure recovery and, as a result, the C_p profiles of Fig. 4.9 shift horizontally in addition to the change in shape.

Turbulent kinetic energy, TKE $= \frac{1}{2}(u'^2 + v'^2 + w'^2)$, profiles are shown in Fig. 4.10. At $x = 4$ the flow is essentially a free shear layer of small thickness relative to the grid spacing. The total (subgrid plus resolved) TKE profile of the highest resolution case at $x = 4$ differs significantly from the two other cases, a fact which suggests that the primary shear layer is not sufficiently resolved by grids C1 and C2. At the other two streamwise locations, TKE profiles can be seen to converge towards the profile of Case C3. The ratio of the subgrid TKE, as estimated by the stretched vortex SGS model, to the total TKE is also shown in Fig. 4.10.

The study of the profiles of Figs. 4.9 and 4.10 indicates that Case C1 is under resolved, even in an LES sense, whereas Cases C2 and C3 appear to capture the flow more accurately. This conclusion is also supported by the comparison to the experimental data discussed in Section 4.3.6.

Accepting the results of Case C2 as sufficiently accurate, a criterion can be formulated for a

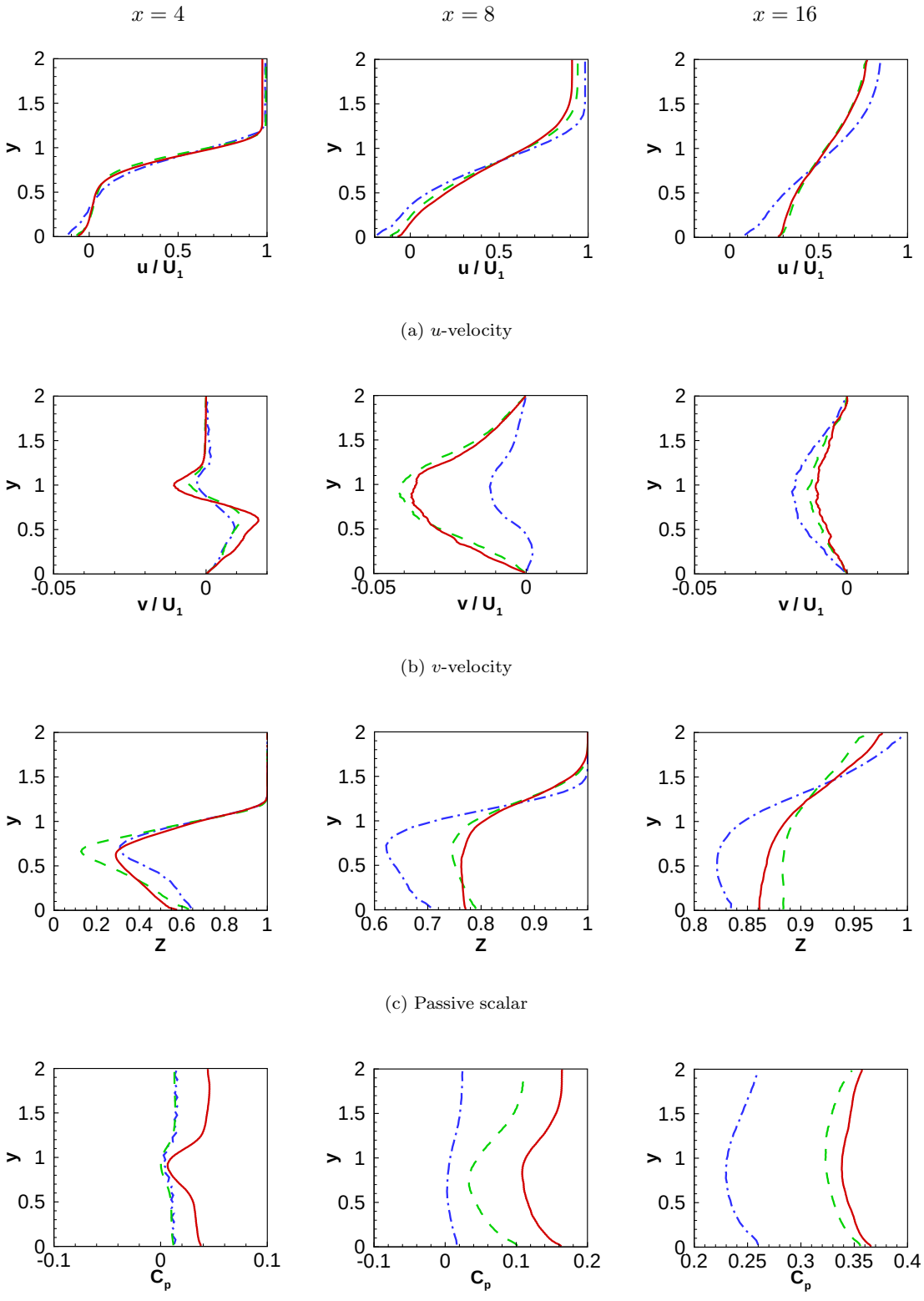

(a) u-velocity

(b) v-velocity

(c) Passive scalar

(d) Pressure coefficient

Figure 4.9: Mean profiles for Cases C1–3 at different streamwise locations, from left to right x=4, 8, and 16. Blue dash-dot lines correspond to Case C1, lowest resolution; green dashed lines to Case C2, medium resolution; red solid lines to Case C3, highest resolution.

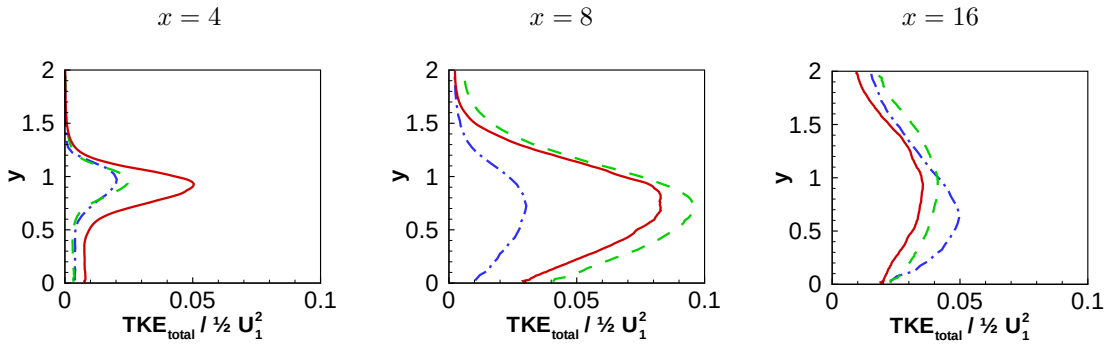

(a) Turbulent kinetic energy

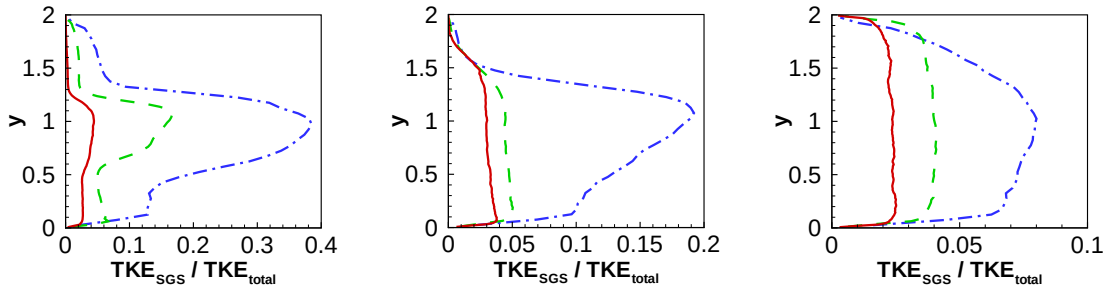

(b) Turbulent kinetic energy ratio, total to sub-grid

Figure 4.10: Turbulent kinetic energy (subgrid plus resolved) and ratio of turbulent kinetic energy to subgrid turbulent kinetic energy for Cases C1–3 at different streamwise locations, from left to right x=4, 8, and 16. Blue dashed-dot lines correspond to Case C1, lowest resolution; green dashed lines to Case C2, medium resolution; red solid lines to Case C3, highest resolution.

resolution requirement of the current LES. One must also keep in mind that the computational cost of the simulation changes by a factor of 16 when the grid resolution is doubled in each direction. Using the information in Fig. 4.10, it can be inferred that a sufficiently resolved simulation requires a ratio of subgrid-to-total TKE of less than 20%. Because of the underling modeling assumptions in LES, it is expected that prerequisite for the use of this criterion is the resolution of all flow features that are directly generated by the boundary conditions of the problem.

4.3.4 Passive scalar excursions

The linearity of the passive scalar equation in combination with the Laplace operator on the right hand side, sets bounds on the admissible values of the scalar. The filtered scalar equation (Eq. 2.6) must ideally observe the boundedness of the scalar field, $0 \leq Z \leq 1$, as does the exact scalar transport equation (e.g., Dimotakis & Miller, 1990). However, the approximation of the additional term of the scalar subgrid flux can produce values outside the interval $[0, 1]$. This is the case for all the present simulations. While the observed scalar out-of-bounds excursions occupy a small fraction

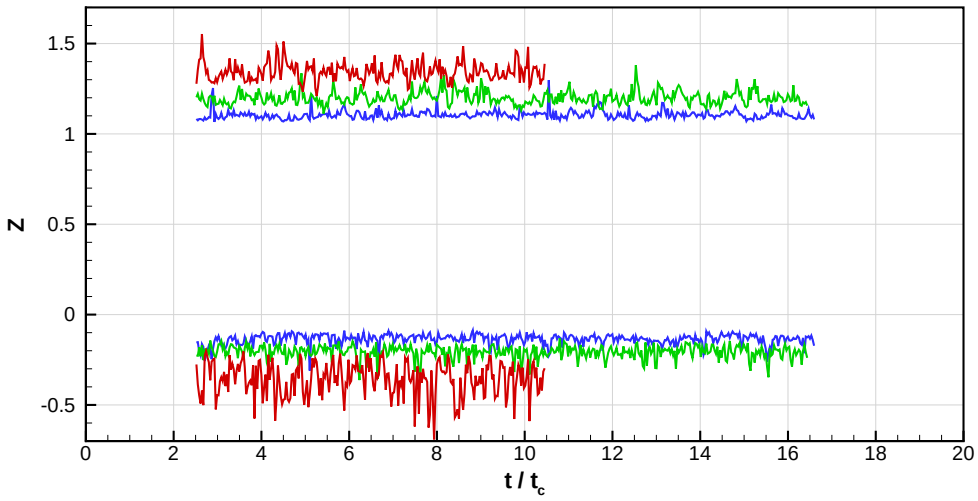

Figure 4.11: Minimum and maximum values of the passive scalar as a function of time for three different resolutions. Blue lines correspond to Case C1, lowest resolution; green to Case C2, medium resolution; red to Case C3, highest resolution.

of the volume, they are unphysical and the result of modeling error since they are produced by the approximation to the subgrid flux.

Results for Cases C1–3 show that the minimum and maximum of Z depend on resolution, as shown in Fig. 4.11. The absolute value of the excursions is found to increase as the grid is refined in the resolution range considered, with the finer run exhibiting peak excursions reaching 50%.

A measure of the error that is more useful than the local peak out-of-bounds excursions is the volume occupied by the under/overshoots. This is shown in Figs. 4.12 and 4.13 for three different thresholds at 1%, 2%, and 5% under/overshoot. The volume fraction occupied by $> 1\%$ excursions (sum of undershoot and overshoot volume fraction) is about 3%. If the tolerance is increased to $> 5\%$, the error as a volume fraction becomes negligible. However, the error reported in Figs. 4.12 and 4.13 is actually a lower bound of the error because it only accounts for excursions that fall outside the range of $[0, 1]$. Although the volume where unphysical values are encountered is small, the presence of the out-of-bounds scalar excursions is a source of contamination of the mixing statistics. For example, creation of fluid with $Z = 1.1$ corresponds an excess amount of top-stream fluid. Fortunately, in the case studied here, Z is a passive scalar and the uniform specific-heat ratio and uniform molar heat capacity of the flow do not couple such out-of-bounds scalar excursions to the flow momentum and energy.

Similar to the case of the minimum and maximum values of Z shown in Fig. 4.11, the out-of-bounds scalar error does not decrease with increasing resolution. While higher resolution might lead one to anticipate a reduction in out-of-bound scalar errors, higher resolution also increases values of the peak local scalar gradients that drive the subgrid-scale terms, amplifying the difficulty.

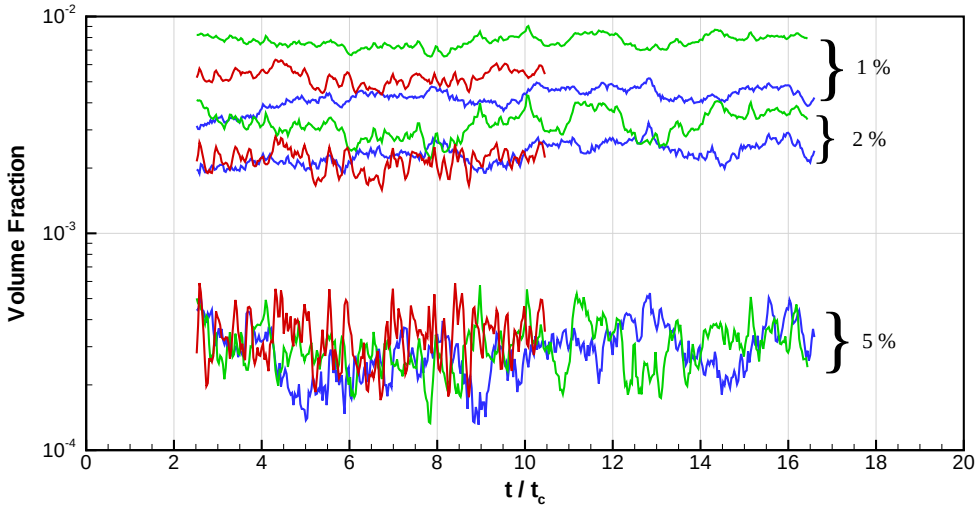

Figure 4.12: Volume fraction of the undershoots of the passive scalar as a function of time for three different thresholds and resolutions. Blue lines correspond to Case C1, lowest resolution; green to Case C2, medium resolution; red to Case C3, highest resolution.

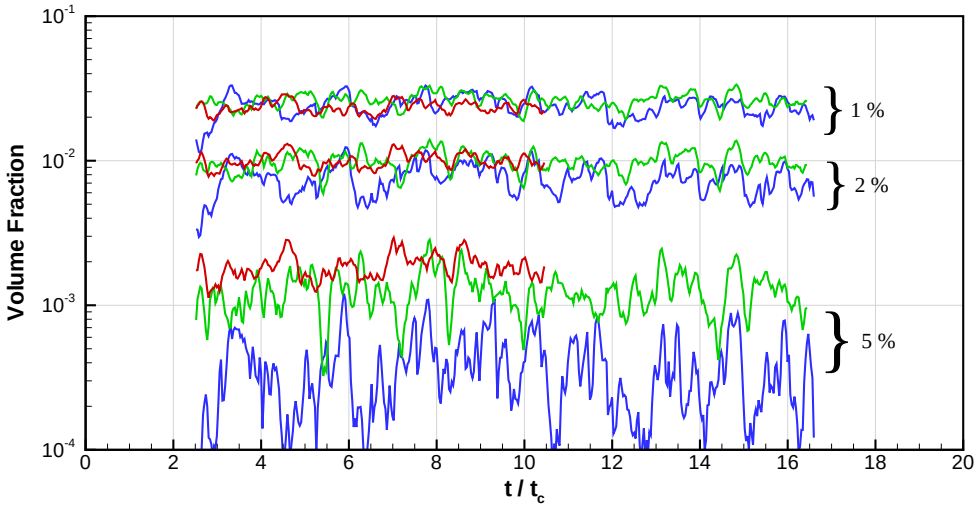

Figure 4.13: Volume fraction of the overshoots of the passive scalar as a function of time for three different thresholds and resolutions. Blue lines correspond to Case C1, lowest resolution; green to Case C2, medium resolution; red to Case C3, highest resolution.

The volume of the undershoots is smaller than the overshoots. However, this is likely a consequence of the flow configuration and not because of a peculiarity of the SGS model. The out-of-bounds excursions occur at the interfacial surface between unmixed and mixed fluid, and therefore, scale with the surface area of such encounters on the flow. As shown in Fig. 4.3, the surface area between mixed fluid and pure upper stream ($Z = 1$) is always much more than between $Z > 0$ and $Z = 0$. This is a consequence of the (intentionally) unequal mass flux of the two streams in the flow. The minimum and maximum of the excursions appear to be matched in absolute value.

Although the out-of-bounds scalar excursions corrupt the mixing statistics, it is important to appreciate the difficulty of the problem in combination with the numerical modeling choices. Almost all mixing occurs at scales far smaller than the grid spacing. Even in the highest resolution run, the cell size is 200 times larger than the Kolmogorov scale ($Sc = 1$ in all simulations). Moreover, the spatial discretization introduces no numerical dissipation and no explicit filtering is performed, relying on the SGS model for all fluid-dynamic dissipation and mixing, as mentioned above. The combination of these factors allows the direct assessment of the model because there is no contribution to the mixing by the numerical scheme, or by "numerical mixing," as is sometimes referred.

Statistics of out-of-bounds scalar excursions are not reported in the literature, therefore a comparison with other numerical schemes and models cannot be carried out.

The role of the numerical scheme is also important in the control of the excursions. Use of the dissipative WENO method that is available in the current computational framework results in a significant reduction of out-of-bounds excursions at the expense, however, of introducing additional dissipation. An interesting alternative, that was not explored in this work, is the use of a non-dissipative discretization with a wider bandwidth than the five-point-stencil tuned centered differences of Hill & Pullin (2004).

4.3.5 Probability density functions of the passive scalar

Probability density functions (PDFs) of the passive scalar contain the full single-point statistical information of $Z(x, y)$. The passive scalar PDF, $\mathcal{P}(Z; x, y)$, can be used to obtain expectations of quantities that depend on the mixture fraction such as the chemical product fraction and the temperature rise, or be directly used to study the characteristics of mixing.

The actual PDF cannot be constructed from the resolved field alone because the value of Z in each cell represents only the volume average and requires additional information about the subgrid PDF. In estimating the total PDF, one approach is to assume a functional form of the SGS scalar distribution and match the low-order statistics that are available from the resolved field (e.g., Williams, 1985; Peters, 2000). This is called the presumed-shape PDF approach. Another common approach is to solve a transport equation for the SGS PDF, as, for example, in Colucci et al. (1998) and Raman et al. (2006).

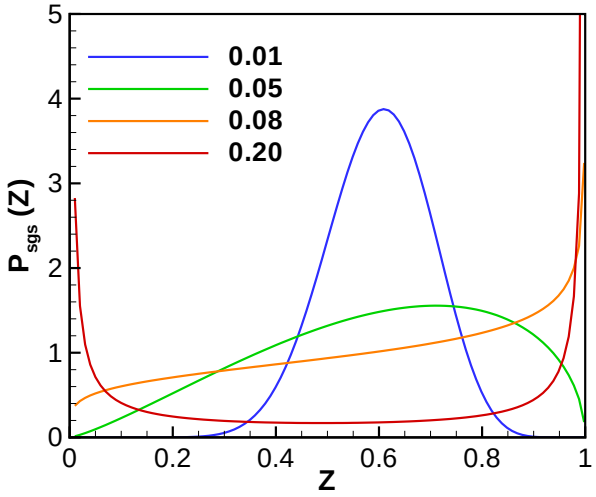

Figure 4.14: Shapes of the beta-function PDF for different values of the variance $\widetilde{Z''^2}$. All distributions have the same mean $\tilde{Z} = 0.6$.

The most widely used distribution for the SGS PDF is the beta distribution (Cook & Riley, 1994; Peters, 2000)

$$\tilde{\mathcal{P}}_{\rm sgs}(Z; x, y) = \frac{Z^{\alpha-1}(1-Z)^{\beta-1}}{\Gamma(\alpha)\Gamma(\beta)}\,\Gamma(\alpha+\beta), \tag{4.19}$$

where $\Gamma(x)$ is the gamma function. The parameters α and β can be expressed in terms of the mean $\tilde{Z}$ and the variance $\widetilde{Z''^2}$

$$\alpha = \tilde{Z}\gamma, \tag{4.20}$$

$$\beta = (1-\tilde{Z})\gamma, \tag{4.21}$$

where

$$\gamma = \frac{\tilde{Z}(1-\tilde{Z})}{\widetilde{Z''^2}} - 1 \geq 0. \tag{4.22}$$

The beta PDF is chosen to approximate the SGS PDF due to its several attractive properties. Its shape resembles PDFs measured in shear layers (Konrad, 1976; Koochesfahani & Dimotakis, 1986) and jets (Venkataramani et al., 1975; Shan & Dimotakis, 2006); the range of the independent variable is in [0,1], and is parameterized by only the first two moments. Figure 4.14 shows different shapes of the beta distribution with the same mean but different variances. For small values of the variance, the shape approaches a Gaussian, whereas when the variance is large, a singularity develops at $Z = 0$ and/or $Z = 1$, corresponding to unmixed pure fluids from each of the two inflow streams. Large variance corresponds to cases where the scalar is stirred but not well mixed in the volume of the computational cell, resulting in two peaks at $Z = 0$ and $Z = 1$, as shown in Fig. 4.14. Perhaps the most significant shortcoming of the beta PDF is the inability to describe distributions with a peak

at $Z = 0$ or $Z = 1$ and a maximum in $0 < Z < 1$. PDFs with more flexible shapes have been used at the expense of the need of additional modeling (Effelsberg & Peters, 1983; Mellado et al., 2003).

Several studies have assessed the performance of the beta PDF model for the SGS prediction of the scalar-composition distribution. Most of them are *a priori* tests (Cook & Riley, 1994; Jiménez et al., 1997; Wall et al., 2000; Mellado et al., 2003) using DNS data. In all *a priori* studies, the beta distribution was found to approximate the moments of the scalar quite well, despite the fact that the agreement in the shape of the SGS PDF was not as good (Cook & Riley, 1994; Jiménez et al., 1997). In *a priori* studies, the exact value of the SGS variance is computed from the DNS, whereas in LES it must be approximated, resulting in additional modeling assumptions. In one of a few *a posteriori* LES studies Pitsch & Steiner (2000) have shown good agreement with experimental data for a turbulent jet diffusion flame.

Several methods have been suggested for the estimation of the subgrid scalar variance in LES. Cook & Riley (1994) used a scale-similarity model, Pierce & Moin (1998) proposed a scale-equilibrium assumption and estimated the remaining coefficient using the Dynamic Procedure (Germano et al., 1991; Moin et al., 1991), whereas Jiménez et al. (2001) derived an evolution equation for the scalar variance in terms of the subgrid scalar dissipation.

The estimate of the subgrid scalar variance used in this study is consistent with the assumption that the subgrid scalar field is wound by a Lundgren stretched spiral vortex (Lundgren, 1982). Pullin & Lundgren (2001) derived the approximate solution to the equations describing the mixing of a passive scalar inside a stretched spiral vortex and obtained an expression for the scalar spectrum. The subgrid variance is computed from the scalar spectrum, $E_Z(k)$,

$$\widetilde{Z''^2} = 2 \int_{k_c}^{\infty} E_Z(k) \mathrm{d}k. \tag{4.23}$$

Similar to the case of the velocity spectrum, closure is attained by dynamic structure function matching using the second-order spherically averaged resolved-scale scalar structure function at a separation distance equal to the grid spacing (Hill et al., 2006).

The procedure of computing the total PDF follows Hill et al. (2006). The total PDF is the "actual" distribution of the scalar at a given point and is derived by correcting the resolved PDF by using an assumed PDF (the beta-PDF in this case) for the subgrid distribution. The resolved PDF is the (normalized) histogram of $\widetilde{Z}$ realizations. As with the computation of the mean quantities, the PDFs are functions of x and y, and realizations in span and time at (x, y) are used to construct $\widetilde{\mathcal{P}}(Z; x, y)$. The SGS PDF, $\widetilde{\mathcal{P}}_{\mathrm{sgs}}(Z, t, \mathbf{x})$, is formally defined as the Favre-PDF of Z (Bilger, 1975, 1977), such that for any function $f(Z)$,

$$\widetilde{f}(Z, t, \mathbf{x}) = \int f(Z)\, \widetilde{\mathcal{P}}_{\mathrm{sgs}}(Z, t, \mathbf{x})\, \mathrm{d}Z. \tag{4.24}$$

The relationship between the total and the subgrid PDF is further discussed in Gao & O'Brien (1993) and Hill et al. (2006).

In all the simulations performed, the difference between the resolved and total PDFs was found to be small. Figure 4.15 shows PDFs for Case C3 at two transverse locations at $x = 6$. As expected, the total PDFs have a lower intermediate maximum than the resolved distribution as a consequence of the finite subgrid variance. The two transverse locations in Fig. 4.15 were chosen to illustrate the difference between a point at the top edge ($y = 1.25$) and about the middle ($y = 1$) of the mixing layer. The most probable value of the scalar remains almost unchanged while the peak of the PDF decreases towards the edge of the mixing layer where it is more probable to find pure upper stream fluid ($Z = 1$) than at an intermediate composition. This behavior of the mixture fraction PDF agrees with the PDFs constructed from the measurements in free shear layers (Konrad, 1976; Koochesfahani & Dimotakis, 1986).

As discussed above, the scalar sometimes assumes values outside the interval [0,1]. Because the out-of-bounds scalar excursions do not occur uniformly randomly in the computational domain, ignoring the problematic values introduces a normalization error and bias in the statistics. Therefore, the values $Z > 1$ were placed in the largest bin, $Z > 1-\epsilon$, and $Z < 0$ in the smallest, $Z < \epsilon$, where a value of $\epsilon = 0.004$ was assumed as the width of the two boundary bins. Similar difficulties arise with the values of the variance estimated by the SGS model. The beta-function PDF is not defined for all pairs of parameters $\widetilde{Z}$ and $\widetilde{Z''^2}$ even when $0 < \widetilde{Z} < 1$. Estimated variances were occasionally too large when the mean was close to one of the boundary values. In those cases, for the construction of the subgrid PDF, the variance was reduced to the largest admissible value.

Each panel of Fig. 4.16 shows PDFs along the transverse direction for Case C2 at fixed x. In these plots, the y-axis is the transverse coordinate and should not be confused with a PDF sample-space parameter. Any curve at constant y corresponds to $\widetilde{\mathcal{P}}(Z; x, y)$ like the ones shown in Fig. 4.15.

The characteristics of the PDFs change with the streamwise coordinate. At $x = 4$, the effect of the recirculation zone results in distributions of mixed fluid near the lower wall ($y = 0$). With increasing y, there is a region where only pure lower stream fluid ($Z = 0$) is found (see Fig. 4.8), and for even larger y the PDFs show typical mixing-layer behavior.

The PDFs at $x = 8$, the location of mean reattachment, show that the mixture becomes more homogeneous near the lower wall than at the center of the duct, with the most probable value moving towards lower Z as y is increasing. This can be attributed to the fact that, as seen in Fig. 4.8, pure lower-stream fluid, although not present near the lower wall, can be found at $y = 0.5$ up to $x = 4$. Moreover, fluid near the lower wall in the recirculation zone is moving at low speeds, resulting in larger Lagrangian times that allow the mixture to become more homogeneous.

Downstream of the mean reattachment, at $x = 12$, pure upper-stream fluid occupies a very small fraction of the height while the PDFs appear more narrow with higher means. Figure 4.17 shows

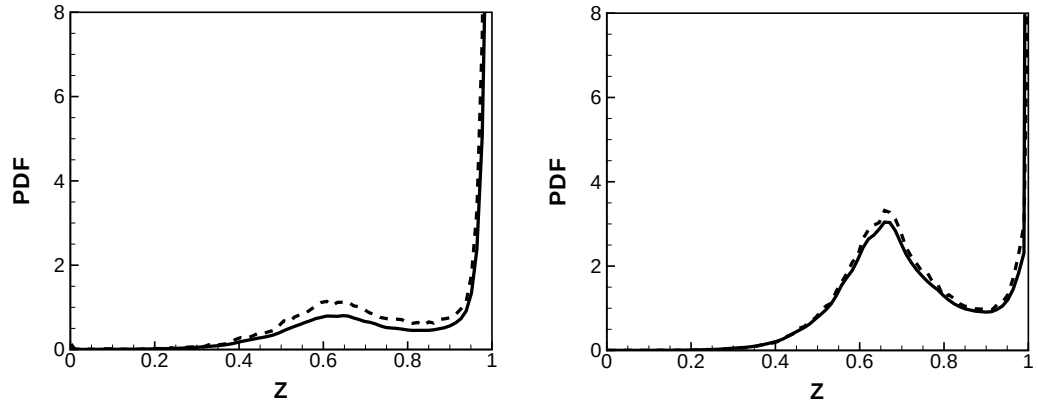

(a) $y = 1.25$ (b) $y = 1$

Figure 4.15: Probability density functions of the scalar at $x = 6$ for Case C3 at two transverse locations. Continuous lines correspond to the total PDF assuming a beta distribution for the subgrid PDF. Dashed lines denote the resolved PDF. The difference between the two is very small, implying that most of the scalar variance is predicted to be in the resolved scales.

PDFs for cases C1–3 at three streamwise locations.

The total PDFs of Fig. 4.16 are well approximated by the resolved scalar field. Accepting the modeling of the subgrid distribution, this implies that most of the scalar variance is captured by the resolved scales.

4.3.6 Comparison with experimental data

The results from Cases C1–3 are compared against the measurements reported in Johnson (2005). The lower-stream velocity in the runs C1–3 corresponds to the case $U_2 = 11$ m/s of Johnson (2005). The comparison is in terms of the pressure coefficient along the lower and upper guide walls, the temperature rise for two equivalence ratios and the probability of mixed fluid. Since there are no heat release effects in the simulations, the pressure coefficient data are compared to non-reacting experiments and the mixing (chemically reacting flow results) to the low heat release cases.

The pressure coefficient comparison is shown in Fig. 4.18. The agreement between the predicted flow and the measured is satisfactory with two main differences. The pressure coefficient in the simulation is positive throughout the computational domain whereas in the experiment the flow appears to accelerate downstream of the splitter plate before recovering pressure after the reattachment of the primary shear layer. This may occur because of the different shape or position of the primary shear layer. The second and most important difference is the length of the recirculation zone. The end of the recirculation zone is indicated in the pressure coefficient distribution by the end of the relatively flat portion of the curve and the start of pressure recovery. In the experiments, the mean

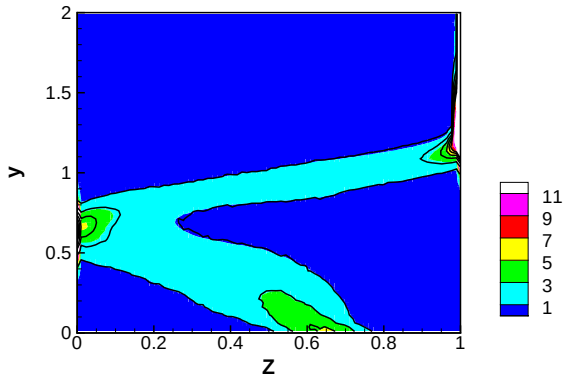

(a) $x = 4$

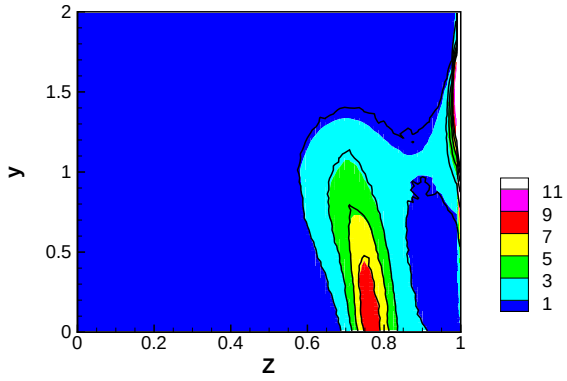

(b) $x = 8$

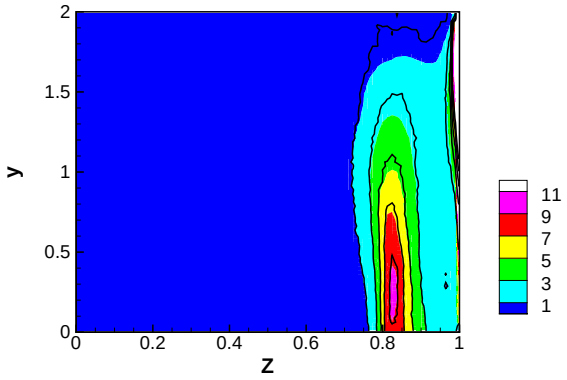

(c) $x = 12$

Figure 4.16: Probability density functions for Case C2 at different streamwise locations. Each panel shows PDFs along the transverse direction. Color contours correspond to the the total PDF whereas black contours to the resolved. Both contour sets have identical increments.

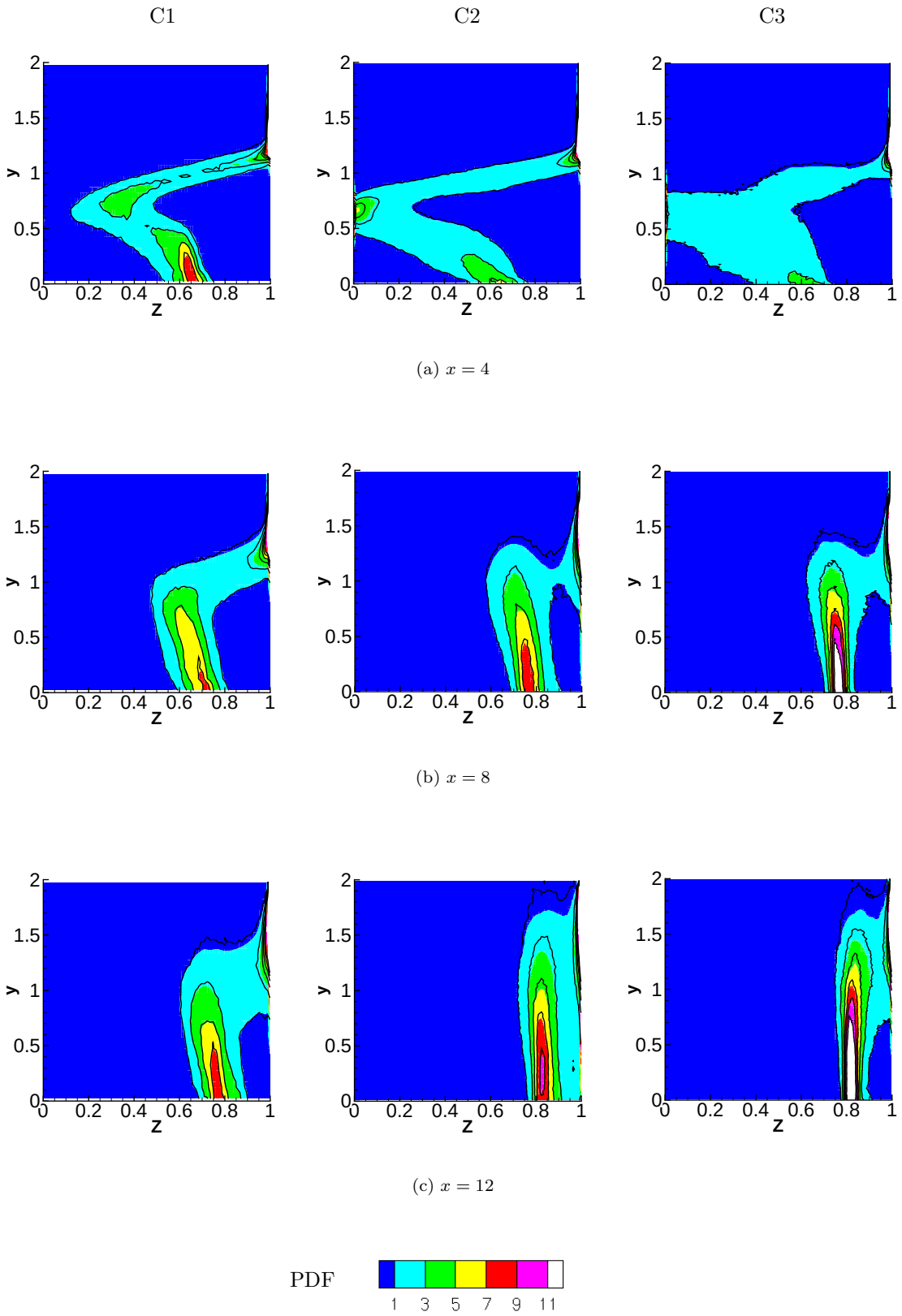

(a) $x = 4$

(b) $x = 8$

(c) $x = 12$

Figure 4.17: Scalar probability density functions for cases C1–3 at different streamwise locations. Color contours correspond to the the total PDF whereas black contours to the resolved. Contours in all panels have identical increments.

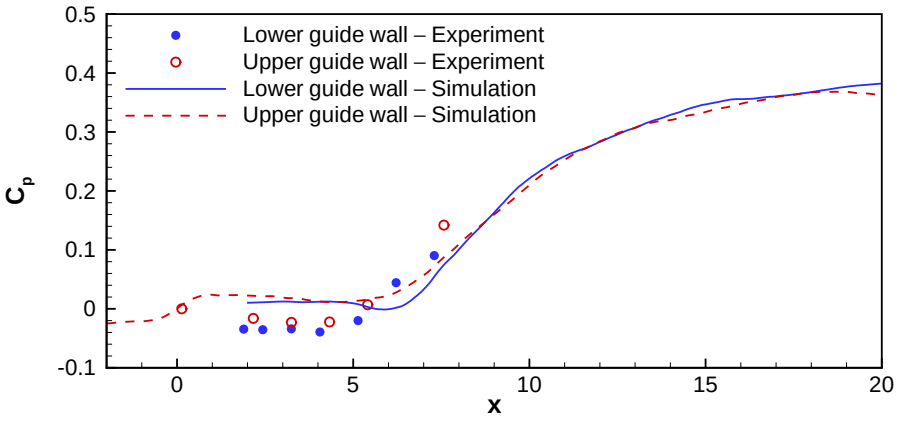

Figure 4.18: Comparison of pressure coefficient along the lower (blue) and upper (red) guide walls. Lines correspond to Case C2 of the simulations and circles to the experiments of Johnson (2005).

length is about one step height less than the simulation, a trend that was observed in all simulations. This can be explained by a mismatch in the virtual origin of the primary shear layer between the experiments and simulations. In the LES, the shear layer develops three-dimensional fluctuations at some distance downstream of the splitter plate, owing to the required length needed by the instabilities to develop. On the other hand, in the experiments, the state of the shear layer is quite different when it separates from the splitter plate. The fluctuations in the boundary layer upstream of the splitter plate, the separation of the flow at the top of the inclined ramp and the effect of the jets emanating from the perforations of the ramp contribute to a different initial condition for the shear layer. Previous studies have shown that growth rate in free shear layers is sensitive to the inflow conditions (e.g., Slessor et al., 1998). These effects are not modeled in current simulations and, as a consequence, the virtual origin and growth rate are expected to differ from the experiments. Unlike simulations of free shear layers and jets, the virtual origin is not a free parameter here because the origin of the secondary shear layer is fixed.

The probability density functions of mixture fraction are used to estimate the temperature rise. At a particular mixture fraction, the relative amount of product is given by

$$Y_{\mathrm{p}}(Z;Z_\phi) = \begin{cases} \frac{Z}{Z_\phi} & \text{for } \; 0 \le Z \le Z_\phi \\ \frac{1-Z}{1-Z_\phi} & \text{for } \; Z_\phi \le Z \le 1 \end{cases} \tag{4.25}$$

assuming complete consumption of the lean reactant. At the stoichiometric mixture fraction

$$Z_\phi = \frac{\phi}{\phi+1} \tag{4.26}$$

the reactants are completely consumed, where ϕ is the stoichiometric mixture ratio (Dimotakis,

1991).

The temperature rise normalized by the adiabatic flame temperature rise, ΔT_{f}, can be computed by (Dimotakis, 1991)

$$\frac{\Delta\widetilde{T}(y;\phi)}{\Delta T_{\mathrm{f}}} = \int_0^1 Y_{\mathrm{p}}(Z, Z_\phi)\, \widetilde{\mathcal{P}}(Z;y)\, \mathrm{d}Z. \tag{4.27}$$

Figure 4.19 shows the comparison of the normalized temperature rise for H_2-rich ($\phi = 1/8$) and F_2-rich ($\phi = 8$) conditions at $x = 7.8$.

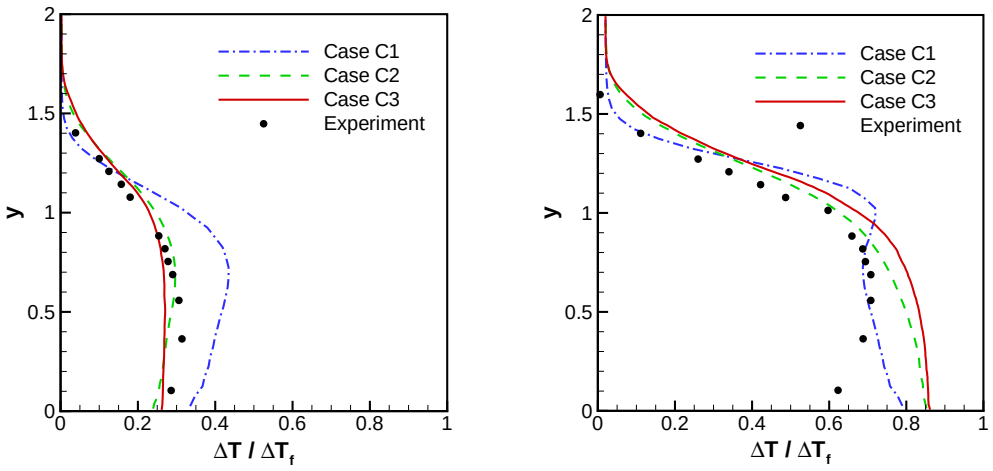

(a) $\phi = 1/8$ (b) $\phi = 8$

Figure 4.19: Comparison of normalized temperature rise for H_2 rich ($\phi = 1/8$) and F_2 rich ($\phi = 8$) at $x = 7.8$

The probability of mixed fluid is defined as the integral of the mixture fraction PDF ignoring the contribution from the edges (Koochesfahani & Dimotakis, 1986; Slessor et al., 1998),

$$P_{\mathrm{m}}(y) \equiv \int_{\epsilon}^{1-\epsilon} \mathcal{P}(Z,y)\, \mathrm{d}Z. \tag{4.28}$$

The limit of integration ϵ is

$$\epsilon \approx \frac{1}{2(1+\phi_0)}, \tag{4.29}$$

with $\phi_0 = 8$ in this case.

The probability of mixed fluid can now be computed from the constructed Z distributions from the LES. In the experiments, this is estimated from the measured temperature rise (Dimotakis, 1991;

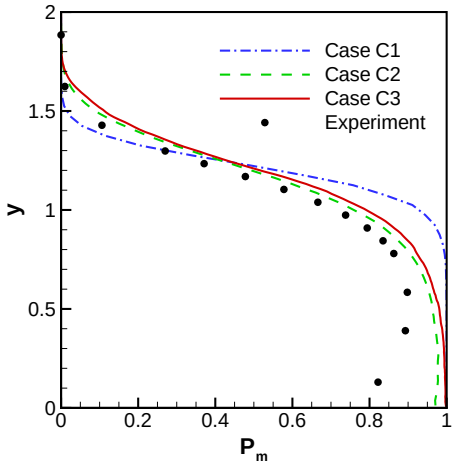

Figure 4.20: Probability of mixed fluid at $x = 7.8$

Slessor et al., 1998)

$$P_{\mathrm{m}}(y) \approx \frac{1}{1+1/\phi_0}\int_0^1 \left[Y_{\mathrm{p}}(Z;\phi=1/8)+Y_{\mathrm{p}}(Z;\phi=8)\right]\mathcal{P}(Z,y)\,\mathrm{d}Z \tag{4.30}$$

$$\approx \frac{1}{1+1/\phi_0}\left[\frac{\Delta T(y)}{\Delta T_{\mathrm{f}}}\bigg|_{\phi=1/8}+\frac{\Delta T(y)}{\Delta T_{\mathrm{f}}}\bigg|_{\phi=8}\right]. \tag{4.31}$$

The comparison of the probability of mixed fluid is shown in Fig. 4.20. The grid C1 appears to be too coarse to predict the mixing accurately. The normalized temperature rise and probability of mixed fluid comparisons show that the top boundary of the mixing region in the simulations extents higher than the experiment.

The main differences between the measured profiles of temperature rise and the ones calculated from the LES can found near the lower wall. The streamwise location where the profiles are recorded is near the mean reattachment of the primary shear layer. In this region, the flow is very unsteady and uncertainties in the measurements are larger. Measurements show that the probability of mixed fluid decreases near the lower wall, in contrast with the prediction of the simulations. In the simulations, because of the reattachment of the primary shear, mixed fluid can be found near the lower wall, therefore the probability of mixed fluid increases with decreasing distance from the lower wall. The experiments show an opposite trend: the probability of mixed fluid decreases near the lower wall. The difference in the trend of the profiles cannot be explained by the available information from the experiments.

In order to quantify the difference between the measurement and prediction and also provide a reference for future simulation efforts, the normalized L_1 distance between the experimental and

LES profiles is computed. The L_1 distance between the curves of Figs. 4.19 and 4.20 is

$$L_1^{\text{dist}} = \int_{y_1}^{y_2} |f_{\text{LES}} - f_{\text{exper}}| \, \mathrm{d}y, \tag{4.32}$$

where f is either the normalized temperature rise or the probability of mixed fluid. Because the range of the measurements does not cover the total height of the duct, the integration is performed from the lowermost location where experimental data are available, y_1, up to the measurement point closest to the top wall, y_2. The L_1 distance is normalized by the L_1 norm of the experimental profile,

$$L_1^{\text{exper}} = \int_{y_1}^{y_2} |f_{\text{exper}}| \, \mathrm{d}y. \tag{4.33}$$

For the purposes of integration the function $f_{\text{exper}}(y)$ between the data points is approximated by piecewise linear interpolation. Table 4.3 shows results for Cases C1–3.

Case	Normalized temperature rise		Probability of mixed fluid
	$\phi = 1/8$	$\phi = 8$	
C1	0.39	0.13	0.19
C2	0.12	0.18	0.10
C3	0.13	0.25	0.14

Table 4.3: Comparison of the difference between the experiments and the simulation for Cases C1–3. The values of the table correspond to the L_1 distance between the data of experiments and simulations normalized by the L_1 norm of the experimental curves.

4.4 Results at $U_1 = 170$ m/s—Effects of variable mass-injection ratio

The effect of variable mass-injection ratio is investigated in this section. Cases D2 and E2 have the same top-steam velocity, $U_1 = 170$ m/s, but different lower-stream mass fluxes. The lower-to-top mass-flux ratio in Case E2 is about double that of D2. The flow in Case D2 is similar to Cases C1–3, with a secondary shear layer forming at the base of the ramp when upstream-moving mixed fluid is further diluted by pure lower-stream fluid. The picture for Case E2 is different. The amount of injected lower-stream fluid pushes the reattachment location downstream while the amount of upstream-moving mixed fluid near the lower guide wall becomes negligible (see Fig. 4.21). The flow indicated in Fig. 4.21(b) between the spitter plate and reattachment is very similar to a free shear layer. For comparison, Fig. 4.23 shows two Schlieren visualizations from the experiments of Johnson (2005) (they are the same as Figs. 1.2 and 1.3). Although the conditions are not identical to Cases D2 and E2, the qualitative agreement of the flow between low and high injection is evident.

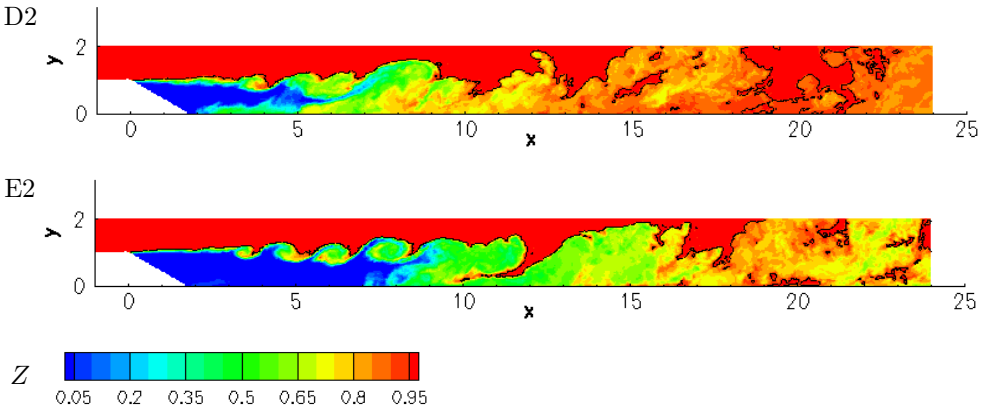

Figure 4.21: Instantaneous scalar fields for Cases D2 and E2 along mid span. Case E2, the lower panel, has about twice the mass flux ratio of lower/upper stream resulting in different characteristics of the flow in the recirculation zone. Black contour corresponds to the stoichiometric mixture fraction for a notional octane (C_8H_{18}) fuel, $Z_{\mathrm{st},\,C_8H_{18}} = 0.94$, ignoring heat-release effects.

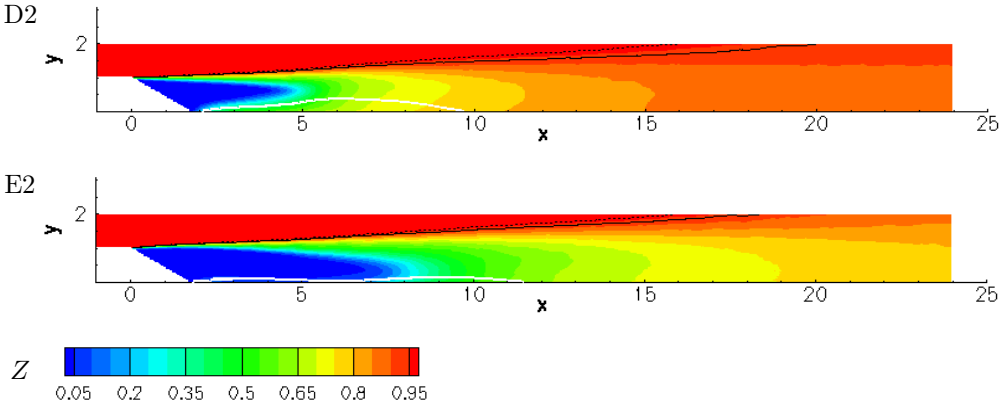

Figure 4.22: Mean scalar fields for Cases D2 and E2. Black continuous contour corresponds to the stoichiometric mixture fraction for a notional octane (C_8H_{18}) fuel, $Z_{\mathrm{st},\,C_8H_{18}} = 0.94$. Dashed contour to the stoichiometric mixture fraction for a notional hydrogen (H_2), $Z_{\mathrm{st},\,H_2} = 0.97$. The white contour near the lower wall corresponds to zero streamwise velocity.

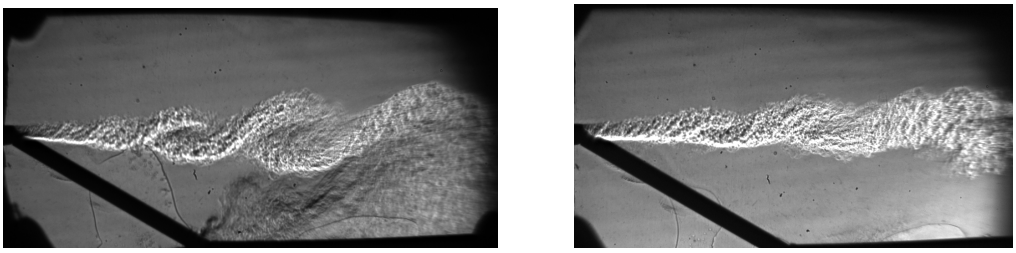

(a) (b)

Figure 4.23: Schlieren visualization of the flow in the expansion ramp geometry from the experiments of Johnson (2005). Upper stream $U_1 \approx 120$ m/s, lower steam $U_R \approx 5.5$ m/s (left) and $U_R \approx 12.5$ m/s.

The contour of stoichiometric mixture fraction for a notional octane (C_8H_{18}) fuel, $Z_{\mathrm{st},\,C_8H_{18}} = 0.94$, is also drawn in Fig. 4.21 for a top stream of air and a lower stream of octane. The contour of $Z_{\mathrm{st},\,C_8H_{18}} = 0.94$ corresponds to the instantaneous location of the mixture fraction assuming that the reaction between air and C_8H_{18} occurs infinitely fast on a surface of negligible thickness and any heat-release effects are negligible.

4.4.1 Mean fields

The difference between the low and high injection cases is illustrated by the mean scalar fields of Fig. 4.22. For low injection, the pure lower-stream fluid is consumed by five step heights on average, whereas in the high-injection case, pure lower-stream fluid can be found up to $x = 8$. The stoichiometric mixture fraction contours for octane and hydrogen, $Z_{\mathrm{st},\,H_2} = 0.97$, are also drawn in Fig. 4.22. A lower stream composed of 50% air–50% H_2 results in the same stoichiometric mixture fraction as C_8H_{18}. Despite the big differences in the flow fields in the recirculation region, the mean location of the "flame" does not change significantly.

An important implication for high-speed air-breathing propulsion applications is that for the present configuration the LES predicts that the top, "air," stream is fully mixed at the required mixture fractions and it is available to combust the fuel. This occurs between $x = 15$–20, or about ten duct heights downstream of the injection, and for the current conditions, appears to be only weakly dependent on the injection ratio, at least in the case of negligible heat-release effects.

4.4.2 Probability density functions of the passive scalar

Total (resolved and subgrid) probability density functions for Cases D2 and E2 are shown in Fig. 4.24. The large differences in the PDFs of Fig. 4.24 are a consequence of the change in the character of the recirculation of mixed fluid near the lower wall. Specifically, at location $x = 8$, the effect of the recirculating flow on the PDFs is clearly seen. At low injection, mixed fluid can be found in the lower half of the duct, whereas at high injection, apart from very near the lower wall, the fluid remains unmixed below the primary shear layer. Moreover, for the low-injection case, the composition is more homogenous, as illustrated by the PDFs at $x = 8$ and $x = 12$ in Fig. 4.24. In this respect, the recirculation zone and the presence of the secondary mixing layer are successful in enhancing the mixing by producing a narrower (of smaller variance) PDFs of mixture fraction in the lower half of the duct.

4.4.3 Comparison with experimental data

The comparison of the pressure coefficients is shown in Figs. 4.25 and 4.26 for Cases D2 and E2, respectively. The agreement for the low-injection case is satisfactory with the results being similar

D2 E2

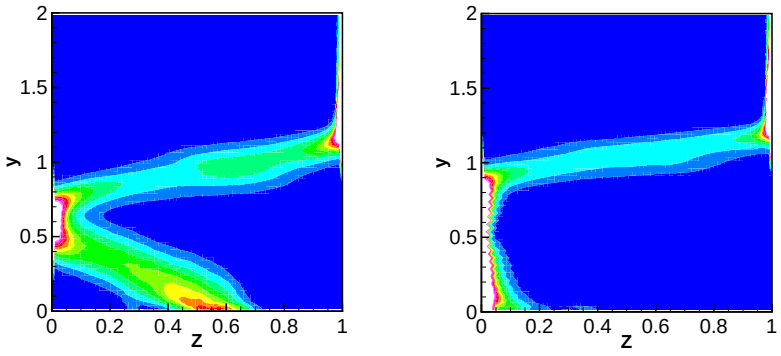

(a) $x = 4$

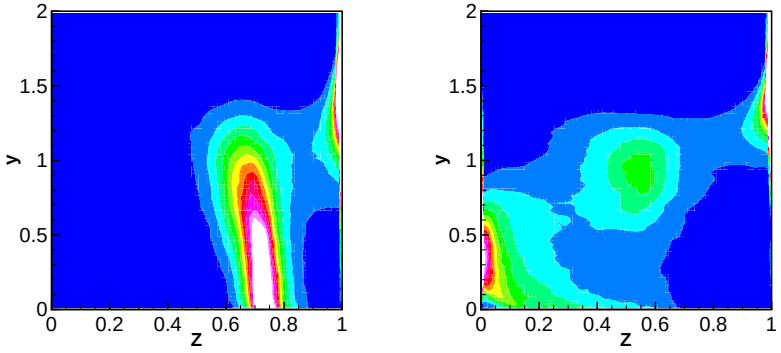

(b) $x = 8$

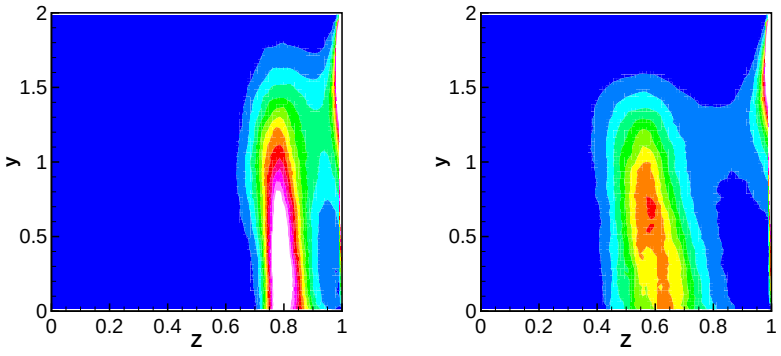

(c) $x = 12$

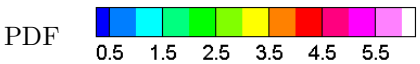

Figure 4.24: Total (resolved and subgrid) scalar probability density functions for Cases D2, low injection, (left column) and E2, high injection, at three streamwise locations. Contours are drawn at identical intervals in all panels.

to the comparison for Cases C2 and C3. The mean reattachment length appears to be overpredicted by the LES by about one step height while the sign of the pressure coefficient is reversed, with the flow in the simulation recovering pressure through the entire length of the computational domain.

The sign of the pressure coefficient before reattachment, as predicted by the simulation, agrees with the measurements for the high-injection case (Fig. 4.26), though its value is underpredicted. Nevertheless, this is an encouraging result, since the trend of C_p with respect to mass-injection ratio is captured by the simulations, with the pressure in LES predictions being more sensitive to changes in injection velocity for the present conditions.

The mean reattachment length in the simulation is about four step heights larger than the experiment. Comparing the C_p profiles for low and high injection, the simulations predict that when doubling the amount of mass flux of the lower stream, keeping the upper stream conditions unchanged, the mean reattachment of the primary shear layer moves 3–4 step heights downstream (Figs. 4.25 and 4.26). In contrast, the measurements show that the reattachment point remains almost unaffected by the increase in injection. The trend of the measurements is at variance with the expected behavior of the flow.

Figure 4.27 shows the total pressure comparisons at $x = 9.4$. The most important feature of the experimental profiles of Fig. 4.27 is the indication of separation near the top wall where the total pressure is decreasing from the free-stream value. The measurements are performed with upstream-facing total pressure probes, thus if the local flow reverses direction for a fraction of the run time, the average value decreases. The same is true for the region near the lower wall. The flow is moving upstream for a fraction of the time that depends on the mean length of the recirculation and its unsteadiness. If at $x = 9.4$ the measurements near the lower wall are contaminated with upstream-moving flow, then the actual total pressure values should have higher values, bringing them in closer agreement with the simulation prediction for Case D2.

The comparison of mixing statistics for Cases D2 and E2 is shown in Figs. 4.28 and 4.28. Normalized temperature-rise profiles are compared against the experimental measurements for $\phi = 1/8$ and $\phi = 8$ at two streamwise locations, $x = 7.2$ and $x = 9.4$. The upstream location is inside the mean recirculation region for both cases, whereas the downstream location is after reattachment for the low-injection case and at about the mean reattachment location for the high injection. Similar to Cases C1 and C2, the mixing layer appears to extend more inside the top free stream, especially in Case E2.

Careful examination of the estimates of the probability of mixed fluid from the experiments shows that the transverse extent of the mixing zone is not growing between the upstream and the downstream location. For Case E2, it appears to be contracting. This can be attributed to the presence of a separation bubble on the upper guide wall that can displace the top stream downwards, thereby reducing the value of the adverse pressure gradient in the flow away from the separation

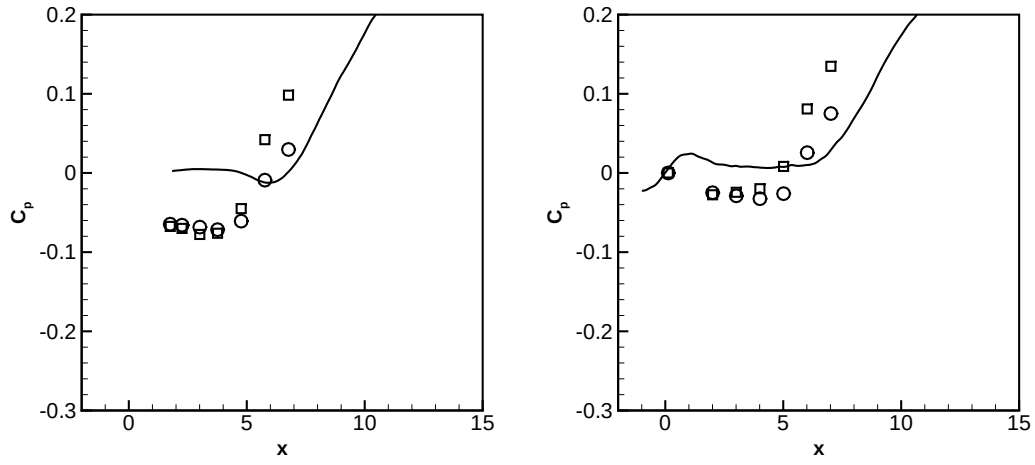

(a) Lower guide wall

(b) Upper guide wall

Figure 4.25: The pressure coefficient on the lower and upper guide walls for Case D2. Symbols correspond to a pair of experiments at the same conditions.

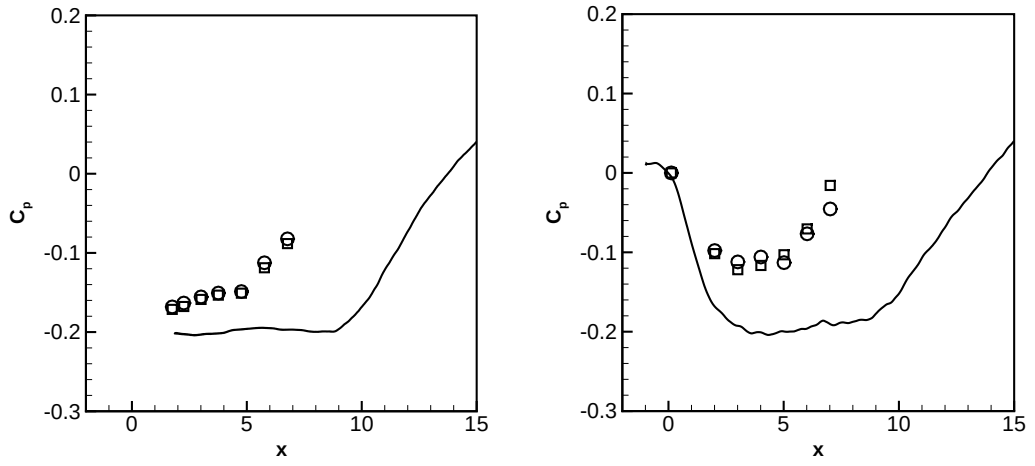

(a) Lower guide wall

(b) Upper guide wall

Figure 4.26: The pressure coefficient on the lower and upper guide walls for Case E2. Symbols correspond to a pair of experiments at the same conditions.

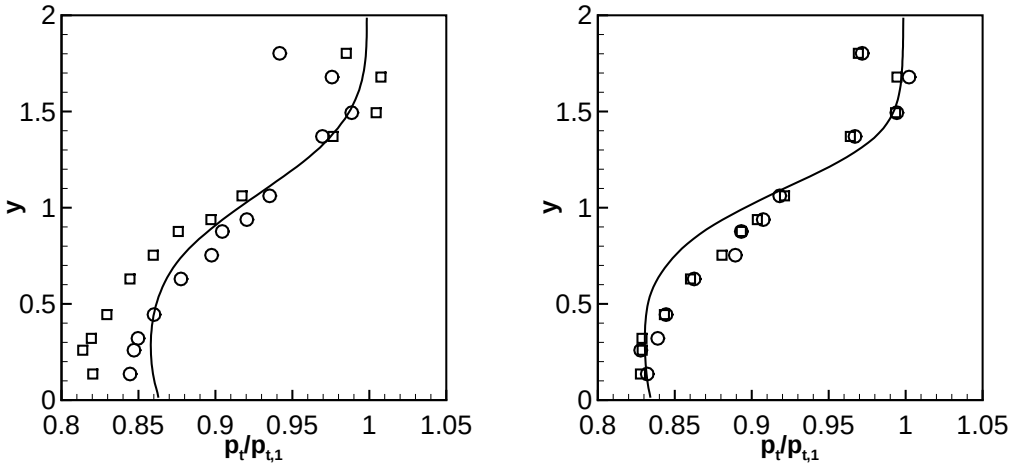

(a) Case D2

(b) Case E2

Figure 4.27: Total pressure comparison for Cases D2 and E2 at $x = 9.4$. Symbols correspond to a pair of experiments at the same conditions.

wall and decrease the height of the mixing zone.

Similar to Cases C1–3, the normalized distance between the measurements and the predictions is shown in Table 4.4.

Case	Rake location	Normalized temperature rise		Probability of mixed fluid
		$\phi = 1/8$	$\phi = 8$	
D2	Upstream	0.27	0.14	0.12
D2	Downstream	0.25	0.13	0.10
E2	Upstream	0.25	0.45	0.31
E2	Downstream	0.32	0.21	0.18

Table 4.4: Comparison of the difference between the experiments and the simulation for Cases D2 and E2 for two downstream locations. Upstream rake location is at $x = 7.2$ and downstream at $x = 9.4$. The values of the table correspond to the L_1 distance between the data of experiments and simulations normalized by the L_1 norm of the experimental curves.

Bergthorson et al. (2008) developed a model for the pressure coefficient at the exit of the test section located at $L_\mathrm{p} = 7.2$. They carry out a control-volume analysis assuming a linear variation of the streamwise velocity profile at the exit, with $u = 0$ on the lower wall. Input to the model are the top and bottom stream (uniform) inflow velocities, U_1 and U_R, respectively, and the inflow pressure, assumed to be the same for both streams. The density is assumed uniform. The resulting pressure

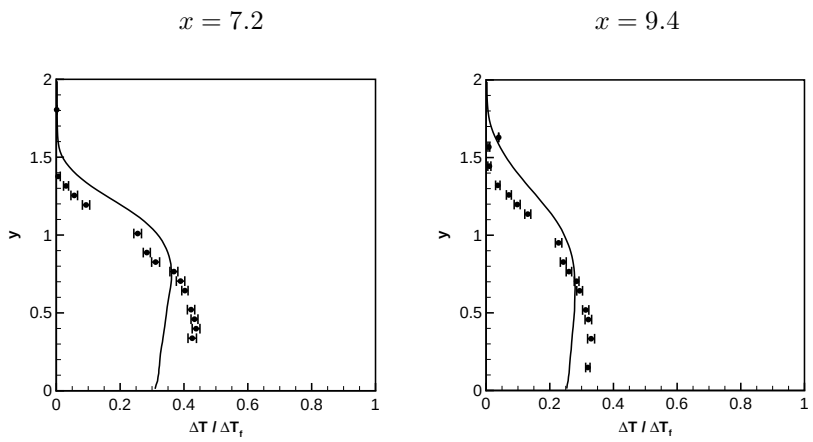

(a) Normalized temperature rise for $\phi = 1/8$

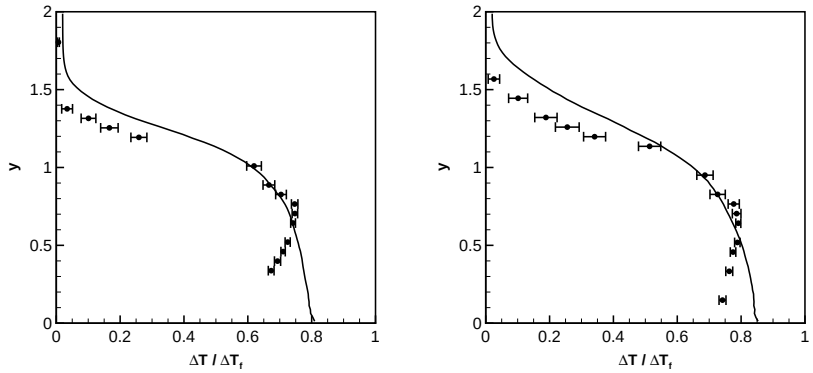

(b) Normalized temperature rise for $\phi = 8$

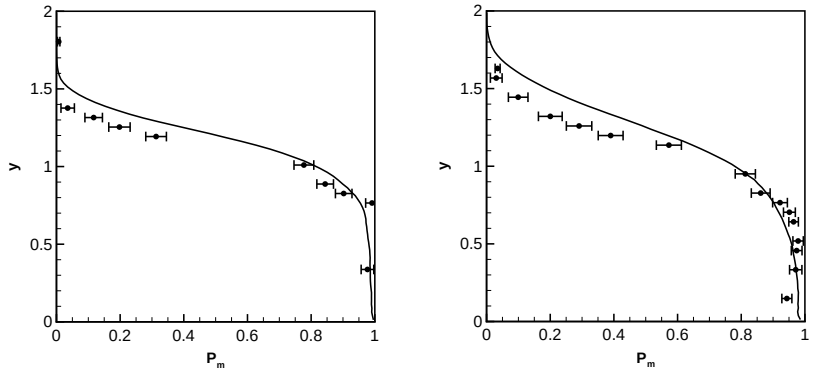

(c) Probability of mixed fluid P_{m}

Figure 4.28: Normalized temperature rise and probability of mixed fluid for Case D2. Left column panels correspond to the upstream rake location, $x = 7.2$, and right column to the downstream rake location, $x = 9.4$. Experimental measurements are indicated by symbols.

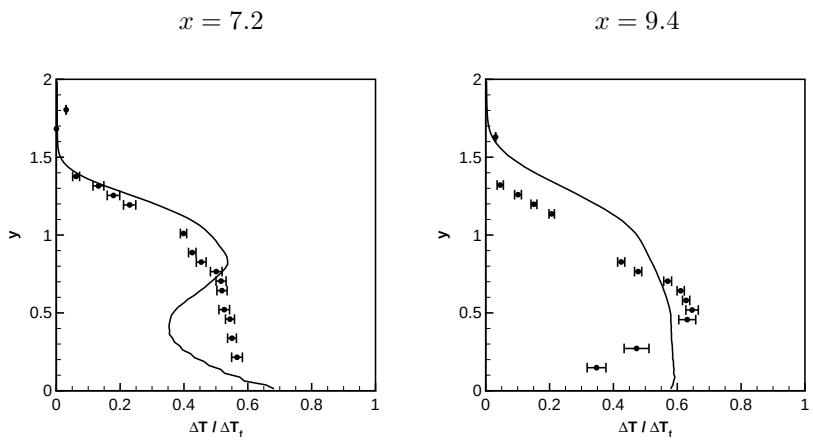

(a) Normalized temperature rise for $\phi = 1/8$

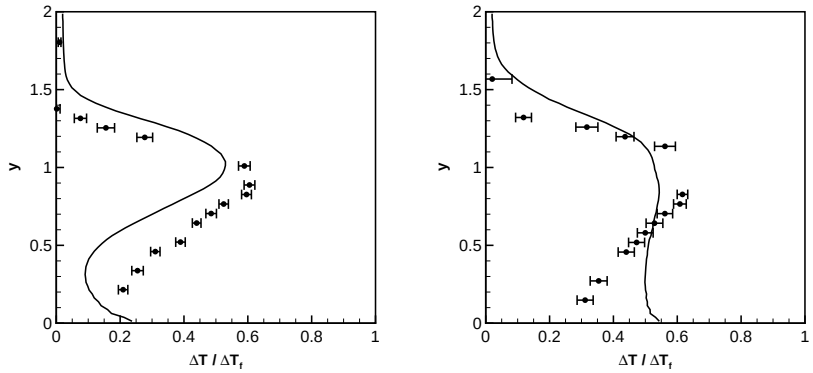

(b) Normalized temperature rise for $\phi = 8$

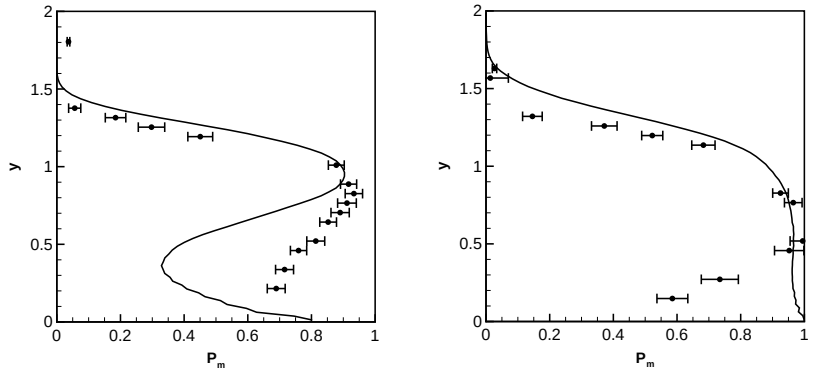

(c) Probability of mixed fluid P_{m}

Figure 4.29: Normalized temperature rise and probability of mixed fluid for Case E2. Left column panels correspond to the upstream rake location, $x = 7.2$, and right column to the downstream rake location, $x = 9.4$. Experimental measurements are indicated by symbols.

coefficient is then given by

$$C_p = \frac{1}{3} - \frac{4}{3\,\sin\alpha}\,\frac{U_\mathrm{R}}{U_1} + \left(1 - \frac{2}{3\,\sin^2\alpha}\right)\left(\frac{U_\mathrm{R}}{U_1}\right)^2, \tag{4.34}$$

where $\alpha = 30^\circ$ is the angle of the ramp with respect to the top stream (see Fig. 1.1). The model for the pressure coefficient is plotted in Fig. 4.30 together with the measurements of Johnson (2005) and Bergthorson et al. (2008) and the prediction of the simulations. The model is in accord with the experimental measurements.

The pressure coefficient is a function of streamwise distance that is implicitly represented in the C_p model by the choice of exit velocity profile. As a consequence, Eq. 4.34 will agree with experimental data if the velocity profile at the end of the test section is linear, or more generally, if the velocity profile at the end of the test section has the same momentum flux as the one assumed. The friction on the walls is expected to be negligible. The velocity profiles from the simulations at L_p show that the choice of a linear velocity profile may not be well justified (Fig. 4.31).

4.5 Discussion

The most important of the modeling assumptions in the current study is the treatment of solid boundaries as no-stress boundaries. The experimental measurements show that the flow separates on the top wall in the adverse pressure gradient region following the reattachment of the primary shear layer. This behavior of the flow cannot be reproduced by the boundary conditions adopted in the simulations, a limitation that is important in accurately predicting the level of mixing even away from walls. Separation can change the location of the mixing zone by displacing the top stream downwards, while the modification of the local pressure and velocity fields can affect the growth and dynamics of the mixing layer. The probability of mixed-fluid profiles of Case E2 (Fig. 4.29) show evidence of the downwards displacement of the mixing zone.

As an *a posteriori* test, the separation criterion for a turbulent boundary layer of Stratford (1959) is applied to the mean flow field of the simulations. This separation criterion relates the change in the pressure coefficient, C_p, to the Reynolds number of the boundary layer, $Re_x = U\,x/\nu$, and for Reynolds numbers of the order of 10^6 is,

$$C_p\left(x\frac{\mathrm{d}C_p}{\mathrm{d}x}\right)^{\frac{1}{2}} = 0.39\,(10^{-6}Re_x)^{\frac{1}{10}}, \tag{4.35}$$

when $\mathrm{d}^2p/\mathrm{d}x^2 \geq 0$ and $C_p \leq 4/7$. The distance x was computed from the inflow resulting in a higher Reynolds number by neglecting the effects of favorable pressure gradient regions which results in a more conservative estimate.

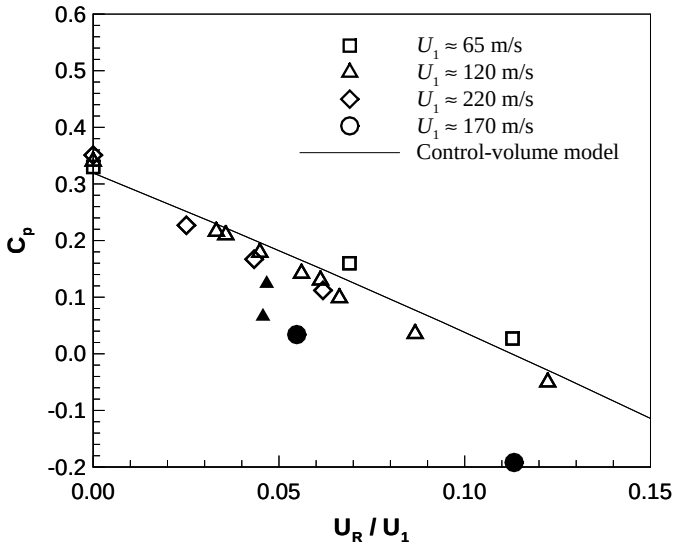

Figure 4.30: Pressure coefficient at the exit of the test section, $x = 7.2$, as a function of the mass-injection ratio. Open symbols correspond to the experiments of Johnson (2005) and Bergthorson et al. (2008), filled symbols to the present simulations (Cases C2, C3, D2 and E2). Continuous line is the control volume model of Bergthorson et al. (2008) (Eq. 4.34).

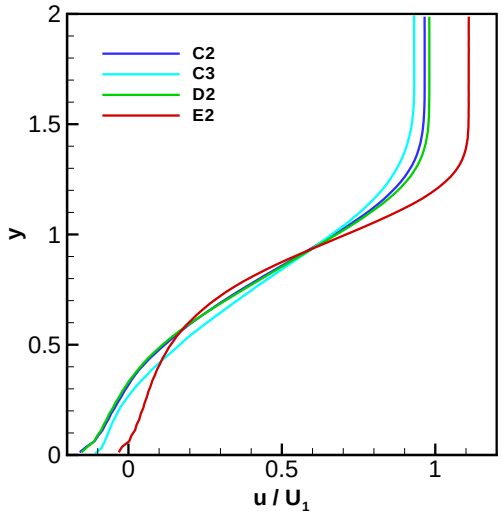

Figure 4.31: Computed streamwise velocity profiles at $x = 7.2$

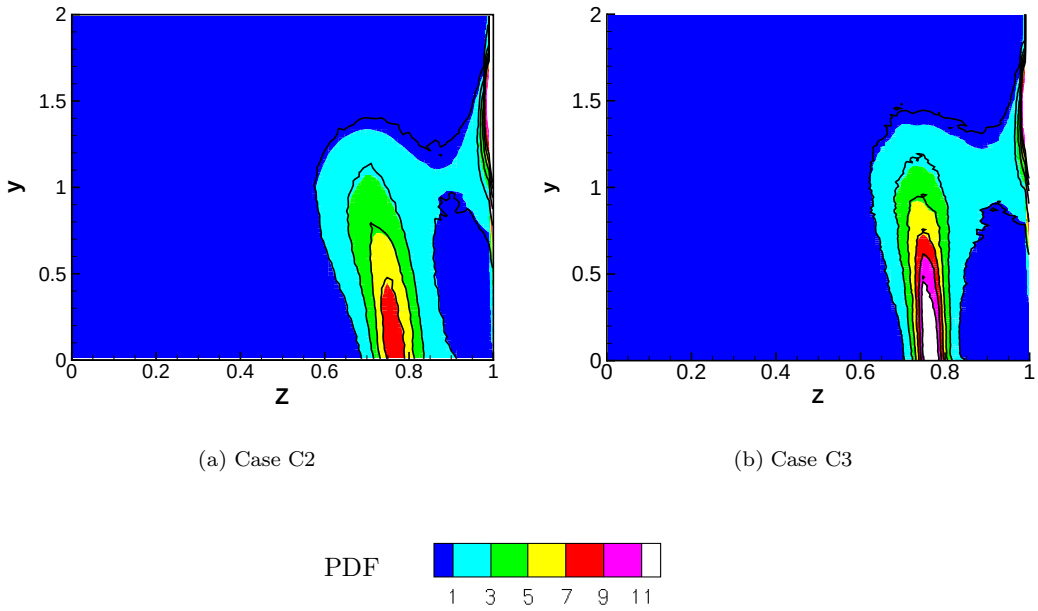

(a) Case C2

(b) Case C3

Figure 4.32: Probability density functions at $x = 8$ for two resolutions, Case C3 has twice the resolution of Case C2. Color contours correspond to the the total PDF whereas black contours to the resolved. Both contour sets have identical increments.

The separation criterion of Stratford (1959) does not predict separation for any of the computed mean pressure distributions on the upper guide wall. Although the conditions for using the criterion are satisfied by the mean flow, the character of the time-dependent flow field differs significantly from the flows the criterion was validated for. Stratford's criterion was developed for steady flows over airfoils or similar bodies in a steady free stream. On the other hand, the flow in the expansion ramp geometry is unsteady with large-scale structures interacting with each other and the solid boundaries. The induced instantaneous adverse pressure distribution on the walls is therefore more severe than the pressure gradients of the mean field. As a consequence, the separation bubble is likely to be very unsteady, with a time dependence that is in phase with the shear-layer large-scale structure, and can alter the dynamics of the mixing layer. The effects of the unsteady flow are important and a successful treatment of the boundary layers should be able to predict the response of the turbulent boundary layer and the separation/reattachment in a rapidly varying flow field.

Comparison with experimental measurements suggests that most of the differences observed in the mixing statistics can be attributed to discrepancies in the large-scale flow field. In all cases considered in the present study, the probability of mixed fluid is found to be in better agreement with the estimates from the experimental measurements than the comparison of the pressure coefficients. This is a result of the complex flow in the expansion ramp geometry and the interaction of the turbulent flow with the solid boundaries. Consequently, accurate prediction of three-dimensional boundary-layer effects, including separation, and the growth rate of the shear layer, are a prerequisite

for a reliable simulation of the flow and the mixing.

One of the key elements in this study is the prediction of the total probability density function of the passive scalar, estimated by correcting the resolved PDF using an assumed distribution for the subgrid field. Figure 4.32 shows the difference between the total and resolved PDFs for Cases C2 and C3. For these cases, satisfactory agreement with experiments of the probability of mixed fluid was achieved (Fig. 4.20). Therefore, with a high level of confidence, it can be concluded that the PDFs of Fig. 4.32 provide a good representation of the true distribution of the mixture.

The difference between the total and resolved PDF was found to be small for all cases simulated. As can be seen from Fig. 4.32, this difference remains almost constant as the grid resolution is doubled. Almost all of the variance of the PDFs of the scalar is contributed by the resolved field. It appears that for the current conditions, the spanwise and time variation of the scalar at position (x, y) results in a PDF that is a good approximation of the actual mixture PDF at (x, y). Although this conclusion may hold for flows with Schmidt numbers of order unity, like the one simulated here, it is expected that the subgrid moments and shape of the PDF will become of greater importance as the Schmidt number and the fraction of the scalar spectrum and variance represented by the SGS model increase. Hill et al. (2006) also concluded that the contribution of the subgrid scalar variance was small compared to the resolved counterpart in simulations of Richtmyer–Meshkov instability using the stretched vortex LES–SGS model. They also incorporated the effects of variable Schmidt number and found relatively small changes in the shape of the PDF with respect to the Schmidt number due to the logarithmic dependence of the subgrid variance on the Schmidt number.

Accordingly, the dependence of the total PDF on the subgrid contribution to the distribution is weak, as the subgrid variance is always small. As a consequence, the present agreement between experiments and LES predictions cannot be regarded as validation of the subgrid beta distribution.

Chapter 5

Summary and conclusions

5.1 Summary

The flow field and mixing in an expansion-ramp geometry was studied using large-eddy simulation (LES) with subgrid scale (SGS) modeling employing the stretched-vortex model for momentum and scalar subgrid turbulent transport (Lundgren, 1982; Voelkl et al., 2000; Pullin, 2000; Pullin & Lundgren, 2001). The predictions of the LES were compared against the experimental measurements of Johnson (2005) and Bergthorson et al. (2008) and found to be in good agreement, given the high Reynolds number of the flow and the modeling difficulties presented by the SGS scalar transport. The mixing was studied by tracking a passive scalar without taking into account the effects of chemical reactions and heat release, an approximation expected to be adequate in view of the experiments that were conducted in parallel.

The approach followed in this work relies on verification and validation of the numerical methods and turbulence models, focusing on developing a predictive computational framework for turbulent-mixing applications based on non-dissipative approximations of the spatial derivatives and a turbulence model based on physical arguments.

For the type of unsteady flows of interest here, the choice and implementation of the boundary closure of the discrete equations is of key importance. Simple exact solutions of the equations of motion can be used for the verification of the interior scheme. A simple vortical solution of the Euler equations was used to verify the order of accuracy on a periodic domain.

For the assessment of the computer code including the boundary closure, a method utilizing results from linear stability analysis (LSA) theory was developed. LSA can be used to compute unstable perturbations to a flow, subject to certain approximations. The perturbations computed from LSA are then used as an inflow condition to the flow computed by the solver been assessed. An alternative approach based on the use of correlations was developed by which the solution obtained from a numerical solver is correlated with the LSA solution. The comparison in terms of a correlation helps assess whether the perturbations evolve correctly and grow at the expected rate. The growth

rate of the perturbations for an unbounded (effectively) incompressible shear layer and a confined compressible shear layer was found to be in excellent agreement with the prediction of the LSA.

The LES equations were discretized on a regular Cartesian grid and the geometry of the ramp-injection configuration was represented implicitly by a level-set function. Boundary conditions were applied on the level-set using the ghost fluid method (GFM). The GFM boundary condition for the assumed-uniform subsonic inflow through the ramp was implemented in characteristic form and results show that for the cases considered it did not have a negative effect on the stability of the mean flow.

The LES–SGS model used in this study has also been used in the same form in simulations of Richtmyer–Meshkov instability (Hill et al., 2006), a turbulent planar jet, (Pantano et al., 2007), and turbulent channel (Pantano et al., 2008) flows successfully. No LES–SGS model-parameters were adjusted in these studies. This is an encouraging result for the prediction of turbulent flows.

Specifically, the recirculating flow between the ramp and the reattachment of the primary shear layer is present in the LES, together with the secondary shear layer at the base of the ramp where fluid mixed in the primary shear layer is further diluted by the pure lower stream. The magnitude of the velocity of upstream-moving flow near the lower wall is 10–15% of the top free stream for mass-injection ratios of about 1/10, but becomes negligible as the flow tends towards a free shear layer for higher mass-injection ratios of about 1/5.

The mean reattachment length of the primary shear layer was somewhat overpredicted by the simulations, a result that can be attributed to the longer length required for transition of the primary shear layer to a three-dimensional state in the simulations compared to experiments.

Total (resolved and subgrid) probability density functions (PDFs) of the passive scalar were estimated using an assumed beta-distribution model for the subgrid scalar field. The difference between the total and resolved PDFs was found to be small, implying that most of the scalar variance is contributed by the resolved fields rather than the subgrid component. This conclusion is in agreement with the observations of Hill et al. (2006) in LES of Richtmyer–Meshkov instability.

PDFs of the scalar show the effects of the recirculating flow on the quantity of the mixed fluid, where high probabilities of mixed fluid can be found in the lower half of the duct. This would not be possible with a free shear layer at similar free-stream conditions at the same streamwise location. Moreover, the pure lower-stream fluid is depleted by 4 step heights in the low-injection cases, and about 8 step heights in the high-injection case.

The flow was computed for three resolutions, differing by a factor of 2 in each direction between them, in order to investigate convergence. The mean fields and the scalar PDFs exhibit good resolution independence for the two finer grids used. The coarse grid failed to provide accurate predictions of the flow. The intermediate resolution grid has a good balance between acceptable error level and computational cost and can be used to provide a criterion for the resolution requirement

by the LES: the flow is well predicted when the ratio of subgrid-to-total turbulent kinetic energy is less than 0.2.

The most significant modeling assumption was the treatment of walls as stress-free (slip) boundaries. As a consequence, the flow in the simulation does not separate from the top wall in the adverse pressure gradient region following the reattachment of the shear layer. The analysis of the mean pressure fields showed that separation is likely to be attributable to the unsteady flow than the mean pressure recovery.

Inclusion of boundary-layer effects in the simulations is expected to bring the LES–SGS results in closer agreement with the measurements. Moreover, the effects of entropy production through friction become important in the extension of the current simulations to supersonic top streams. Apart from boundary-layer modeling considerations, the present LES methodology can be used to study the same flow with a supersonic top stream without any modification. In this case, the presence of shock waves results in an increase of the computational cost. Given a boundary-layer model with moderate resolution requirements and the use of the adaptive mesh refinement capability of the present computational framework, such simulations are not out of reach of the current computational capabilities. Using data from a preliminary spatially developing boundary layer simulation employing the stretched-vortex LES–SGS model with the stress boundary condition of Pantano et al. (2008), it can be estimated that inclusion of boundary-layer effects will result in a simulation of about 1 billion computational cells. This estimate assumes that the region near the wall is refined using adaptive mesh refinement, with cell sizes being four times smaller in each direction than the interior of the computational domain.

5.2 Conclusions

The goal of the present work is to provide a prediction for the mixing on a molecular scale in a high-Reynolds-number turbulent shear flow. The approach followed addresses the difficulty of computational simulation of such flows and aims to provide predictions that are free of arbitrary parameters or choices, such as adjustable model constants or computational-grid resolution.

The accuracy and performance of the components of the numerical model are assessed through verification and validation. A novel verification method was developed in order to assess the interior scheme and the boundary closure for an unsteady flow. The projection-based metric developed in this work can be considered as a new class of error metrics for verification, which in combination with the use of linear stability analysis solutions can be used for code assessment using flows with realistic boundary conditions. Although the projection-based metric cannot be used to demonstrate that a numerical scheme is convergent or consistent, it aims to complement existing error metrics and provide a useful tool for code assessment.

Comparison of the LES results with experimental measurements relies on identifying the sources of error and then assessing their contribution to the differences observed. The mean fields and probability density functions of the passive scalar are shown to become independent of the grid resolution as the grid is refined and the resolution requirements are quantified. Simulations do not rely on arbitrary parameter choices and are conducted using well-defined modeling assumptions. Consequently, the effect of all modeling assumptions on the prediction of the flow can be identified and quantified.

The comparison of the LES results with the measurements is limited by the treatment of walls as a slip boundary in the simulation. Nevertheless, this is a valuable assessment of the SGS model as many of the characteristics of the flow are captured even in the absence of boundary-layer effects. The complex character of the flow allows the assessment of the numerical method and SGS model in a realistic configuration.

Bibliography

AIAA, 1998. *AIAA Guide for the Verification and Validation of Computational Fluid Dynamics Simulations*. American Institute of Aeronautics & Astronautics.

Akselvoll, K. & Moin, P., 1996. Large-eddy simulation of turbulent confined coannular jets. *J. Fluid Mech.*, **315**:387–411.

Arienti, M., Hung, P., Morano, E., & Shepherd, J. E., 2003. A level set approach to Eulerian-Lagrangian coupling. *J. Comput. Phys.*, **185**(1):213–251.

Balsara, D. S. & Shu, C. W., 2000. Monotonicity preserving weighted essentially non-oscillatory schemes with increasing high order of accuracy. *J. Comp. Phys.*, **160**:405–452.

Batchelor, G. K., 1959. Small-scale variation of convected quantities like temperature in turbulent fluid. Part 1. General discussion and the case of small conductivity. *J. Fluid Mech.*, **5**:113–133.

Ben-Yakar, A. & Hanson, R. K., 2001. Cavity flame-holders for ignition and flame stabilization in scramjets: An overview. *J. of Propul. Power*, **17**(4):869–877.

Ben-Yakar, A., Mungal, M. G., & Hanson, R. K., 2006. Time evolution and mixing characteristics of hydrogen and ethylene transverse jets in supersonic crossflows. *Phys. Fluids*, **18**: 026101:1–16.

Bergthorson, J. M., Johnson, M. B., Bonanos, A. M., Slessor, M., Su, W.-J., & Dimotakis, P. E., 2008. Molecular mixing and flowfield measurements in a recirculating shear flow. Part I: Subsonic flow. *Phys. Rev. E.* (submitted).

Bilger, R. W., 1975. A note on Favre averaging in variable density flows. *Combust. Sci. Technol.*, **11**:215–217.

Bilger, R. W., 1977. Comment on "Structure of turbulent shear flows: A new look." *AIAA J.*, **15**:1056.

Bilger, R. W., 1993. Conditional moment closure for turbulent reacting flow. *Phys. Fluids*, **5**(2): 436–444.

Blumen, W., 1970. Shear layer instability of an inviscid compressible fluid. *J. Fluid Mech.*, **40**: 769–781.

Blumen, W., Drazin, P. G., & Billings, D. F., 1975. Shear layer instability of an inviscid compressible fluid. Part 2. *J. Fluid Mech.*, **71**:305–316.

Bonanos, A. M., Bergthorson, J. M., & Dimotakis, P. E., 2007. Molecular mixing and flowfield measurements with reacting expansion-ramp combustor. *AIAA Paper* 2007-5417.

Bonanos, A. M., Bergthorson, J. M., & Dimotakis, P. E., 2008a. Mixing measurements in a supersonic expansion-ramp combustor. *Flow Turbul. Combust.*

Bonanos, A. M., Berthorson, J. M., & Dimotakis, P. E., 2008b. Molecular mixing and flowfield measurements in a recirculating shear flow. Part II: Supersonic flow. *Phys. Rev. E.* (submitted).

Bond, C. L., 1999. *Reynolds Number Effects on Mixing in the Turbulent Shear Layer*. Ph.D. thesis, California Institute of Technology. http://resolver.caltech.edu/CaltechETD:etd-03242005-162912.

Breidenthal, R. E., 1978. *A chemically reacting, turbulent shear layer*. Ph.D. thesis, California Institute of Technology.

Brown, G. L. & Roshko, A., 1974. On density effects and large structure in turbulent mixing layers. *J. Fluid Mech.*, **64**:775–816.

Burke, S. P. & Schumann, T. E. W., 1928. Diffusion flames. *Ind. Eng. Chem.*, **20**(1):998–1004.

Callenaere, M., Franc, J. P., Michel, J. M., & Riondet, M., 2001. The cavitation instability induced by the development of a re-entrant jet. *J. Fluid Mech.*, **444**:223–256.

Colonius, T., 2004. Modeling artificial boundary conditions for compressible flow. *Annu. Rev. Fluid Mech.*, **36**:315–345.

Colonius, T., Lele, S. K., & Moin, P., 1997. Sound generation in a mixing layer. *J. Fluid Mech.*, **330**:375–409.

Colucci, P. J., Jaberi, F. A., & Givi, P., 1998. Filtered density function for large eddy simulation of turbulent reacting flows. *Phys. Fluids*, **10**(2):499–515.

Cook, A. W. & Dimotakis, P. E., 2001. Transition stages of Rayleigh–Taylor instability between miscible fluids. *J. Fluid Mech.*, **443**:69–99.

Cook, A. W. & Riley, J. J., 1994. A subgrid model for equilibrium chemistry in turbulent flows. *Phys. Fluids*, **6**(8):2868–2870.

Curran, E. T., Heiser, W. H., & Pratt, D. T., 1996. Fluid phenomena in scramjet combustion systems. *Annu. Rev. Fluid Mech.*, **28**:323–360.

E. T. Curran & S. N. B. Murthy (Eds.), 2000. *Scramjet Propulsion*, volume 189 of *Progress in Astronautics and Aeronautics*. AIAA.

Curran, E. T., 2001. Scramjet engines: The first forty years. *J. of Propul. Power*, **17**:1138–1148.

Deiterding, R., September 2003. *Parallel adaptive simulation of multi-dimensional detonation structures*. Ph.D. thesis, Brandenburgischen Technischen Universität Cottbus.

Deiterding, R. AMROC—Blockstructured Adaptive Mesh Refinement in Object-oriented C++. http://amroc.sourceforge.net, October 2004.

Dimotakis, P. E., 1986. Two-dimensional shear-layer entrainment. *AIAA J.*, **24**:1791–1796.

Dimotakis, P. E., 1991. Turbulent free shear layer mixing and combustion, In: *High-Speed Propulsion Systems*, S. N. B. Murthy & E. T. Curran (Eds.), volume 137 of *Progress in Astronautics and Aeronautics*, pages 265–340, AIAA.

Dimotakis, P. E., April 2000. The mixing transition in turbulent flows. *J. Fluid Mech.*, **409**:69–98.

Dimotakis, P. E., 2005. Turbulent mixing. *Annu. Rev. Fluid Mech.*, **37**:329–356.

Dimotakis, P. E. & Hall, J. L., 1987. A simple model for finite chemical kinetics analysis of supersonic turbulent shear layer combustion. *AIAA Paper* 87-1879.

Dimotakis, P. E. & Brown, G. L., 1976. The mixing layer at high Reynolds number: large-structure dynamics and entrainment. *J. Fluid Mech.*, **78**:535–560.

Dimotakis, P. E. & Miller, P. L., 1990. Some consequences of the boundedness of scalar fluctuations. *Phys. Fluids*, **2**(11):1919–1920.

Drazin, P. G. & Davey, A., 1977. Shear layer instability of an inviscid compressible fluid. Part 3. *J. Fluid Mech.*, **82**:255–260.

Drazin, P. G. & Reid, W. H., 2004. *Hydrodynamic Stability*. Cambridge University Press, Cambridge, U.K.

Ducros, F., Comte, P., & Lesieur, M., 1996. Large-eddy simulation of transition to turbulence in a boundary layer developing spatially over a flat plate. *J. Fluid Mech.*, **326**:1–36.

Eaton, J. K. & Johnston, J. P., 1981. A review of research on subsonic turbulent flow reattachment. *AIAA J.*, **19**(9):1093–1100.

Eckart, C., 1948. An analysis of the stirring and mixing processes in incompressible fluids. *J. Mar. Res.*, **7**(3):265–275.

Effelsberg, E. & Peters, N., 1983. A composite model for the conserved scalar p.d.f. *Combust. Flame*, **50**:351–360.

Egolfopoulos, F. N., Dimotakis, P. E., & Bond, C. L., 1996. On strained flames with hypergolic reactants: the $H_2/NO/F_2$ system in high-speed, supersonic and subsonic mixing-layer combustion. *Proc. Combust. Inst.*, **26**:2885–2893.

Fedkiw, R. P., Aslam, T., Merriman, B., & Osher, S., 1999. A non-oscillatory Eulerian approach to interfaces in multimaterial flows (the Ghost Fluid Method). *J. Comput. Phys.*, **152** (2):89–112.

Freund, J. B., Lele, S. K., & Moin, P., 2000. Compressibility effects in a turbulent annular mixing layer. Part 1. Turbulence and growth rate. *J. Fluid Mech.*, **421**:229–267.

Gao, F. & O'Brien, E. E., 1993. A large-eddy simulation scheme for turbulent reacting flows. *Phys. Fluids A*, **5**:1282–1284.

Germano, M., Piomelli, U., Moin, P., & Cabot, W. H., 1991. A dynamic subgrid-scale eddy viscosity model. *Phys. Fluids A*, **3**:1760–1765.

Ghosal, S., 1996. An analysis of numerical errors in large-eddy simulations of turbulence. *J. Comput. Phys.*, **125**:187–206.

Ghosal, S., 1999. Mathematical and physical constraints on large-eddy simulation of turbulence. *AIAA J.*, **37**:425–433.

Goldberg, S., 1960. *Probability: An Introduction*. Prentice-Hall Inc, Englewood Cliffs, New Jersey.

Gottlieb, S., Shu, C. W., & Tadmor, E., 2001. Strong stability-preserving high-order time discretization methods. *SIAM Rev.*, **43**(1):89–112.

Gutmark, E. J., Schadow, K. C., & Yu, K. H., 1995. Mixing enhancement in supersonic free shear flows. *Annu. Rev. Fluid Mech.*, **27**:375–417.

Hall, J. L., 1991. *An Experimental Investigation of Structure, Mixing and Combustion in Compressible Turbulent Shear Layers*. Ph.D. thesis, California Institute of Technology. http://resolver.caltech.edu/CaltechETD:etd-09232005-141544.

Hall, J. L., Dimotakis, P. E., & Roseman, H., 1991. Some measurements of molecular mixing in compressible turbulent shear layers. *AIAA Paper* 91-1719.

Han, G., Tumin, A., & Wygnanski, I., 2000. Laminar-turbulent transition in Poiseuille pipe flow subjected to periodic perturbation emanating from the wall. Part 2. Late stage of transition. *J. Fluid Mech.*, **419**:1–27.

Hatton, L., 1997. The T experiments: Errors in scientific software. *IEEE Comput. Sci. Eng.*, **4** (2):27–38.

Hermanson, J. C. & Dimotakis, P. E., 1989. Effects of heat release in a turbulent, reacting shear layer. *J. Fluid Mech.*, **199**:333–375.

Hill, D. J., Pantano, C., & Pullin, D. I., 2006. Large-eddy simulation and multiscale modelling of a Richtmer–Meshkov instability with reshock. *J. Fluid Mech.*, **557**:29–61.

Hill, D. J. & Pullin, D. I., 2004. Hybrid tuned center-difference-WENO method for large eddy simulations in the presence of strong shocks. *J. Comput. Phys.*, **194**(2):435–450.

Hollo, S. D., McDaniel, J. C., & R. J. Hartfield, J., 1994. Quantitative investigation of compressible mixing: Staged transverse injection into Mach 2 flow. *AIAA J.*, **32**(3):528–534.

Honein, A. E. & Moin, P., 2004. Higher entropy conservation and numerical stability of compressible turbulence simulations. *J. Comput. Phys.*, **201**(2):531–545.

Hulek, T. & Lindstedt, R., 1998. Joint scalar-velocity pdf modelling of finite rate chemistry in a scalar mixing layer. *Combust. Sci. Technol.*, **136**(1):303–331.

Island, T. C., Urban, W. D., & Mungal, M. G., 1996. Quantitative scalar measurements in compressible mixing layers. *AIAA Paper* 1996-0685.

Jiménez, J., Ducros, F., Cuenot, B., & Bédatb, B., 2001. Subgrid scale variance and dissipation of a scalar field in large eddy simulations. *Phys. Fluids*, **13**:1748–1754.

Jiménez, J., Liñán, A., Rogers, M. M., & Higuera, F. J., 1997. *A priori* testing of subgrid models for chemically reacting non-premixed turbulent shear flows. *J. Fluid Mech.*, **349**:149–171.

Johnson, M. B., 2005. *Aerodynamic Control and Mixing with Ramp Injection.* Engineer's thesis, California Institute of Technology. http://resolver.caltech.edu/CaltechETD:etd-05262005-112117.

Kaiktsis, L. & Monkewitz, P. A., 2003. Global destabilization of flow over a backward-facing step. *Phys. Fluids*, **15**(12):3647–3658.

Kannepalli, C. & Piomelli, U., 2000. Large-eddy simulation of a three-dimensional shear-driven turbulent boundary layer. *J. Fluid Mech.*, **423**:175–203.

Kerstein, A. R., 1988. A linear-eddy model of turbulent scalar transport and mixing. *Combust. Sci. Technol.*, **60**:391–421.

Kerstein, A. R., 1989. Linear-eddy modeling of turbulent transport. II—Application to shear layer mixing. *Combust. Flame*, **75**:397–413.

Kerstein, A. R., 1990. Linear-eddy modelling of turbulent transport. Part 3. Mixing and differential molecular diffusion in round jets. *J. Fluid Mech.*, **216**:411–435.

Kerstein, A. R., 1999. One-dimensional turbulence: model formulation and application to homogeneous turbulence, shear flows, and buoyant stratified flows. *J. Fluid Mech.*, **392**:277–334.

Klimenko, A. Y., 1990. Multicomponent diffusion of various admixtures in turbulent flow. *Fluid Dynamics*, **25**:327–334.

Klimenko, A. Y. & Bilger, R. W., 1999. Conditional moment closure for turbulent combustion. *Prog. Energy Combust. Sci.*, **25**:595–687.

Knupp, P. & Salari, K., 2003. *Verification of Computer Codes in Computational Science and Engineering*. Chapman and Hall/CRC, Boca Raton, Florida.

Konrad, J. H., 1976. *An Experimental Investigation of Mixing in Two-Dimensional Turbulent Shear Flows with Aplications to Diffusion-Limited Chemical Reactions*. Ph.D. thesis, California Institute of Technology.

Koochesfahani, M. M. & Dimotakis, P. E., 1986. Mixing and chemical reactions in a turbulent liquid mixing layer. *J. Fluid Mech.*, **170**:83–112.

Kosovic, B., Pullin, D. I., & Samtaney, R., 2002. Subgrid-scale modelling for large-eddy simulations of compressible turbulence. *Phys. Fluids*, **14**:1511–1522.

Kutschenreuter, P., 2000. Supersonic flow combustors, In: *Scramjet Propulsion*, S. N. B. Murthy & E. T. Curran (Eds.), volume 189 of *Progress in Astronautics and Aeronautics*, pages 513–568, AIAA.

Landau, L. D. & Lifshitz, E. M., 1959. *Fluid Mechanics*, volume 6 of *Course of Theoretical Physics*. Pergamon.

Leonard, A., 1974. Energy cascade in large-eddy simulations of turbulent fluid flows. *Advances in Geophysics*, **18**:237–248.

Lesieur, M. & Metais, O., 1996. New trends in large-eddy simulations of turbulence. *Annu. Rev. Fluid Mech.*, **28**:45–82.

Lessen, M., Fox, J. A., & Zien, H. M., 1965. On the inviscid stability of the laminar mixing of two parallel stream of a compressible fluid. *J. Fluid Mech.*, **23**:355–367.

Lessen, M., Fox, J. A., & Zien, H. M., 1966. Stability of the laminar mixing of two parallel streams with respect to supersonic disturbances. *J. Fluid Mech.*, **25**:737–742.

Liu, X. D., Osher, S., & Chan, T., 1994. Weighted essentially non-oscillatory schemes. *J. Comp. Phys.*, **126**:202–228.

Lundgren, T. S., 1982. Strained spiral vortex model for turbulent fine structure. *Phys. Fluids*, **25**:2193–2203.

Matheou, G., Pantano, C., & Dimotakis, P. E., 2008. Verification of a fluid-dynamics solver using correlations with linear stability results. *J. Comput. Phys.*, **227**(11):5385–5396.

Mattner, T. W., Pullin, D. I., & Dimotakis, P. E., 19–23 July 2004. Large eddy simulations of miscible Rayleigh–Taylor instability. In *9th Intl Workshop on the Physics of Compressible Turbulent Mixing*, Cambridge, U.K.

McDonald, R. P., 1985. *Factor Analysis and Related Methods*. Lawrence Erlbaum Associates, Hillside, New Jersey.

Mellado, J. P., Sarkar, S., & Pantano, C., 2003. Reconstruction subgrid models for non-premixed combustion. *Phys. Fluids*, **15**:3280–3307.

Meneveau, C. & Katz, J., 2000. Scale-invariance and turbulence models for large-eddy simulation. *Annu. Rev. Fluid Mech.*, **32**(1):1–32.

Metais, O. & Lesieur, M., 1992. Spectral large-eddy simulation of isotropic and stably stratified turbulence. *J. Fluid Mech.*, **239**:157–194.

Metcalfe, R. W., Orszag, S. A., Brachet, M. E., Menon, S., & Riley, J. J., 1987. Secondary instability of a temporally growing mixing layer. *J. Fluid Mech.*, **184**:207–243.

Meyers, J., Geurts, B. J., & Baelmans, M., 2003. Database analysis of errors in large-eddy simulation. *Phys. Fluids*, **15**:2740–2755.

Michalke, A., 1964. On the inviscid instability of the hyperbolic-tangent velocity profile. *J. Fluid Mech.*, **19**(4):543–556.

Misra, A. & Pullin, D. I., 1997. A vortex-based subgrid stress model for large-eddy simulation. *Phys. Fluids*, **9**:2443–2454.

Moin, P., Squires, K., Cabot, W., & Lee, S., 1991. A dynamic subgrid-scale model for compressible turbulence and scalar transport. *Phys. Fluids A*, **7**:2746–2757.

Mungal, M. G. & Dimotakis, P. E., 1984. Mixing and combustion with low heat release in a turbulent shear layer. *J. Fluid Mech.*, **148**:349–382.

Oberkampf, W. L. & Trucano, T. G., 2002. Verification and validation in computational fluid dynamics. *Progress in Aerospace Sciences*, **38**(3):209–272.

Oefelein, J. C., 2006. Large eddy simulation of turbulent combustion processes in propulsion and power systems. *Progress in Aerospace Sciences*, **42**(1):2–37.

Osher, S. & Sethian, J., 1988. Fronts propagating with curvature-dependent speed: algorithms based on Hamilton–Jacobi formulations. *J. Comput. Phys.*, **79**(1):12–49.

Pantano, C., Deiterding, R., Hill, D. J., & Pullin, D. I., 2007. A low-numerical dissipation patch-based adaptive mesh refinement method for large-eddy simulation of compressible flows. *J. Comput. Phys.*, **221**(1):63–87.

Pantano, C., Pullin, D. I., Dimotakis, P. E., & Matheou, G., 2008. LES approach for high Reynolds number wall-bounded flows with application to turbulent channel flow. *J. Comput. Physics*. (In press).

Pantano, C. & Sarkar, S., 2001. A subgrid model for nonlinear functions of a scalar. *Phys. Fluids*, **13**(12):3803–3819.

Papamoschou, D. & Roshko, A., 1988. The compressible turbulent shear layer: an experimental study. *J. Fluid Mech.*, **197**:453–477.

Partridge, D., 1991. *A new guide to artificial intelligence*. Ablex Publishing Corp., Norwood, New Jersey.

Peters, N., 1984. Laminar diffusion flamelet models in non-premixed turbulent combustion. *Prog. Energy Combust. Sci.*, **10**(3):319–339.

Peters, N., 2000. *Turbulent combustion*. Cambridge University Press, Cambridge, U.K.

Pierce, C. D. & Moin, P., 1998. A dynamic model for subgrid-scale variance and dissipation rate of a conserved scalar. *Phys. Fluids*, **10**:3041–3044.

Piomelli, U., 1999. Large-eddy simulation: achievements and challenges. *Progress in Aerospace Sciences*, **35**:335–362.

Pitsch, H. & Steiner, H., 2000. Large-eddy simulation of a turbulent piloted methane/air diffusion flame. Sandia flame D. *Phys. Fluids*, **12**:2541–2554.

Pitsch, H., 2006. Large-eddy simulation of turbulent combustion. *Annu. Rev. Fluid Mech.*, **38**(1): 453–482.

Poinsot, T. J. & Lele, S. K., 1992. Boundary-conditions for direct simulations of compressible viscous flows. *J. Comput. Phys.*, **101**(1):104–129.

Poinsot, T. & Veynante, D., 2005. *Theoretical and numerical combustion*. Edwards, Philadelphia, Pennsylvania.

Pope, S. B., 1985. PDF methods for turbulent reactive flows. *Prog. Energy Combust. Sci.*, **11**: 119–192.

Pope, S. B., 1990. Computations of turbulent combustion: Progress and challenges. *Proc. Combust. Inst.*, **23**:591–612.

Pope, S. B., 2004a. *Turbulent Flows*. Cambridge University Press, Cambridge, U.K.

Pope, S. B., 2004b. Ten questions concerning the large-eddy simulation of turbulent flows. *New Journal of Physics*, **6**:35.

Post, D. E. & Votta, L. G., January 2005. Computational science demands a new paradigm. *Physics Today*, **58**:35–41.

Powell, M. J. D., 1981. *Approximation Theory and Methods*. Cambridge University Press, Cambridge, U.K.

Pullin, D. I., 2000. A vortex-based model for the subgrid flux of a passive scalar. *Phys. Fluids*, **12**:2311–2316.

Pullin, D. I. & Lundgren, T. S., 2001. Axial motion and scalar transport in streched spiral vortices. *Phys. Fluids*, **13**:2553–2563.

Pullin, D. I. & Saffman, P. G., 1994. Reynolds stresses and one-dimensional spectra for a vortex model of homogenius anisotropic turbulence. *Phys. Fluids*, **6**:1787–1796.

Rai, M. M., 1986. A conservative treatment of zonal boundaries for Euler equation calculations. *J. Comp. Phys.*, **62**:472–503.

Raman, V., Pitsch, H., & Fox, R. O., 2006. Eulerian transported probability density function sub-filter model for large-eddy simulations of turbulent combustion. *Combustion Theory and Modelling*, **10**:439–458.

Ravier, S., Abid, M., Amielh, M., & Anselmet, F., 2006. Direct numerical simulations of variable-density plane jets. *J. Fluid Mech.*, **546**:153–191.

Reynolds, O., 1883. An experimental investigation of the circumstances which determine whether the motion of water shall be direct or sinuous, and of the law of resistance in parallel channels. *Philosophical Transactions of the Royal Society of London*, **174**:935–982.

Richardson, L. F., 1910. The approximate arithmetical solution by finite differences of physical problems involving differential equations with an application to the stresses in a masonry dam. *Trans. Royal Society London, Ser. A*, **210**:307–357.

Richardson, L. F., 1927. The deferred approach to the limit. *Trans. Royal Society London, Ser. A*, **226**:229–361.

Roache, P. J., 1998. *Verification and Validation in Computational Science and Engineering*. Hermosa Publishers, New Mexico.

Rossmann, T., Mungal, M. G., & Hanson, R. K., 2004. Mixing efficiency measurements using a modified cold chemistry technique. *Exp. Fluids*, **37**:566–576.

Roy, C. J., 2005. Review of code and solution verification procedures for computational simulation. *J. Comput. Phys.*, **205**(1):131–156.

Schlichting, H., 1979. *Boundary-layer theory*. McGraw-Hill.

Seiner, J. M., Dasha, S. M., & Kenzakowski, D. C., 2001. Historical survey on enhanced mixing in scramjet engines. *J. of Propul. Power*, **17**:1273–1286.

Shan, J. W. & Dimotakis, P. E., 2006. Reynolds-number effects and anisotropy in transverse-jet mixing. *J. Fluid Mech.*, **566**:47–96.

Slessor, M. D., Bond, C. L., & Dimotakis, P. E., 1998. Turbulent shear-layer mixing at high reynolds numbers: effects of inflow conditions. *J. Fluid Mech.*, **376**:115–138.

Slessor, M. D., Zhuang, M., & Dimotakis, P. E., 2000. Turbulent shear-layer mixing: growth-rate compressibility scaling. *J. Fluid Mech.*, **414**:35–45.

Smagorinsky, J., 1963. General circulation experiments with the primitive equations. i. the basic experiment. *Mon. Weather Rev.*, **91**:99–164.

Smith, S. H. & Mungal, M. G., 1998. Mixing, structure and scaling of the jet in crossflow. *J. Fluid Mech.*, **357**:83–122.

Spaid, F. W. & Zukoski, E. E., 1968. Secondary injection of gases into a supersonic flow. *AIAA J.*, **6**(2):205–212.

Steinberg, S. & Roache, P. J., 1985. Symbolic manipulation and computational fluid dynamics. *J. Comput. Phys.*, **57**(2):251–284.

Strand, B., 1994. Summation by parts for finite-difference approximations for d/dx. *J. Comput. Phys.*, **110**(1):47–67.

Stratford, B. S., 1959. The prediction of separation of the turbulent boundary layer. *J. Fluid Mech.*, **5**:1–16.

Tennekes, H. & Lumley, J. L., 1972. *A first course in turbulence.* MIT Press, Cambridge, Massachusetts.

Thompson, K. W., 1987. Time dependent boundary conditions for hyperbolic systems. *J. Comput. Phys.*, **68**:1–24.

VanLerberghe, W. M., Santiago, J. G., Dutton, J. C., & Lucht, R. P., 2000. Mixing of a sonic transverse jet injected into a supersonic flow. *AIAA J.*, **38**:470–479.

Venkataramani, K. S., Tutu, N. K., & Chevray, R., 1975. Probability distributions in a round heated jet. *Phys. Fluids*, **18**(11):1413–1420.

Veynante, D. & Knikker, R., 2006. Comparison between les results and experimental data in reacting flows. *Journal of Turbulence*, **7**(35).

Voelkl, T., Pullin, D. I., & Chan, D. C., 2000. A physical-space version of the stretched-vortex subgrid-stress model for large-eddy simulation. *Phys. Fluids*, **12**:1810–1825.

Vreman, B., Geurts, B., & Kuerten, H., 1996. Comparision of numerical schemes in large-eddy simulation of the temporal mixing layer. *Int. J. Numer. Methods Fluids*, **22**:297–311.

Wall, C., Boersma, B. J., & Moin, P., 2000. An evaluation of the assumed beta probability density function subgrid-scale model for large eddy simulation of nonpremixed, turbulent combustion with heat release. *Phys. Fluids*, **12**(10):2522–2529.

Warhaft, Z., 2000. Passive scalars in turbulent flows. *Annu. Rev. Fluid Mech.*, **32**(1):203–240.

Wesseling, P., 2001. *Principles of computational fluid dynamics.* Springer-Verlag Berlin Heidelberg.

Williams, F. A., 1975. Recent advances in theoretical descriptions of turbulent diffusion flames, In: *Turbulent mixing in nonreactive and reactive flows*, S. N. B. Murthy (Ed.), pages 189–208, Plenum Press, New York.

Williams, F. A., 1985. *Combustion Theory.* Addison Wiley.

Yu, K. H., Wilson, K. J., & Schadow, K. C., 2001. Effect of flame-holding cavities on supersonic-combustion performance. *J. of Propul. Power*, **17**(6):1287–1295.

Yu, K. H., Wilson, K. J., Smith, R. A., & Schadow, K. C., 1998. Experimental investigationon dual-purposecavity insupersonicreacting flows. *AIAA Paper* 98-0723.

Zang, T. A., 1991. On the rotation and skew-symmetric forms for incompressible flow simulations. *Appl. Numer. Math.*, **7**(1):27–40. ISSN 0168-9274.

Zhuang, M., Dimotakis, P. E., & Kubota, T., 1990a. The effect of walls on a spatially growing supersonic shear layer. *Phys. Fluids A*, **2**(4):599–604.

Zhuang, M., Kubota, T., & Dimotakis, P. E., 1990b. Instabillity of inviscid, compressible free shear layers. *AIAA Journal*, **28**(10):1728–1733.

Zukoski, E. E. & Spaid, F. W., 1964. Secondary injection of gases into a supersonic flow. *AIAA J.*, **2**(10):1689–1696.